

**AXIAL FLUX PERMANENT MAGNET MACHINE WITH NOVEL FLAT
WINDING MADE OF CONDUCTOR SHEET**

A THESIS SUBMITTED TO
THE GRADUATE SCHOOL OF NATURAL AND APPLIED SCIENCES
OF
MIDDLE EAST TECHNICAL UNIVERSITY

BY

GÖKHAN ÇAKAL

IN PARTIAL FULFILLMENT OF THE REQUIREMENTS
FOR
THE DEGREE OF MASTER OF SCIENCE
IN
ELECTRICAL AND ELECTRONICS ENGINEERING

SEPTEMBER 2020

Approval of the thesis:

**AXIAL FLUX PERMANENT MAGNET MACHINE WITH NOVEL FLAT
WINDING MADE OF CONDUCTOR SHEET**

submitted by **GÖKHAN ÇAKAL** in partial fulfillment of the requirements for the degree of **Master of Science in Electrical and Electronics Engineering Department, Middle East Technical University** by,

Prof. Dr. Halil Kalıpçılar _____
Dean, Graduate School of **Natural and Applied Sciences**

Prof. Dr. İlkay Ulusoy _____
Head of Department, **Electrical and Electronics Engineering**

Assist. Prof. Dr. Ozan Keysan _____
Supervisor, **Electrical and Electronics Engineering, METU**

Examining Committee Members:

Assist. Prof. Dr. Emine Bostancı _____
Electrical and Electronics Engineering, METU

Assist. Prof. Dr. Ozan Keysan _____
Electrical and Electronics Engineering, METU

Prof. Dr. Lale Tükenmez Ergene _____
Electrical Engineering, Istanbul Technical University

Assoc. Prof. Dr. Metin Aydin _____
Mechatronics Engineering, Kocaeli University

Assist. Prof. Dr. Taner Göktaş _____
Electrical and Electronics Engineering, Inonu University

Date: 18.09.2020

I hereby declare that all information in this document has been obtained and presented in accordance with academic rules and ethical conduct. I also declare that, as required by these rules and conduct, I have fully cited and referenced all material and results that are not original to this work.

Name, Surname: Gökhan Çakal

Signature : 

ABSTRACT

AXIAL FLUX PERMANENT MAGNET MACHINE WITH NOVEL FLAT WINDING MADE OF CONDUCTOR SHEET

Çakal, Gökhan

M.S., Department of Electrical and Electronics Engineering

Supervisor: Assist. Prof. Dr. Ozan Keysan

September 2020, 121 pages

This thesis proposes a novel winding topology, called flat winding, as an alternative to the conventional windings with stranded round wires for electric machines. It is made of a thin conductor sheet by industrial automation tools such as stamping press, laser, or water jet. Since these tools are widely used in the production of electric machines, the flat winding topology enjoys the advantage of the ease of manufacturing without significant modification on the production line. Superior current ratings, shortened end windings, and high fill factors are other advantages of flat winding. In order to evaluate its performance, it is implemented on the axial flux permanent magnet machine. Analytical modeling of the machine, including field modeling, voltage, torque derivations, and losses modeling, eliminated the finite element dependency. The promised advantages of flat winding are investigated on 1.4 kW, 26 Nm, and 48 V prototype machine, and the accuracy of the analytical models are validated through experimental verification. The feasibility of copper and aluminum flat windings is investigated on the prototype and compared in cost, manufacturing, and efficiency. The performance of flat winding topology in MW-scale machines are evaluated on

1 MW, 480 kNm, and 680 V direct-drive generator for wind turbine application. It is seen that flat winding has elevated the machine performance by achieving 46 Nm/kg torque density. In conclusion, the analysis in the thesis shows that novel flat winding topology is a promising alternative to the conventional windings for electric machines.

Keywords: Electric Machine Winding, Axial Flux Permanent Magnet Machine, Analytical Modeling, Wind Turbine Generator, Optimization

ÖZ

İLETKEN LEVHADAN ÜRETİLEN ÖZGÜN YASSI SARGILI EKSENEL AKILI SABİT MIKNATISLI MAKİNA

Çakal, Gökhan

Yüksek Lisans, Elektrik ve Elektronik Mühendisliği Bölümü

Tez Yöneticisi: Dr. Öğr. Üyesi. Ozan Keysan

Eylül 2020 , 121 sayfa

Bu tez, elektrikli makineler için, ince, yuvarlak tellere sahip geleneksel sargılara alternatif olarak, yassı sargı adı verilen yeni bir sargı topolojisi önermektedir. Önerilen sargı türü, damgalama presi, lazer veya su jeti gibi endüstriyel otomasyon araçlarıyla ince bir iletken levhadan üretilmektedir. Bu araçlar elektrikli makineleri üretiminde yaygın olarak kullanıldığından, yassı sargı topolojisi, üretim hattında önemli değişikliklere neden olmaksızın, üretim kolaylığı avantajına sahiptir. Yüksek akım değerleri, kısaltılmış sargı sonları uzunluğu ve yüksek doldurma faktörü, yassı sarginin diğer avantajlarıdır. Önerilen sargı türünün performansını değerlendirmek için, yassı sargı topolojisi, eksenel akılı, sabit mıknatıslı makinede uygulanmıştır. Manyetik alan analizi, gerilim, döndürme momenti formülünün çıkarılması ve kayıpların modellenmesi içeren makinenin analitik modeli, sonlu eleman analizi bağımlılığını ortadan kaldırmıştır. Yassı sarginin vaat edilen avantajları, 1.4 kW, 26 Nm ve 48 V değerlerine sahip, üretimi gerçekleştirilen prototip makine üzerinde araştırılmış ve analitik modellerin hassasiyeti deneysel doğrulama yoluyla ölçülmüştür. Bakır ve alüminyum yassı sargıların fizibilitesi, maliyet, üretim ve verimlilik açısından prototip üz-

rinde araştırılmıştır. MW ölçekli makinelerde yassı sargı topolojisinin performansı, 1 MW, 480 kNm ve 680 V değerlerine sahip, rüzgâr türbini uygulaması için, doğrudan tahrikli generatör üzerinden değerlendirilmiştir. Yassı sargıya sahip generatörün, 46 Nm/kg döndürme monenti yoğunluğuna ulaşarak, makine performansını yükselttiği görülmüştür. Sonuç olarak, tezde sunulan analiz, özgün yassı sargı topolojisinin, elektrik makineleri geleneksel sargılarıyla karşılaştırıldığında, gelecek vaat eden bir alternatif olduğunu göstermektedir.

Anahtar Kelimeler: Elektrik Makinesi Sargısı, Eksenel Akılı Sabit Mıknatıslı Makine, Analitik Modelleme, Rüzgâr Türbini Generatörü, Optimizasyon

To my family...

ACKNOWLEDGMENTS

Foremost, I would like to express my sincere gratitude to my supervisor Dr. Ozan Keysan for the continuous support of my MSc study and research for his patience, motivation, enthusiasm, and immense knowledge. His guidance helped me in all the time of research and writing of this thesis. I could not have imagined having a better supervisor and mentor for my MSc study.

Besides my supervisor, I would like to thank the rest of my thesis committee: Prof. Lale Tükenmez Ergene, Dr. Metin Aydin, and Dr. Taner Göktaş for their encouragement, insightful comments, and hard questions. I want to give special thanks to Dr. Emine Bostancı, who helped me solve challenging finite element problems with her patience.

I am thankful to TUBITAK, The Scientific and Technological Research Council of Turkey, for granting me their MSc studies scholarship.

I wish to show my gratitude to my colleagues in PowerLab Research Group: Furkan Karakaya, Serhat Emir Ogan, Yusuf Basri Yılmaz, and others in the office for the stimulating discussions and for all the fun we have had in the last four years. Also, I would like to thank Furkan Tokgöz and Hande Bayazıt for helping me in the prototyping stage.

I would like to express my heartfelt thanks to Gizem Demirkol. Her love and encouragement when the times got rough are much appreciated and duly noted. Without her support, it would not be easy to complete this work.

Finally, my deep and sincere gratitude goes to my parents, Kemal and Ayten, for their love, caring, and sacrifices for my education for a bright future.

TABLE OF CONTENTS

| | |
|---|------|
| ABSTRACT | v |
| ÖZ | vii |
| ACKNOWLEDGMENTS | x |
| TABLE OF CONTENTS | xi |
| LIST OF TABLES | xiv |
| LIST OF FIGURES | xvi |
| LIST OF ABBREVIATIONS | xxi |
| LIST OF VARIABLES | xxii |
| CHAPTERS | |
| 1 INTRODUCTION | 1 |
| 1.1 Proposed Solution | 2 |
| 1.2 Existing Topologies and Differences | 3 |
| 1.3 The Outline of the Thesis | 5 |
| 2 PROPOSED MACHINE TOPOLOGY WITH NOVEL FLAT WINDING | 7 |
| 2.1 Existing electric machine topologies | 7 |
| 2.1.1 Axial Flux vs. Radial Flux Machines | 7 |
| 2.1.2 Air-cored vs. Iron-cored Machines | 9 |

| | | |
|-------|--|----|
| 2.2 | Overview of the Proposed Machine | 10 |
| 2.3 | Flat Winding Stator | 12 |
| 2.4 | Rotor | 16 |
| 2.5 | Design Challenges | 19 |
| 2.6 | Summary | 20 |
| 3 | ANALYTICAL MODELING OF THE MACHINE | 23 |
| 3.1 | Magnetic Field Modeling | 23 |
| 3.2 | Induced Voltage and Torque Characteristics | 34 |
| 3.3 | Loss Modeling | 35 |
| 3.4 | Deflection Analysis | 39 |
| 3.5 | Summary | 44 |
| 4 | EXPERIMENTAL VERIFICATION OF THE TOPOLOGY WITH 1.4 KW PROTOTYPE | 47 |
| 4.1 | Optimization Using Genetic Algorithm | 47 |
| 4.2 | Mechanical Design | 54 |
| 4.3 | Manufacturing of the Prototype Machine | 56 |
| 4.4 | Experimental Results | 61 |
| 4.5 | Copper vs. Aluminum Flat Winding | 65 |
| 4.6 | Demagnetization Analysis | 72 |
| 4.6.1 | Demagnetization Current by Finite Element Analysis | 74 |
| 4.6.2 | Maximum Current Calculation | 76 |
| 4.7 | Summary | 77 |
| 5 | 1 MW DIRECT-DRIVE WIND TURBINE GENERATOR | 79 |

| | | |
|-------|---|-----|
| 5.1 | Mechanical Structure | 81 |
| 5.1.1 | C-shaped Core Design | 81 |
| 5.1.2 | Multi-staged Design | 82 |
| 5.2 | Genetic Algorithm Optimization | 82 |
| 5.2.1 | Diameter Variation | 84 |
| 5.2.2 | Flat Wire Thickness Variation | 85 |
| 5.2.3 | The Optimum Design | 88 |
| 5.3 | Thermal analysis of the optimum design | 92 |
| 5.4 | Comparison of the Optimum Design with Existing Technologies . . . | 94 |
| 5.5 | Demagnetization Analysis | 95 |
| 5.6 | Summary | 97 |
| 6 | CONCLUSIONS AND FUTURE WORKS | 99 |
| 6.1 | Future Work | 101 |
| | REFERENCES | 103 |
| A | FOURIER SERIES REPRESENTATION OF MAGNETIZATION | 115 |
| B | CONSTANTS USED IN CIRCULAR PLATE THEORY FOR DEFLECTION ANALYSIS | 119 |
| C | SUPPLEMENTARY DOCUMENTS | 121 |

LIST OF TABLES

TABLES

| | |
|---|----|
| Table 3.1 Specifications of the selected machine for validation of field modeling | 32 |
| Table 3.2 Specifications of the selected machine for loss modeling validation | 38 |
| Table 3.3 Comparison of the losses obtained by analytical model and finite element analysis, for the selected machine | 38 |
| Table 3.4 Parameters of the selected machine for the deflection analysis | 42 |
| Table 4.1 Optimization constraints | 48 |
| Table 4.2 Optimization parameters | 49 |
| Table 4.3 The optimum design parameters of the 1.4 kW prototype | 50 |
| Table 4.4 Loss and efficiency comparison of analytical and experimental results | 65 |
| Table 4.5 Evaluation of the designs with copper and aluminum stators at rated speed (26 Nm, 525 rpm) and high speed (14 Nm, 1000 rpm) operations | 71 |
| Table 5.1 Fixed design parameters | 83 |
| Table 5.2 Optimization parameters | 83 |
| Table 5.3 Optimized 1 MW, 20 rpm generator design parameters | 89 |
| Table 5.4 Specific costs of the materials [86] | 90 |
| Table 5.5 Comparison of the optimum design with other direct-drive permanent magnet generators studied in the literature | 94 |

Table 6.1 Comparison of the winding topologies 100

LIST OF FIGURES

FIGURES

| | | |
|-------------|--|----|
| Figure 1.1 | Conventional and proposed winding for electric machines | 2 |
| Figure 1.2 | Alternative winding topologies proposed in the literature | 4 |
| Figure 2.1 | Electric machine categorization according to flux passing direction [22] | 8 |
| Figure 2.2 | Various configurations of axial flux machines [23] | 9 |
| Figure 2.3 | Basis representation of the selected axial flux permanent magnet machine | 11 |
| Figure 2.4 | Manufacturing of flat wire from thin copper sheet using laser cutter | 12 |
| Figure 2.5 | Manufacturing steps of the flat wire | 13 |
| Figure 2.6 | Flat wires forming the air-cored stator | 14 |
| Figure 2.7 | Manufactured copper flat wired stator | 14 |
| Figure 2.8 | The evaluation of the different pole shapes | 16 |
| Figure 2.9 | Single loop of flat winding with rotor structure employing diagonally placed permanent magnets | 17 |
| Figure 2.10 | Induced voltage on a single loop of flat winding | 17 |
| Figure 2.11 | Single turn of flat winding composed of as many flat wires as the number of pole pairs | 18 |
| Figure 2.12 | Bending angles of the flat wire | 19 |

| | | |
|-------------|---|----|
| Figure 2.13 | Exploded view of the proposed AFPM with novel flat winding | 19 |
| Figure 3.1 | Approximation of the permanent magnets | 24 |
| Figure 3.2 | 2D representation of the simplified model | 25 |
| Figure 3.3 | Two regions representing the magnetic field: air and magnet regions [48] | 25 |
| Figure 3.4 | Magnetization characteristics of permanent magnets [48] | 26 |
| Figure 3.5 | Superposition principle used for the field analysis of double-sided rotor structure | 32 |
| Figure 3.6 | Flux density distribution of the analyzed machine obtained using FEA | 33 |
| Figure 3.7 | Comparison of no-load air gap magnetic flux density at mean radius | 33 |
| Figure 3.8 | Voltage generation of a portion of a single loop of flat winding | 34 |
| Figure 3.9 | Losses of the proposed machine | 36 |
| Figure 3.10 | Eddy current loss on a conductor due to external PM field | 37 |
| Figure 3.11 | Circular plate model of rotor disc for analytical deflection analysis [50] | 40 |
| Figure 3.12 | Approximation of Maxwell stress on rotor discs for deflection analysis | 41 |
| Figure 3.13 | Deflection analysis of rotor disc by finite element method | 43 |
| Figure 3.14 | Deflection analysis of the detailed rotor disc | 44 |
| Figure 4.1 | Air gap flux density distribution of the optimum design obtained using 3D FEA | 52 |
| Figure 4.2 | Air gap flux density of the optimum design | 52 |

| | |
|--|----|
| Figure 4.3 Output torque of the optimum design with sinusoidal excitation obtained by 3D FEA | 53 |
| Figure 4.4 3D mesh structure used in finite element analysis | 53 |
| Figure 4.5 Mechanical drawing of the optimum design on SolidWorks | 54 |
| Figure 4.6 Mechanical assembly of the optimum design | 55 |
| Figure 4.7 Manufacturing of flat wires with laser cutter | 56 |
| Figure 4.8 Manufactured copper flat wire | 57 |
| Figure 4.9 Manufacturing of flat winding stator | 57 |
| Figure 4.10 A hot spot at the improper end winding connection due to weak soldering | 58 |
| Figure 4.11 Epoxy molding of flat winding | 59 |
| Figure 4.12 Phasor diagram of the three phase stator | 59 |
| Figure 4.13 Manufactured rotor disc employing diagonally placed perma- nent magnets | 60 |
| Figure 4.14 Manufactured prototype machine | 60 |
| Figure 4.15 Experimental setup | 61 |
| Figure 4.16 Open circuit characteristics of the prototype machine | 62 |
| Figure 4.17 Phase voltage and line current measurements of the prototype machine at full-load and half-load conditions | 63 |
| Figure 4.18 Thermal characteristics of the stator windings | 63 |
| Figure 4.19 The eddy current loss on the windings due to external PM field and friction&windage losses measurement at various rotational speeds at no-load | 64 |

| | |
|---|----|
| Figure 4.20 Manufactured copper (left) and aluminum flat winding stators for the prototype machine | 66 |
| Figure 4.21 Experimental data of eddy current losses on the windings due to external PM field of copper and aluminum stators | 67 |
| Figure 4.22 Temperature increase of copper and aluminum stators at various loading conditions at rated speed | 68 |
| Figure 4.23 Total losses of the machines with different flat winding materials | 69 |
| Figure 4.24 Efficiency map of the machines with different stator materials . . | 70 |
| Figure 4.25 Favorable material in terms of losses and efficiency | 70 |
| Figure 4.26 Typical BH characteristics of a permanent magnet | 73 |
| Figure 4.27 Direct and quadrature axes of the proposed machine | 74 |
| Figure 4.28 Peak current profile applied in demagnetization analysis | 75 |
| Figure 4.29 Demagnetization characteristic of the permanent magnet at different peak short circuit phase currents at 80 °C | 76 |
| | |
| Figure 5.1 Exploded view of AFPM generator with novel flat winding for wind turbine applications | 80 |
| Figure 5.2 Structural models | 81 |
| Figure 5.3 The variation of generator parameters against diameter | 85 |
| Figure 5.4 Two designs with different flat wire thicknesses | 86 |
| Figure 5.5 The variation of generator parameters against flat wire thickness | 87 |
| Figure 5.6 Convergence plot of the genetic algorithm | 88 |
| Figure 5.7 The optimum 1 MW and 20 rpm design | 90 |
| Figure 5.8 Sample manufacturing cut-out of 92 flat wires from copper sheet with dimensions of 1 m and 2 m using a planar cutting tool such as laser | 91 |

| | | |
|-------------|---|-----|
| Figure 5.9 | Thermal analysis of the optimum design at rated operation | 93 |
| Figure 5.10 | Thermal analysis of the partially coated stator design | 93 |
| Figure 5.11 | Demagnetization characteristic of the permanent magnet at different peak short circuit phase currents | 96 |
| Figure A.1 | Magnetization characteristics of permanent magnets | 116 |
| Figure C.1 | Scan this QR code to reach the repository | 121 |

LIST OF ABBREVIATIONS

ABBREVIATIONS

| | |
|-------|--------------------------------------|
| 2D | Two dimensional |
| 3D | Three dimensional |
| AFPM | Axial Flux Permanent Magnet Machine |
| CNC | Computer Numerical Control |
| EMF | Electromotive Force |
| FEA | Finite Element Analysis |
| GA | Genetic Algorithm |
| IPM | Interior Permanent Magnet |
| MIG | Metal Inert Gas |
| NdFeB | Neodymium Iron Boron |
| PCB | Printed Circuit Board |
| PM | Permanent Magnet |
| RFPM | Radial Flux Permanent Magnet Machine |
| THD | Total Harmonic Distortion |
| TIG | Tungsten Inert Gas |

LIST OF VARIABLES

VARIABLES

| | |
|--------------|---|
| a | Number of series-connected flat wires per phase per stage |
| a_r | Rotor disc outer radius |
| b | Number of series-connected stages |
| \vec{B} | Magnetic flux density vector |
| B_r | Remanence flux density of permanent magnets |
| b_r | Shaft radius |
| C | Unknown coefficient |
| D | Plate constant |
| E | Young's Modulus |
| f_e | Electrical frequency |
| \vec{H} | Magnetic field strength vector |
| H_c | Coercivity of permanent magnets |
| h_m | Permanent magnet thickness |
| \hat{I} | Peak stator current |
| I_d | D-axis current |
| I_{demag} | Peak phase current causing demagnetization |
| I_{normal} | Peak phase current in normal operation |
| I_{ph} | Phase rms current |
| I_q | Q-axis current |
| k_{mag} | Maxwell stress modifier |
| k_1 | Harmonics factor for eddy current loss calculation |

| | |
|-----------|--|
| k_w | Winding factor |
| l | Conductor length of flat wire |
| L | Distance between two rotor discs |
| L_{ph} | Phase inductance |
| M_{rb} | Unit radial bending moment at the shaft |
| m_{yCS} | Fourier coefficients of cosine terms |
| M_y | Magnetization of permanent magnets |
| n | Number representing space harmonic |
| p | Number of poles |
| P_{sp} | Volumetric specific eddy current loss on the windings due to external PM field |
| P_c | DC winding losses |
| pp | Number of pole pairs |
| q | Maxwell stress |
| Q_b | Unit shear force at the shaft |
| R_{ph} | Phase resistance |
| r_m | Mean radius of flat winding |
| r_o | Inner radius of the area occupied by magnets |
| s | Total number of stages |
| T | Electrical period |
| t | Flat wire thickness |
| T | Output torque |
| t_c | Rotor core thickness |
| V_d | Direct axis voltage |
| V_{ph} | Induced phase rms voltage |
| V_q | Quadrature axis voltage |
| w | Flat wire width |

| | |
|----------------|----------------------------------|
| y | Displacement at the outer radius |
| α_p | Magnet to pole pitch ratio |
| β | Bending angle of flat wire |
| λ_{PM} | Permanent magnet flux linkage |
| μ_0 | Permeability of free space |
| μ_r | Relative permeability |
| ν | Poisson ratio |
| ω | Mechanical rotational speed |
| ω_e | Electrical rotational speed |
| ρ | Resistivity |
| τ_p | Pole pitch |
| θ | Load angle |
| φ | Magnetic scalar potential |

CHAPTER 1

INTRODUCTION

It is a well-known fact that the winding of an electric machine significantly affects machine performance by determining critical parameters such as current density, fill factor or winding losses. Most of the electric machines currently employ conventional windings with stranded round wires shown in Fig. 1.1a. However, they may not meet the increasing performance demand by advances in technology due to their limitations. For example, in order to improve the torque density of the machine, the current density of windings can be increased. However, the thermal performance of the conventional windings may limit the current density, and an advanced cooling system may be required for superior ratings. Additionally, for some applications, such as traction applications, high torque or current ratings are desired. In order to increase the current rating of the conventional round wires, the coils are generally connected in parallel, which may cause some problems, such as circulating currents. The fill factor of the winding is among other parameters that define the machine performance, and it is desired to be increased. However, the fill factor of the conventional round wires is limited around 35–45 % due to the round shape [1]. Additionally, stranded round wires require customized machines for the winding process. They are typically wound around a tooth with the help of these winding machines. Since they are customized for this task only, they increase the manufacturing cost and labor required in the production.

To sum up, the conventional windings with stranded round wires may limit the machine performance in some cases, and novel winding solutions are desired to overcome the challenges mentioned above.



(a) Conventional winding with stranded round wires [2]



(b) Proposed flat wire made of thin conductor sheet



(c) Proposed flat winding

Figure 1.1: Conventional and proposed winding for electric machines

1.1 Proposed Solution

This thesis presents a novel winding topology made of a thin conductor sheet as an alternative to the conventional windings with stranded round wires. The proposed winding topology is called ‘flat winding,’ and it is composed of many flat wires, as shown in Fig. 1.1b. Small pieces are cut from the conductor sheet using a stamping press, laser, or water jet, and by bending and welding operations, the flat winding can be formed easily. In Fig. 1.1c, a manufactured flat winding is shown. The details of the manufacturing stages will be presented in Section 2.3.

The proposed flat winding topology can provide significant advantages, and it is able to overcome the challenges mentioned in the previous section. It is seen that the flat winding is able to operate with superior current densities. Also, due to its large cross-sectional area, the flat winding can carry high currents without a need for par-

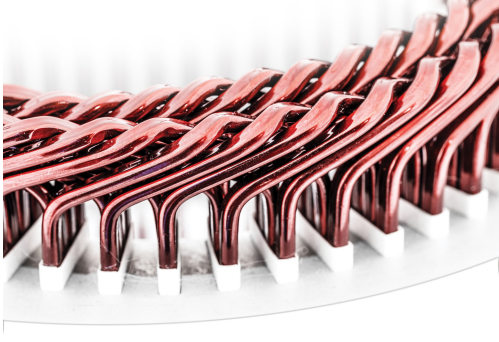
allel connection. Its rectangular-shaped cross-sectional area also enables to achieve superior fill factors. The detailed advantages of the flat winding will be presented in Section 2.3. To sum up, it is seen that the flat winding is a promising alternative for conventional windings.

1.2 Existing Topologies and Differences

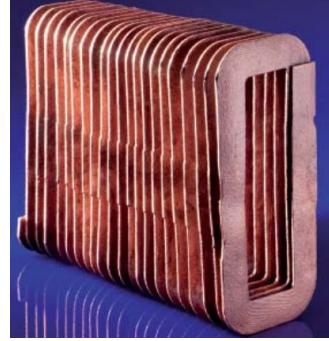
Today, most of the electric machines employ conventional windings with stranded round wires. In Fig. 1.1, proposed flat winding topology and conventional winding with stranded round wires are shown. The first difference between these two winding topologies appears in manufacturing. Proposed flat winding promises ease of manufacturing because the tools used to manufacture flat wire, such as stamping press, are widely used in the manufacturing of electric machines. Therefore, without significant modification on the production line, the flat winding can be manufactured easily.

Generally, conventional windings can operate with current density of 5 A/mm^2 to 6 A/mm^2 under air cooling [3]. As will be explored in Section 4.4, it is seen that the proposed flat winding is able to operate with current density of 7 A/mm^2 under natural cooling. This value can be increased further under forced cooling, which presents a clear advantage of flat winding over conventional winding. Additionally, high fill factor and shortened end winding length are among other advantages that make flat winding more favorable over conventional stranded windings.

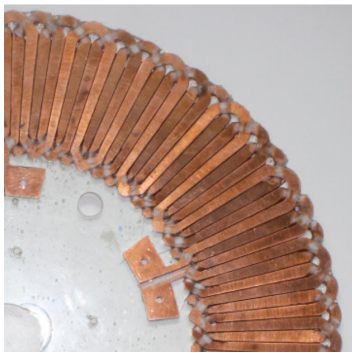
As an alternative to the conventional stranded wires, there are also other winding topologies studied in the literature, as shown in Fig. 1.2. For example, a hairpin or bar-wound windings shown in Fig. 1.2a are widely studied in recent years [4, 5, 6]. In fact, this type of winding is commercialized in traction applications, such as in Toyota Prius [7], or Chevrolet Volt [8]. The main differences between the flat winding and hairpin winding rely on manufacturing and structure. While hairpin winding is manufactured from readily available and enameled bar-wound conductors, the flat winding is manufactured from a thin conductor sheet by cutting and bending operations. Additionally, since it is made of a thin conductor sheet, the flat wire has a smaller thickness to width ratio, compared to hairpin winding. To illustrate, the



(a) Hairpin or bar-wound winding [10]



(b) Winding by cast production [11]



(c) Solid winding by water jet and CNC [12]



(d) PCB winding

Figure 1.2: Alternative winding topologies proposed in the literature

hairpin winding used in 2017 Prius motor has dimensions of $2.24 \times 3.81 \text{ mm}^2$ [9]; however, the flat wire used in the prototype machine in Chapter 4 has dimensions of $1 \times 5 \text{ mm}^2$. Related to this, hairpin winding suffers from elevated AC losses due to its large cross-sectional area and requires improved cooling. However, since the flat wire in this study is made of a thin conductor sheet and stacked through the thickness in the circumferential direction, AC losses are significantly reduced, whose experimental verification will be given in Chapter 4.

Additionally, in [13, 14], the authors presented casting production of electric machine windings, as shown in Fig. 1.2b; however, similar to hairpin windings, they also suffer from elevated AC losses, which is significantly reduced in the proposed flat winding. The author in [12] presents a winding design shown in Fig. 1.2c, which is manufactured from 4 mm thick copper using a water jet. Unlike flat winding, the

entire winding of a phase is manufactured as one piece, and overlapping regions are milled using CNC. This leads to a non-uniform cross-sectional area through the coil. Additionally, the magnets in the study have conventional rectangular placement while they are placed diagonally in this study due to the design of flat winding, as will be explained later. Again, it is observed that the coil design in [12] suffers from AC losses with a measured efficiency of 25%. Lastly, there are examples of winding design, in which the windings of the machine are printed on a PCB [15, 16, 17], and one example of it is shown in Fig 1.2d. Compared to the flat winding stator, the PCB winding stator is not suitable for kW-range power applications due to the limited number of copper layers and copper thickness on PCB. Also, it is not cost-effective compared to the flat winding topology.

1.3 The Outline of the Thesis

The outline of the thesis is as follows:

In Chapter 2, a literature survey is presented, where the existing electric machine topologies are summarized in terms of flux passing direction and stator core material. Then, axial flux permanent magnet machine (AFPM) topology is selected for the implementation of flat winding, and the details of the selected topology are presented. First, the advantages and possible applications of AFPM are outlined. Then, the stator part of the machine is presented, starting from the manufacturing stages of the flat winding. Also, the promised advantages of the flat winding are highlighted here. Lastly, the design challenges of AFPM are presented.

In Chapter 3, analytical modeling of AFPM is presented. First, air gap flux density is modeled using magnetic scalar potential, and the results are compared with finite element simulations. Then, the induced voltage and torque of AFPM are derived. Also, analytical modeling of the machine losses, including DC winding losses and eddy current losses on the windings due to external PM field, are presented. The accuracy of the models is measured on a dummy machine by comparing the results of the analytical models and finite element solutions. Lastly, an analytical model that calculates the deflection of the rotor cores due to Maxwell stress is presented.

In Chapter 4, in order to measure the accuracy of the analytical models and highlight the promised advantages of the flat winding on a real machine, experimental verification is presented with 1.4 kW prototype. The manufacturing details of the machine are given, and the experimental setup is introduced. Then, experimental test results are presented, including open circuit characteristics, thermal characteristics, losses, and efficiency measurements. Lastly, the feasibility of aluminum flat winding is investigated.

In Chapter 5, the performance of the proposed flat winding is evaluated on 1 MW direct-drive wind turbine generator. First, the mechanical structure of the generator is introduced. Then, the generator is optimized by genetic algorithm with the given constraints to achieve minimum mass. The optimized generator is compared with the proposed generators in the literature in terms of mass and torque density. Additionally, the thermal analysis of the generator is investigated using finite element analysis, and improved thermal solutions are proposed for the flat winding stator. Lastly, a demagnetization study is presented for the 1 MW-generator.

CHAPTER 2

PROPOSED MACHINE TOPOLOGY WITH NOVEL FLAT WINDING

This chapter presents existing electric machine topologies and selects one to investigate the performance of flat winding on an application. The advantages and potential applications of the selected topology are presented. Also, the design challenges will be highlighted.

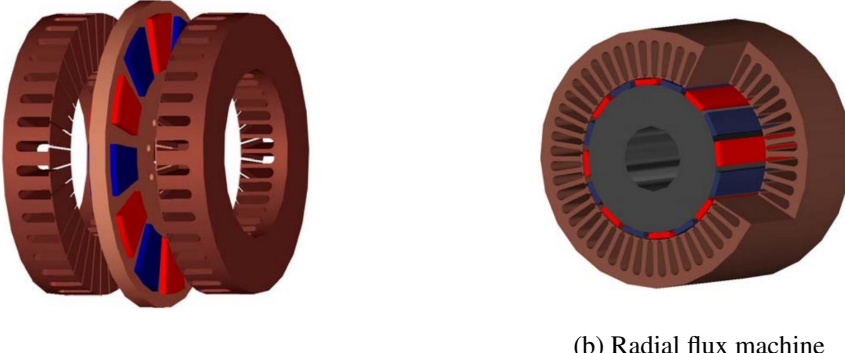
2.1 Existing electric machine topologies

In order to gain a general insight into electric machine topologies, this section categorizes the electric machines for two properties. Firstly, they are categorized in terms of flux passing direction as axial flux and radial flux machines. Then, they are categorized according to the stator core material as air-cored and iron-cored machines.

2.1.1 Axial Flux vs. Radial Flux Machines

Electric machines can be categorized into two groups according to the flux passing direction: axial flux and radial flux machines, as shown in Fig. 2.1. They are also referred to as an axial air gap and radial air gap machines [18, 19]. There are also transverse flux machines; however, they are not included in this categorization because they are not commonly used due to low power factor [20]. The key differences between radial and axial flux machines can be stated as follows:

- Axial flux machines have short axial length and large diameter, whereas radial flux machines have long axial length and short diameter. Due to their large diameters, axial flux machines have higher torque density.



(a) Axial flux machine

(b) Radial flux machine

Figure 2.1: Electric machine categorization according to flux passing direction [22]

- There is no net attraction force on rotor and stator for radial flux machines due to rotational symmetry. However, for the axial flux machines, depending on the topology, there can be non-zero attraction force in the axial direction on the rotor or stator due to Maxwell stress. This can cause the deflection into the air gap and makes the mechanical design challenging for axial flux machines. This attraction also results in stress on the bearings in the axial direction, causing mechanical faults over time [21].
- Axial flux machines have the advantage of stackability in the axial direction. In this way, the modularity of the machine can be achieved, and the fault tolerance of the machine can be increased.

Since the proposed flat winding topology in this thesis is implemented as an axial flux machine, further investigation of axial flux machines is needed. In Fig. 2.2, various configurations of the axial flux machines are shown. Firstly, it is observed that the configurations have a different number of air gaps, which effectively determines the mechanical complexity. Secondly, note that the attraction force in the axial direction on the intermediate rotor and stator parts is eliminated. For example, for the design in Fig. 2.2c, assuming that the stator is iron-cored, the stator is attracted in the axial direction by two rotor discs. Thus, the net force in the axial direction on the stator is zero, which eliminates the deflection of the stator for this case. However, for the iron-cored stator or rotor of all configurations, there is a non-zero attraction force in the axial direction due to Maxwell stress.

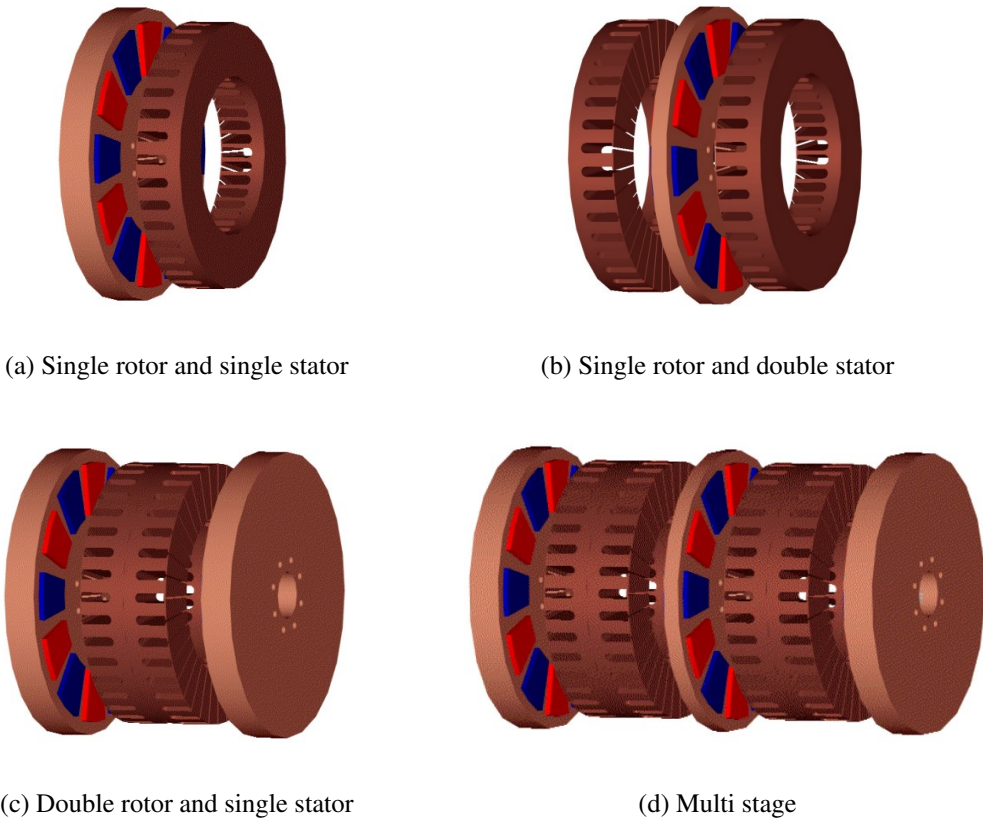


Figure 2.2: Various configurations of axial flux machines [23]

2.1.2 Air-cored vs. Iron-cored Machines

According to the stator core material, electric machines can be categorized into two groups: air-cored (ironless or coreless) and iron-cored machines. In iron-cored machines, the armature windings are wound around a magnetic material with high permeability, such as magnetic steel, to decrease the system's magnetic reluctance. However, for air-cored machines, there is no magnetic material in the stator structure. The key differences between air-cored and iron-cored machines can be explained on the studied topology in the thesis, the one in Fig. 2.2c, as follows:

- Since there is no magnetic material in its stator, the air-cored machine has a larger magnetic air gap and magnetic reluctance than an iron-cored machine with the same dimensions. This leads to lower magnetic loading for the air-cored machine.

- Due to its high reluctance, the air-cored machine has a lower inductance than the iron-cored machine. Lower inductance limits the field weakening performance of the air-cored machine and decreases the power factor [24]. Additionally, lower inductance causes large short circuit currents on the windings due to low impedance.
- The iron-cored design suffers from the core losses on the stator. However, since there is no magnetic material on the air-cored design's stator, no core losses are observed.
- Due to the lack of magnetic material in the stator, there is no attraction force between rotor and stator parts of the air-cored configuration in Fig. 2.2c. This makes the mechanical design less challenging for the air-cored machine.
- There are no problems related to cogging torque for air-cored design. However, for the slotted iron-cored design, cogging torque may be observed.
- For the air-cored machine, the magnetic loading is low, and the rotor cores' deflection is limited. Thus, less structural elements that keep the air gap clearance within the tolerances are needed, resulting in lower mass.

2.2 Overview of the Proposed Machine

Axial flux permanent magnet machine (AFPM) topology in Fig. 2.2c is selected for this study. It has a double rotor and single rotor structure, where the stator is sandwiched between two rotor discs. The stator is air-cored, and it employs novel flat winding topology that will be presented in the next section. The double-sided rotor includes strong permanent magnets placed on the rotor yokes. The design has two air gaps due to the double-sided structure. The basic representation of the proposed AFPM can be seen in Fig. 2.3.

The proposed machine has the following advantages:

- The stator of the machine is air-cored; therefore, there is no cogging torque.

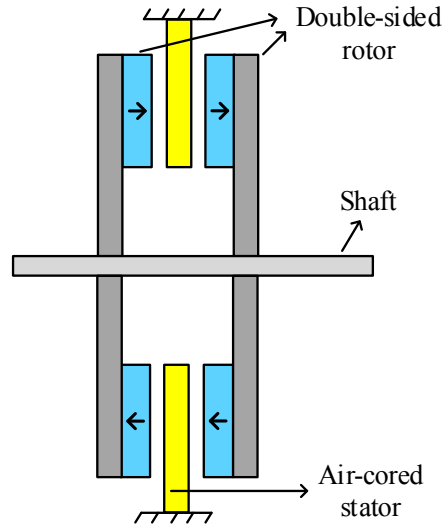


Figure 2.3: Basis representation of the selected axial flux permanent magnet machine

- There is no attraction force between rotor and stator due to the air-cored design. This reduces the structural mass required to maintain air gap clearance and reduces the manufacturing and assembly cost.
- Compared to its radial flux counterpart, AFPM has higher torque density [25, 26, 27]. A longer lever arm can explain this due to the larger mean radius of AFPM topology compared to conventional inner rotor radial flux design.
- The design is stackable in the axial direction. Multi-staged designs can reduce the structural mass for the same power rating and provide higher torque density [28]. Also, multi-staged designs increase the modularity of the machine, which can create advantages in manufacturing, transportation, and maintenance for large power applications.
- Double-sided rotor discs are connected and locked together via the machine shaft, and there is no relative motion between them. This implies no changing magnetic field on the magnets and rotor yokes due to magnet excitation. This eliminates the eddy current losses on the windings due to magnet excitation, a critical issue for single-sided designs.

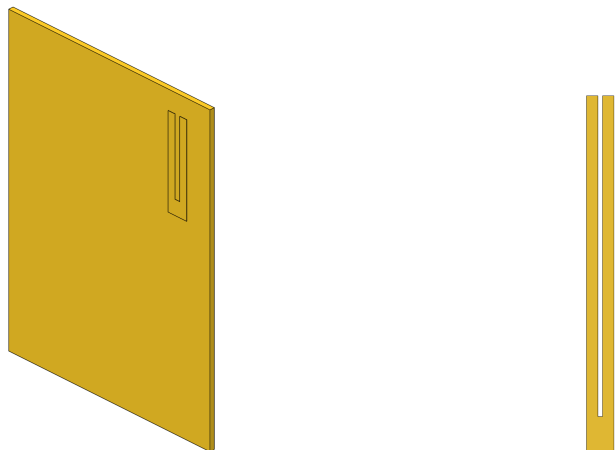


Figure 2.4: Manufacturing of flat wire from thin copper sheet using laser cutter

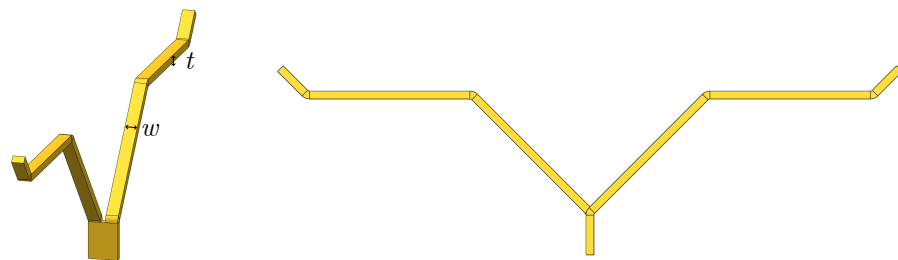
Thanks to the presented advantages, AFPM topology is an attractive solution for a variety of applications. The proposed machine is used in direct-drive in-wheel concepts for traction applications due to its small axial length and high torque density [29, 30, 31]. Flywheel energy storage systems are another possible application of AFPM because of its relative high moments of inertia [32, 33, 34]. Additionally, the proposed machine is used in wind energy systems as a wind turbine generator [35, 36, 37]. In this study, also, 1 MW direct-drive AFPM generator for wind turbines will be designed in Chapter 5.

2.3 Flat Winding Stator

Instead of conventional stranded wires, a novel flat winding topology is proposed in this study, which is made of thin conductor sheet using stamping press, water-jet, or laser as in Fig. 2.4. Flat winding is composed of many flat wires. The manufacturing stages of the flat wire is depicted in Fig. 2.5. This type of wire is manufactured from a thin conductor sheet, such as copper or aluminum. U-shaped conductors, as in Fig. 2.5b, are cut from the sheet using planar cutting tools such as laser or water jet. Then, the obtained piece is bent to give the final form of the flat wire, as shown in Fig.2.5c and Fig 2.5d. There are two bending points in a flat wire. This design selection significantly reduces the end windings and increase efficiency.



(a) U-shaped piece cut from thin conductor sheet
using laser cutter (b) Flat wire before bending step



(c) Flat wire final form (d) Flat wire final form side view

Figure 2.5: Manufacturing steps of the flat wire

The required number of flat wires are placed around an axis and connected to each other in various configurations to form an air-cored stator, as shown in Fig. 2.6. Two flat wires are connected electrically at their endpoints. Various welding technologies can be used for that purpose, depending on flat wire material. For example, the soldering is enough for copper flat wire material; however, advanced welding techniques may be required for other conductor materials. For aluminum, TIG or MIG welding can be used to weld flat wires together. Electrical isolation between two adjacent flat wires is ensured with high-temperature isolation papers located between them.

In Fig. 2.7, the manufactured prototype of a flat winding stator is given. This three phase stator is made of copper flat wires, and it is used in 1.4 kW prototype machine that will be presented in Chapter 4. In order to have mechanical rigidity, flat wires are

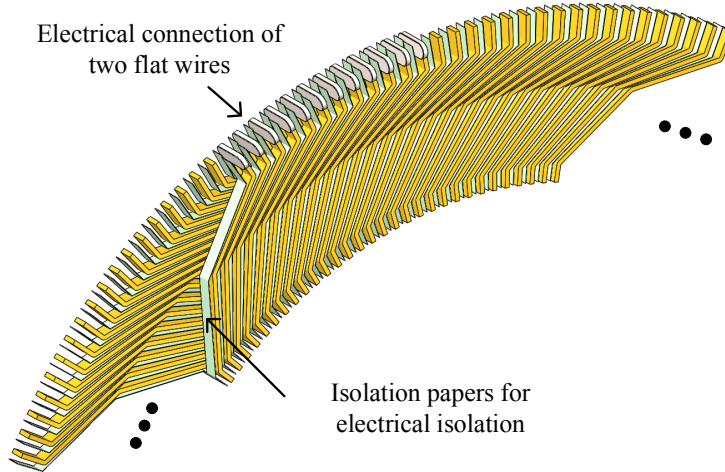


Figure 2.6: Flat wires forming the air-cored stator

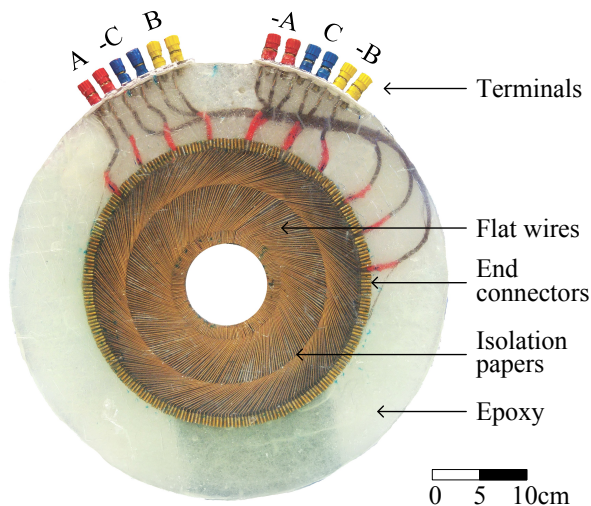


Figure 2.7: Manufactured copper flat wired stator

put inside the epoxy resin. It is important to have an epoxy resin with high thermal conductivity so that it can evacuate the heat out of the stator windings. Nevertheless, epoxy resins have lower thermal conductivity than conductors themselves. There may be some solutions for better thermal performance when the flat wires are partially coated with epoxy resin. Additionally, there may be some air bubbles in the epoxy during casting process. They may decrease the equivalent thermal conductivity of the stator and lead to some mechanical problems. In order to overcome this problem, the epoxy should be vacuumed to evacuate the air bubble inside it.

Compared to the conventional stranded wire, the flat wire has the following advantages:

- Flat winding topology provides ease of manufacturing with industrial automation tools because it involves only cutting and bending processes. It can be manufactured using commonly used automation tools such as laser or water-jet cutters, which reduces manufacturing cost and time in large volume productions.
- Thanks to its better thermal performance, superior current densities can be obtained. As it will be presented in Section 4.4, the proposed flat wire is capable of achieving current density of 7 A/mm^2 without forced cooling, which outperforms conventional wires.
- Due to its large cross-sectional area, high current ratings are achievable with flat wire, eliminating the necessity of making parallel winding connections as in the conventional stranded wired stators. It is known that making parallel winding connections may be problematic in some cases due to the circulating currents.
- The end winding lengths are significantly reduced in flat winding because series-connected flat wires are directly welded to each other at their endpoints without any wire connections, as shown in Fig. 2.6. This eliminates the losses in end windings and increases the efficiency of the machine.
- High fill factors can be achieved in flat winding topology due to the flat wire's rectangular-shaped cross-sectional area.
- Since the flat wires are cut from a thin conductor sheet, they are not covered with an insulating material such as enamel coating in stranded wires. Therefore, when the stator is partially coated with epoxy, as will be investigated in Section 5.3, it is easier to evacuate the heat out of conductors, which results in better thermal performance and higher electrical loadings.

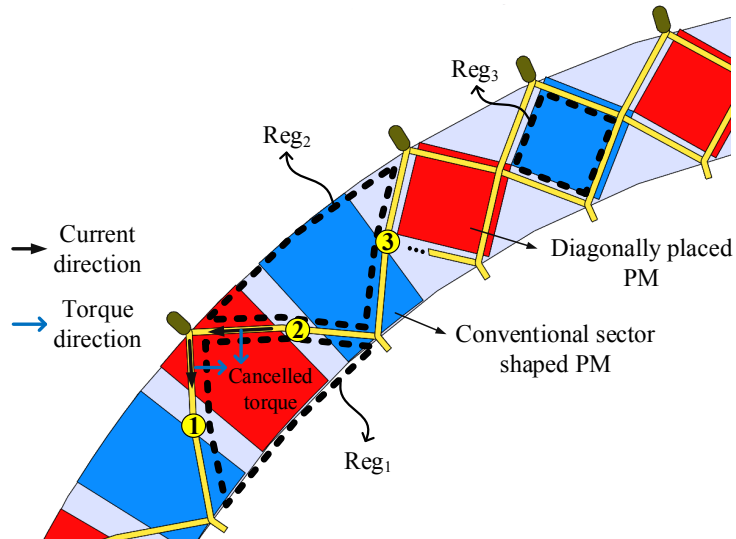


Figure 2.8: The evaluation of the different pole shapes

2.4 Rotor

The proposed AFPM topology's rotor structure consists of two rotor discs located at two sides of the air-cored flat winding stator. Strong NdFeB magnets are used to excite the rotor due to their high energy product. N42M grade NdFeB magnets with remanence flux density of 1.39 T are preferred. Two rotor discs are connected via a machine shaft, and they rotate synchronously. Since there is no relative motion between two rotor discs, permanent magnet excitation does not cause any eddy current losses on the magnets and rotor yokes.

Unlike the conventional sector shaped permanent magnets (PM) shown on the left side of the Fig. 2.8, the diagonally placed square shaped PMs shown on the right side of the same figure are preferred for the proposed topology. At this point, the selection of the PM or pole shape needs further investigation. The conventional sector shaped PMs are not suitable for the flat winding topology. Note that the usage of these magnets results in the cancellation of the torque produced on the flat wire conductors numbered 1 and 2 because they are under the effect of the same pole although they carry current at different directions. In order to prevent the torque cancellation on conductors 1 and 2, the pole area should be within the first region shown in Fig. 2.8. Similarly, to prevent the torque cancellation on conductors 2 and 3, the

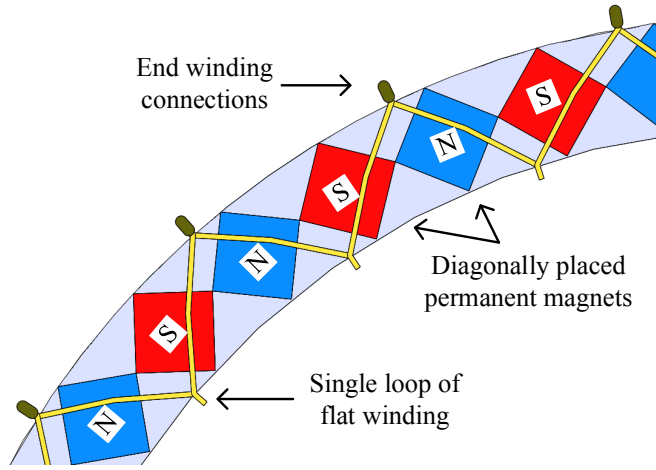


Figure 2.9: Single loop of flat winding with rotor structure employing diagonally placed permanent magnets

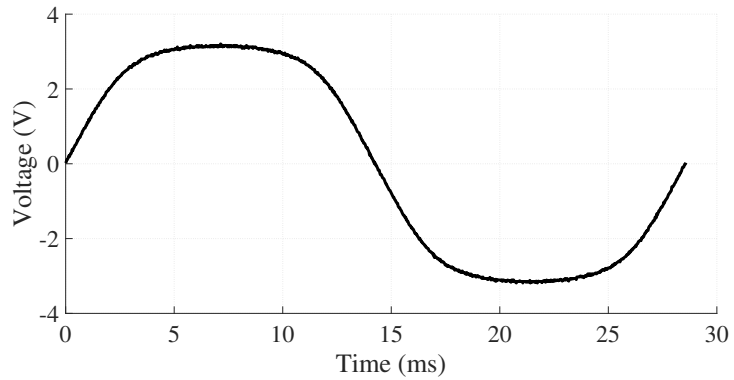


Figure 2.10: Induced voltage on a single loop of flat winding

pole area should be within the second region. Therefore, the actual pole area should be within the third region, which is the intersection of the first and second regions. Using finite element analysis, different PM or pole shapes, such as cylindrical, oval, or trapezoidal, are evaluated. It is seen that the maximum torque and flux linkage are obtained by full utilization of the allowed pole area. Thus, in the proposed design, diagonally placed square PMs are used on the rotor side.

In order to illustrate how voltage is induced on flat windings, in Fig. 2.9, a single loop of flat winding is shown with a rotor disc employing diagonally placed permanent magnets. When the rotor is rotated, the voltage waveform shown in Fig. 2.10 is induced on this single loop of flat winding.

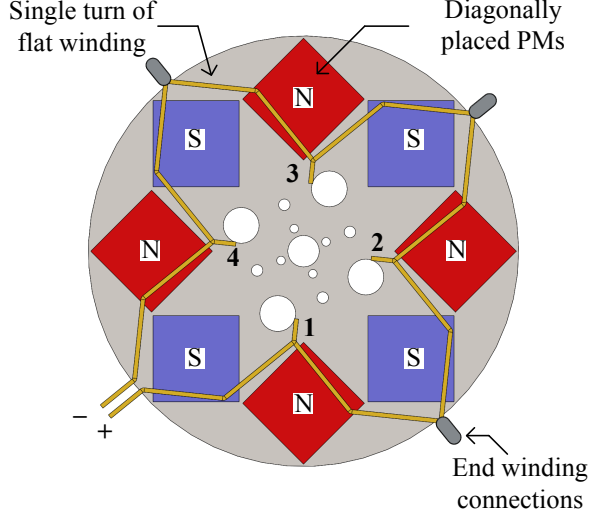


Figure 2.11: Single turn of flat winding composed of as many flat wires as the number of pole pairs

It is important to relate the flat winding topology and pole number in two aspects. First, the number of flat wires to form a single turn of winding depends on the pole number. There are as many flat wires as the number of pole pairs in a single turn of flat winding. To illustrate, the rotor and single turn of the flat winding structure are shared in Fig. 2.11, where there are four pole pairs and four flat wires forming a single loop of flat winding.

Secondly, the flat wire geometry also depends on the number of poles. The bending angles on a flat wire are shown in Fig. 2.12. The bending angle of the bending point at the middle of the flat winding is a function of pole number as follows

$$\beta = \frac{360^\circ}{p} \quad (2.1)$$

where β is the bending angle shown in Fig. 2.12 and p is the number of poles. The bending angles at the endpoints of flat wire are independent of pole number, and they are equal to 45° .

In Fig. 2.13, the rotor and stator structure of the proposed AFPM are shown in the exploded view. The air-cored flat winding stator is sandwiched between eight-pole rotor discs. The stator should be fixed to the outer frame of the machine.

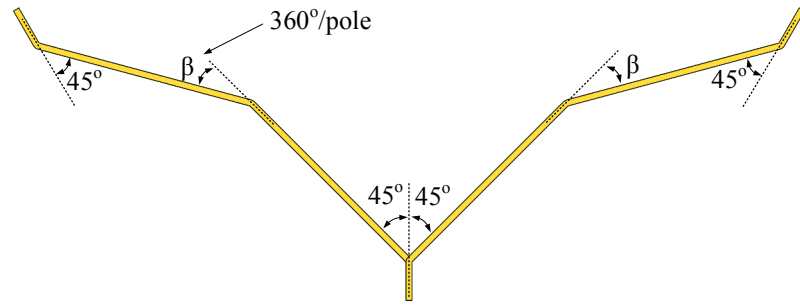


Figure 2.12: Bending angles of the flat wire

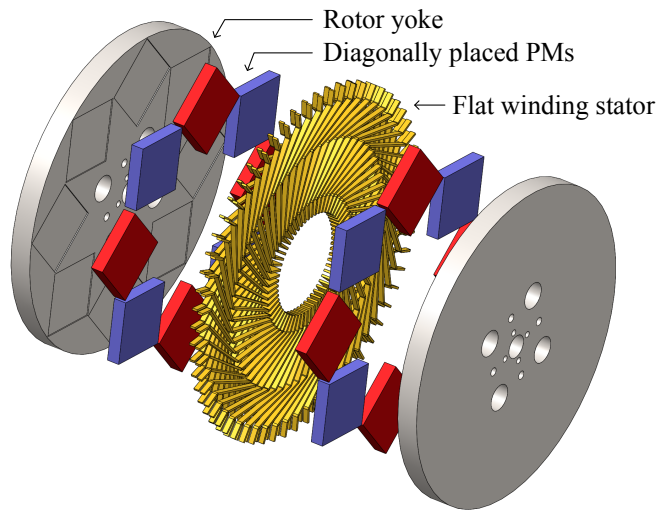


Figure 2.13: Exploded view of the proposed AFPM with novel flat winding

2.5 Design Challenges

There are several design challenges associated with the proposed AFPM topology as follows:

- Compared to the conventional stranded wire, the flat wire has a much larger cross-sectional area because it is made of a laser-cut conductor sheet. Therefore, if it is not well-designed, the windings may suffer from high eddy current losses on the windings due to external PM field. There are two solutions applied in this study to prevent this problem. First, it is known that the eddy current losses are proportional to the cross-sectional area of the conductor on the plane, which is perpendicular to the flux passing direction in the axial di-

rection in our case. Therefore, in order to limit the eddy current losses, a thin conductor sheet is used, generally 1 mm to 3 mm, while manufacturing of the flat wire. This limits the cross-sectional area, and thus, eddy current losses. Secondly, thin flat wires are stacked through the thickness in the circumferential direction, as seen in Fig. 2.6. In that way, on the plane in which eddy currents are created, the cross-sectional area is minimized, and eddy current losses are limited.

- Especially for low power and small diameter applications, the number of flat wires is limited due to space limitation in the circumferential direction. This limits the number of turns and results in low voltage, high current machines. For example, the manufactured prototype machine that will be presented in Chapter 4 has 300 mm diameter and 1.4 kW rated power. It has line voltage of 42 V and rated current of 20 A. On the machine side, this may not cause a problem; however, a high current rating on the drive side results in high conduction losses on the switches and may decrease the drive efficiency in low power and high current applications. As the machine's diameter and power rating increase, this problem is eliminated due to the high number of turns and large diameter.
- There are also a few mechanical issues that should be paid attention to this topology. Firstly, although the stator is air-cored, and there is no attraction between rotor and stator, there may be considerable attraction force between two rotor discs due to permanent magnets, resulting in an eccentricity fault. Therefore, the deflection analysis should be carried out for the rotor discs while designing the mechanical structure. Secondly, there are two air gaps in the topology. Therefore, the mechanical structure of the topology should be robust such that it preserves the air gap distances within the tolerances.

2.6 Summary

In order to investigate the performance of flat winding on a machine, this chapter presented the axial flux permanent magnet machine topology with a flat winding stator. First, the existing topologies and their properties are summarized. Then, axial flux permanent magnet topology with the double rotor and single stator configuration is

selected for the implementation. The advantages of the topology are presented, which include high torque density, no cogging torque, and stackability, etc. Also, possible applications of the proposed topology are investigated. Then, the air-cored stator is presented, which is made of flat wires. The manufacturing stages of flat wires are explained. It is seen that flat wires are made of a thin conductor sheet by cutting and bending operations. Electrically isolating flat wires and coating them with epoxy are followed steps of the manufacturing of the stator. Also, the advantages of the flat winding, such as ease of manufacturing and superior current ratings, are highlighted. Then, the details of the rotor employing diagonally placed permanent magnets are investigated. Lastly, in the chapter, the design challenges of the proposed topology are presented. Due to its large cross-sectional area, a flat winding stator has a high risk of eddy current losses on the windings due to external PM field. However, two solutions are presented for that problem. Also, for small diameter applications, the machine's induced voltage may be limited due to a limited number of turns. However, this can be overcome by connecting all windings in series. Lastly, some mechanical challenges are highlighted, and the chapter is concluded.

CHAPTER 3

ANALYTICAL MODELING OF THE MACHINE

In machine design and analysis, having an analytical model of the machine enables to quickly get the results without any time-consuming finite element analysis dependency. Especially in the optimization study, where designs with different geometries are evaluated at each iteration, and re-meshing is required, the analytical modeling saves too much time [38, 39].

Analytical modeling of the proposed machine starts with the derivation of the open circuit magnetic field model using magnetic scalar potential. Then, induced voltage and torque characteristics are derived. Analytical modeling of the DC winding losses and eddy current losses on the windings due to external PM field are also presented for efficiency calculations, and the results are compared with finite element simulations. Lastly, an analytical model for deflection of the rotor cores is presented.

3.1 Magnetic Field Modeling

There are different methods presented in the literature for the magnetic field analysis of permanent magnet machines. In [40, 41, 42], authors used magnetic scalar potential to derive the magnetic field. A quasi 3D computational method using vector potential is developed in [43, 44]. In this study, field analysis of the proposed axial flux permanent magnet machine is carried out using magnetic scalar potential with the help of Fourier analysis and Laplace equations. This method provides accurate modeling of the magnetic field of permanent magnet machines using a 2D representation of the model.

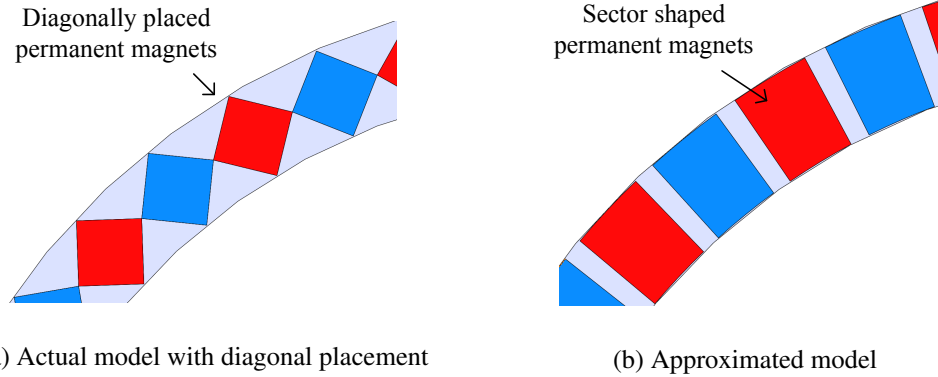


Figure 3.1: Approximation of the permanent magnets

Permanent magnets create the magnetic field in the air gap on the rotor. This field can be distorted by the magnetic field created by current-carrying armature coils on the stator, called armature reaction. However, the proposed topology is air-cored and has a large magnetic air gap compared to iron-cored machines. Therefore, armature reaction is low and negligible [45, 46, 47]. Accordingly, only no-load magnetic field by permanent magnets are considered in the study.

In the analysis, the following assumptions are made to simplify the model:

- There is no uniform 2D representation of the permanent magnets due to their diagonal placement as in Fig. 3.1a. Therefore, they have approximated as sector shaped magnets with 0.78 magnet to pole pitch ratio as in Fig. 3.1b. This approximation creates a small difference at the third harmonic of the magnetic field, but the fundamental components are in good agreement, as shown later in this chapter.
- The rotor cores are assumed to be infinitely magnetic permeable and have linear B-H characteristics.
- The permanent magnets have uniform magnetization with a constant relative permeability of 1.05.
- The proposed machine has a double-sided rotor. However, the magnetic field analysis is conducted for a single-sided rotor structure for simplicity, and the superposition principle is used to get the actual field model.

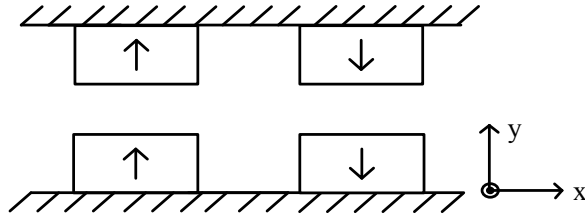


Figure 3.2: 2D representation of the simplified model

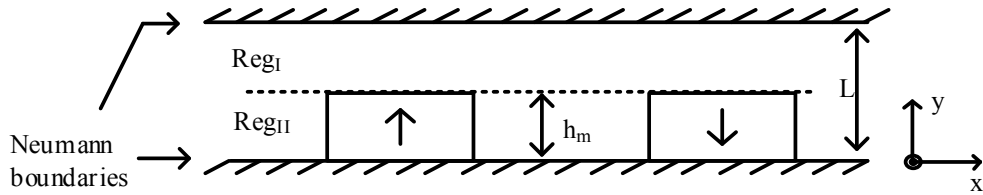


Figure 3.3: Two regions representing the magnetic field: air and magnet regions [48]

The 2D representation of the simplified model is shown in Fig. 3.2 for one pole pair. Note that the stator windings are not shown in the figure because the winding current is zero in open circuit magnetic field analysis and the windings are inactive. The 2D model is presented on Cartesian coordinates, where the x-axis is on the circumferential direction, and the y-axis is on the machine's axial direction.

In order to reduce computational load, the field analysis is conducted over single-sided rotor topology. The actual field of double-sided topology is derived from this analysis using the superposition principle. 2D representation of the single-sided topology is presented in Fig. 3.3. In the analysis, two regions are representing the model: the air region labeled as Reg_I and the magnet region labeled as Reg_{II} , as shown in Fig. 3.3. In the figure, h_m represents the magnet thickness in the axial direction, and L represents the distance between two rotor yokes. The Neumann boundaries represent the boundaries of the infinitely permeable core.

The magnetic field analysis starts with an analytical representation of the magnetization of the magnets. Note that the magnets are magnetized in the y-direction, which represents the axial direction. Therefore, there is no magnetization vector component in the x-direction and z-direction. Considering this, magnetization characteristics can

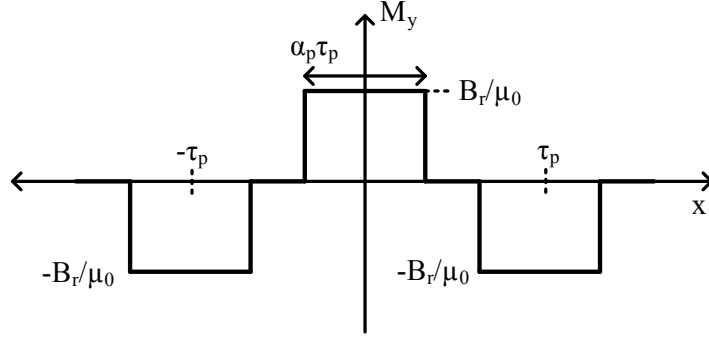


Figure 3.4: Magnetization characteristics of permanent magnets [48]

be depicted as in Fig. 3.4. In the figure, B_r , τ_p , α_p , and μ_0 stand for remanence flux density, pole pitch, the magnet to pole pitch ratio, and permeability of free space, respectively.

The magnetization vector of the permanent magnets has only y-component, which only depends on x-variable. Therefore, it can be written as

$$\vec{M} = M_y(x) \cdot \vec{a}_y \quad (3.1)$$

where \vec{a}_y is unit vector in the y-direction. The analytical expression of y-component of the magnetization vector, M_y , can be obtained using Fourier series representation. The details of Fourier series representation for magnetization can be found in Appendix A. At the end, y-component of magnetization vector can be expressed as

$$M_y(x) = \sum_{n=1}^{\infty} m_{y_{cs}} \cos\left(\frac{\pi n}{\tau_p} x\right) \quad (3.2)$$

and

$$m_{y_{cs}} = \frac{4 B_r}{\pi n \mu_0} \sin\left(\frac{\pi n \alpha_p}{2}\right) \sin^2\left(\frac{\pi n}{2}\right) \quad (3.3)$$

where n stands for n^{th} order space harmonic. Note that since y-component of the magnetization vector is an even function, its Fourier series expansion does not involve the terms with sines.

As stated in [40], the magnetic scalar potential and magnetization vector is related as

$$\nabla^2 \varphi = \frac{1}{\mu_r} \nabla \cdot \vec{M} \quad (3.4)$$

where φ and μ_r stand for magnetic scalar potential and relative permeability, respectively.

Note that in the air region, Reg_I , there is no magnetization source. Therefore, Laplacian of the magnetic scalar potential in Reg_I is zero.

$$\nabla^2 \varphi_I = 0 \quad (3.5)$$

Using (3.4), the Laplacian of the magnetic scalar potential in Reg_{II} can be stated as

$$\nabla^2 \varphi_{II} = \frac{1}{\mu_r} \nabla \cdot \vec{M} = \frac{1}{\mu_r} \left(\frac{\partial M_x}{\partial x} + \frac{\partial M_y}{\partial y} + \frac{\partial M_z}{\partial z} \right) \quad (3.6)$$

As stated in (3.1), magnetization vector in magnet region has only y-component, M_y , which only depends on x-variable. Therefore, it can be written

$$\nabla^2 \varphi_{II} = \frac{1}{\mu_r} \frac{\partial M_y(x)}{\partial y} = 0 \quad (3.7)$$

It is shown that in both air and magnet regions, Laplacian of magnetic scalar potential is zero as shown in (3.5) and (3.7). Therefore, the solution of the magnetic scalar potential is governed by Laplace's equation in both regions as stated in [41], and can be written as

$$\varphi_I = \sum_{n=1}^{\infty} \left(C_1 e^{\pi ny/\tau_p} + C_2 e^{-\pi ny/\tau_p} \right) \cos \left(\frac{\pi n}{\tau_p} x \right) \quad (3.8)$$

$$\varphi_{II} = \sum_{n=1}^{\infty} \left(C_3 e^{\pi ny/\tau_p} + C_4 e^{-\pi ny/\tau_p} \right) \cos \left(\frac{\pi n}{\tau_p} x \right) \quad (3.9)$$

where C_{1-4} are unknown coefficients to be determined by the boundary conditions. It is known that magnetic field strength, \vec{H} , and magnetic scalar potential, φ , have the following relation as stated in [42]

$$\vec{H} = -\nabla \varphi \quad (3.10)$$

$$H_x = -\frac{\partial \varphi}{\partial x} \quad (3.11)$$

$$H_y = -\frac{\partial \varphi}{\partial y} \quad (3.12)$$

Therefore, magnetic field strength, \vec{H} , can be derived in both regions by taking gradient of the magnetic scalar potential as follows

$$H_{Ix} = \frac{\pi n}{\tau_p} \sum_{n=1}^{\infty} \left(C_1 e^{\pi ny/\tau_p} + C_2 e^{-\pi ny/\tau_p} \right) \sin \left(\frac{\pi n}{\tau_p} x \right) \quad (3.13)$$

$$H_{Iy} = - \frac{\pi n}{\tau_p} \sum_{n=1}^{\infty} \left(C_1 e^{\pi ny/\tau_p} - C_2 e^{-\pi ny/\tau_p} \right) \cos \left(\frac{\pi n}{\tau_p} x \right) \quad (3.14)$$

$$H_{IIx} = \frac{\pi n}{\tau_p} \sum_{n=1}^{\infty} \left(C_3 e^{\pi ny/\tau_p} + C_4 e^{-\pi ny/\tau_p} \right) \sin \left(\frac{\pi n}{\tau_p} x \right) \quad (3.15)$$

$$H_{Ily} = - \frac{\pi n}{\tau_p} \sum_{n=1}^{\infty} \left(C_3 e^{\pi ny/\tau_p} - C_4 e^{-\pi ny/\tau_p} \right) \cos \left(\frac{\pi n}{\tau_p} x \right) \quad (3.16)$$

Magnetic field strength, \vec{H} , is linked to the magnetic flux density, \vec{B} , with constitutive relation in both regions as follows

$$\vec{B} = \mu_0 \mu_r \vec{H} + \mu_0 \vec{M} \quad (3.17)$$

Note that in air region, Reg_I , there is no source of magnetization and relative permeability is unity. Therefore, the constitutive relation in the air region can be written as

$$\vec{B}_I = \mu_0 \vec{H}_I \quad (3.18)$$

$$B_{Ix} = \mu_0 H_{Ix} \quad \text{and} \quad B_{Iy} = \mu_0 H_{Iy} \quad (3.19)$$

In magnet region, permanent magnets are the source of magnetization and relative permeability is close to unity. Also, remember that the magnetization vector has only y-component, which represents axial direction. Therefore, the constitutive relation in magnet region, Reg_{II} , can be written as

$$\vec{B}_{II} = \mu_0 \mu_r \vec{H}_{II} + \mu_0 \vec{M} \quad (3.20)$$

$$B_{IIx} = \mu_0 \mu_r H_{IIx} \quad (3.21)$$

$$B_{Ily} = \mu_0 \mu_r H_{Ily} + \mu_0 M_y \quad (3.22)$$

Therefore, magnetic flux density, \vec{B} , in both regions can be written using (3.19), (3.21) and (3.22) as

$$B_{Ix} = \frac{\pi n \mu_0}{\tau_p} \sum_{n=1}^{\infty} \left(C_1 e^{\pi ny/\tau_p} + C_2 e^{-\pi ny/\tau_p} \right) \sin \left(\frac{\pi n}{\tau_p} x \right) \quad (3.23)$$

$$B_{Iy} = - \frac{\pi n \mu_0}{\tau_p} \sum_{n=1}^{\infty} \left(C_1 e^{\pi ny/\tau_p} - C_2 e^{-\pi ny/\tau_p} \right) \cos \left(\frac{\pi n}{\tau_p} x \right) \quad (3.24)$$

$$B_{IIx} = \frac{\pi n \mu_0 \mu_r}{\tau_p} \sum_{n=1}^{\infty} \left(C_3 e^{\pi ny/\tau_p} + C_4 e^{-\pi ny/\tau_p} \right) \sin \left(\frac{\pi n}{\tau_p} x \right) \quad (3.25)$$

$$\begin{aligned} B_{Iiy} = & - \frac{\pi n \mu_0 \mu_r}{\tau_p} \sum_{n=1}^{\infty} \left(C_3 e^{\pi ny/\tau_p} - C_4 e^{-\pi ny/\tau_p} \right) \cos \left(\frac{\pi n}{\tau_p} x \right) \\ & + \mu_0 \sum_{n=1}^{\infty} m_{ycs} \cos \left(\frac{\pi n}{\tau_p} x \right) \end{aligned} \quad (3.26)$$

where m_{ycs} is Fourier coefficients of the cosine terms given in (3.3).

The last step of the derivation of the magnetic field is finding the unknown coefficients, C_{1-4} . There are four unknown coefficients in the field equations. In order to find these coefficients, four boundary conditions should be considered. These boundary conditions can be listed as follows:

- There is no magnetic field outside of Neumann boundaries [42]. Therefore, the magnetic field at the boundaries of the infinitely permeable core is zero.
- Considering that there is no surface current at the boundary, the tangential component of magnetic field strength, \vec{H} , is continuous.
- At the boundary of two regions, the normal component of magnetic flux density, \vec{B} , is continuous.

Therefore, four boundary conditions can be written analytically as

$$H_{Ix}|_{y=L} = 0 \quad (3.27)$$

$$H_{IIx}|_{y=0} = 0 \quad (3.28)$$

$$H_{Ix}|_{y=h_m} = H_{IIx}|_{y=h_m} \quad (3.29)$$

$$B_{Iy}|_{y=h_m} = B_{Iiy}|_{y=h_m} \quad (3.30)$$

Note that these boundary conditions are valid for all x-values, representing circumferential direction. Also, they should hold for every harmonic component of the magnetic field. Therefore, combining (3.13), (3.15), (3.24) and (3.26) with boundary conditions in (3.27) to (3.30), one can get the following

$$C_1 e^{\pi n L / \tau_p} + C_2 e^{-\pi n L / \tau_p} = 0 \quad (3.31)$$

$$C_3 + C_4 = 0 \quad (3.32)$$

$$C_1 e^{\pi n h_m / \tau_p} + C_2 e^{-\pi n h_m / \tau_p} = C_3 e^{\pi n h_m / \tau_p} + C_4 e^{-\pi n h_m / \tau_p} \quad (3.33)$$

$$\begin{aligned} -\frac{\pi n}{\tau_p} C_1 e^{\pi n h_m / \tau_p} + \frac{\pi n}{\tau_p} C_2 e^{-\pi n h_m / \tau_p} &= -\frac{\pi n \mu_r}{\tau_p} C_3 e^{\pi n h_m / \tau_p} \\ &\quad + \frac{\pi n \mu_r}{\tau_p} C_4 e^{-\pi n h_m / \tau_p} + m_{y_{cs}} \end{aligned} \quad (3.34)$$

Rearranging the equations results in

$$e^{\pi n L / \tau_p} C_1 + e^{-\pi n L / \tau_p} C_2 = 0 \quad (3.35)$$

$$C_3 + C_4 = 0 \quad (3.36)$$

$$e^{\pi n h_m / \tau_p} (C_1 - C_3) + e^{-\pi n h_m / \tau_p} (C_2 - C_4) = 0 \quad (3.37)$$

$$e^{\pi n h_m / \tau_p} \left(\frac{\pi n \mu_r}{\tau_p} C_3 - \frac{\pi n}{\tau_p} C_1 \right) + e^{-\pi n h_m / \tau_p} \left(\frac{\pi n}{\tau_p} C_2 - \frac{\pi n \mu_r}{\tau_p} C_4 \right) = m_{y_{cs}} \quad (3.38)$$

In order to find the unknown coefficients, C_{1-4} , the boundary condition equations given in (3.35) to (3.38) can be put into matrix form. In order to do this, the exponential terms are represented as follows

$$E_1 = e^{\pi n L / \tau_p} \quad \text{and} \quad E_2 = e^{-\pi n L / \tau_p} \quad (3.39)$$

$$E_3 = e^{\pi n h_m / \tau_p} \quad \text{and} \quad E_4 = e^{-\pi n h_m / \tau_p} \quad (3.40)$$

Then, the boundary condition equations can be represented in the matrix form as follows

$$\begin{bmatrix} E_1 & E_2 & 0 & 0 \\ 0 & 0 & 1 & 1 \\ E_3 & E_4 & -E_3 & -E_4 \\ -\frac{\pi n}{\tau_p} E_3 & \frac{\pi n}{\tau_p} E_4 & \frac{\pi n \mu_r}{\tau_p} E_3 & -\frac{\pi n \mu_r}{\tau_p} E_4 \end{bmatrix} \begin{bmatrix} C_1 \\ C_2 \\ C_3 \\ C_4 \end{bmatrix} = \begin{bmatrix} 0 \\ 0 \\ 0 \\ m_{y_{cs}} \end{bmatrix} \quad (3.41)$$

Note that the matrix equation in (3.41) should hold for all harmonic components, n . In order to derive magnetic field of the proposed machine, finite number of harmonics, say N , should be considered. Therefore, the matrix equation in (3.41) should be modified so that it includes the solution for all harmonics as follow

$$\begin{bmatrix} \mathbf{E}_1 & \mathbf{E}_2 & \mathbf{0} & \mathbf{0} \\ \mathbf{0} & \mathbf{0} & \mathbf{I} & \mathbf{I} \\ \mathbf{E}_3 & \mathbf{E}_4 & -\mathbf{E}_3 & -\mathbf{E}_4 \\ -\mathbf{M} \cdot \mathbf{E}_3 & \mathbf{M} \cdot \mathbf{E}_4 & \mu_r \mathbf{M} \cdot \mathbf{E}_3 & -\mu_r \mathbf{M} \cdot \mathbf{E}_4 \end{bmatrix} \begin{bmatrix} \mathbf{C}_1 \\ \mathbf{C}_2 \\ \mathbf{C}_3 \\ \mathbf{C}_4 \end{bmatrix} = \begin{bmatrix} \mathbf{0} \\ \mathbf{0} \\ \mathbf{0} \\ \mathbf{M}_{\text{yes}} \end{bmatrix} \quad (3.42)$$

where \mathbf{E}_{1-4} are $N \times N$ diagonal matrices employing only exponential terms given in (3.39) and (3.40). \mathbf{M} is also $N \times N$ diagonal matrix containing $(\pi n / \tau_p)$ terms. Lastly, \mathbf{C}_{1-4} and \mathbf{M}_{yes} are single column matrices with $N \times 1$ size. Then, the matrix equation in (3.42) can be simplified as

$$\mathbf{E} \cdot \mathbf{C} = \mathbf{Y} \quad (3.43)$$

where \mathbf{E} is $4N \times 4N$ square matrix, and \mathbf{C} and \mathbf{Y} are $4N \times 1$ matrices. Then, the unknown coefficient matrix, \mathbf{C} , can be obtained with matrix inversion operation easily, using computational tools, such as MATLAB, as follows

$$\mathbf{C} = \mathbf{E}^{-1} \cdot \mathbf{Y} \quad (3.44)$$

The entities of the solved \mathbf{C} matrix are coefficients, C_{1-4} , that is used in the magnetic field equations in (3.23) to (3.26). Therefore, with this derivation, one can find the axial and circumferential components of the magnetic flux density in the air gap for each harmonic component.

Remember that this derivation is carried out for single-sided rotor topology. However, the proposed machine has a double-sided rotor structure, as in Fig. 3.2, and the field solutions have to be obtained for this configuration. In order to achieve this, the superposition principle is used as depicted in Fig. 3.5. Field constructed in double-sided rotor topology is simply the superposition of the fields constructed by two single-sided rotor topologies.

The presented analytical model is implemented on MATLAB, and the files can be found in Appendix C.

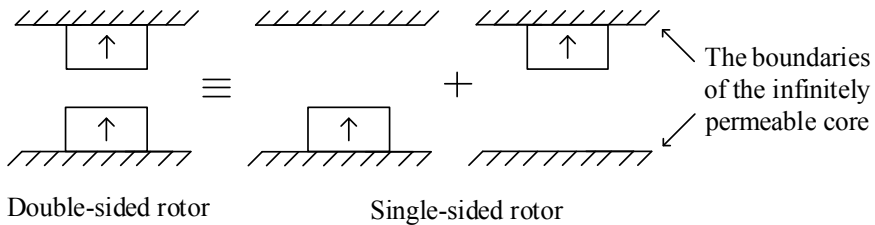


Figure 3.5: Superposition principle used for the field analysis of double-sided rotor structure

Table 3.1: Specifications of the selected machine for validation of field modeling

| Parameter | Value |
|---------------------------|---------|
| Rated power | 1 MW |
| Rotational speed | 20 rpm |
| Diameter | 4.8 m |
| Number of poles | 46 |
| Magnet grade | N42M |
| Remanence flux density | 1.29 T |
| Magnet to magnet distance | 47.3 mm |
| Magnet thickness | 36.5 mm |

In order to measure the accuracy of the proposed analytical method, a machine is selected, and its magnetic flux density is obtained analytically. Also, the magnetic flux density is obtained using finite element analysis (FEA), and these two results are compared. The specifications of the selected machine can be seen in Table 3.1. It is 1 MW axial flux permanent magnet machine that contains double-sided rotor discs with diagonally placed permanent magnets. For the FEA, ANSYS Maxwell is used, and the flux density is obtained on the middle plane of the air gap of the generator as in Fig. 3.6.

For the comparison purpose, magnetic flux density distribution at the mean radius of the generator is obtained using the proposed analytical method and compared with 3D FEA simulations. The results are presented in Fig. 3.7a for one pole pair. Also, in Fig. 3.7b, the harmonics of the flux density obtained using the analytical model

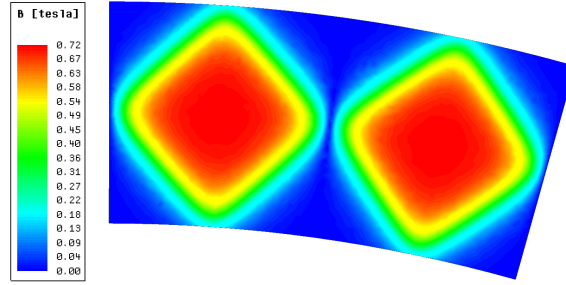
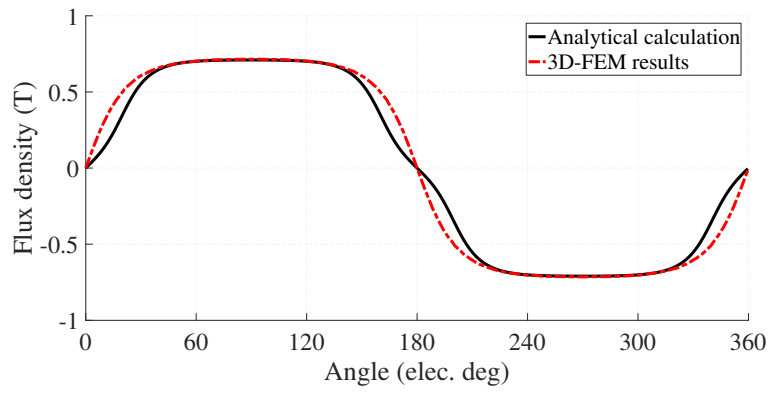
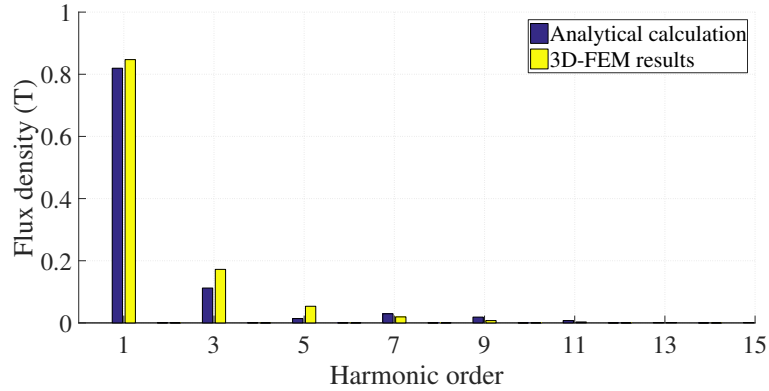


Figure 3.6: Flux density distribution of the analyzed machine obtained using FEA



(a) Spatial distribution comparison



(b) Harmonic distribution comparison

Figure 3.7: Comparison of no-load air gap magnetic flux density at mean radius

and FEA are compared. The results show that there is 3 % difference fundamental components. A slight difference at the third-order harmonics is caused by the sector shaped approximation of the diagonally placed magnets shown in Fig. 3.1. Overall, the results are in good agreement with each other.

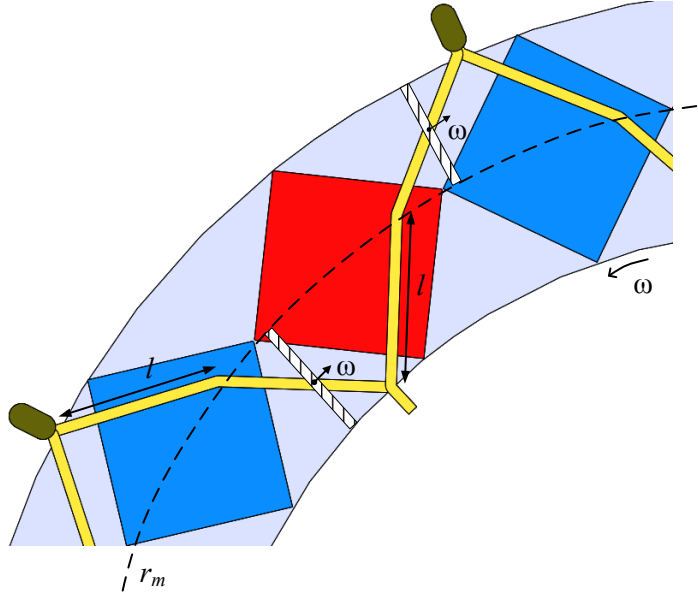


Figure 3.8: Voltage generation of a portion of a single loop of flat winding

3.2 Induced Voltage and Torque Characteristics

With the help of the proposed magnetic field model, the induced voltage and torque equations can be derived easily. A portion of the single loop of flat winding is shown in Fig. 3.8 with a rotor rotational speed of ω . In a single flat wire shown in Fig. 2.5c, there are four conductors, each with length l as in Fig. 3.8. Note that the voltage is induced on the parts that are perpendicular to both flux passing and velocity directions. That is, the induced voltage is proportional to the length of the radial projection of the flat wire as in Fig. 3.8. Also, the induced voltage is proportional with rotational speed, radius, and number of flat wires. Therefore, the induced phase voltage of the generator is given as

$$V_{ph} = B_y \omega r_m \frac{l}{\sqrt{2}} 2 a b k_w \quad (3.45)$$

where V_{ph} is the rms induced phase voltage, B_y is the rms flux density at the air gap, ω is the rotational speed, r_m is the mean radius as in Fig. 3.8, a is the number of series-connected flat wires per phase per stage, b is the number of series-connected stages, and k_w is the winding factor of the flat winding stator. By considering the harmonics of flux density and their corresponding winding factors, the induced voltage for each harmonic can be calculated.

The output torque of the three phase machine, T , can be obtained using phase current and derived induced voltage equation as

$$T = 3 B_y r_m \frac{l}{\sqrt{2}} 2 a k_w I_{ph} s \quad (3.46)$$

where I_{ph} is the phase current of each stage, and s is the total number of stages.

3.3 Loss Modeling

Loss modeling is an important step to have accurate efficiency estimation. For the proposed machine topology, the losses of the machine can be categorized into four classes, as in Fig. 3.9. Throughout the thesis, the core losses on rotor discs and permanent magnet (PM) losses are ignored because two rotor discs are rotating synchronously, and there is no source of changing magnetic field, except the one due to ignorable armature reaction. The mechanical losses are considered experimentally in the following chapter. Additionally, there are three types of winding losses. DC winding loss, also known as I^2R loss, is caused by the current flowing through the windings with homogeneous current density distribution. Due to low operating frequencies, AC winding loss due to skin and proximity effect is ignored throughout the thesis. Due to the large cross-sectional area of the flat wire, eddy current loss on winding conductors due to external PM field becomes comparable with DC winding loss, and it is considered in the analysis of the machine.

In this section, both DC winding losses and eddy current losses on flat windings due to external PM field are derived analytically. The DC winding losses can be derived easily by calculating the phase resistance at each stage, R_{ph} , using flat wire geometry, and paying attention to the series or parallel connections. Then, the DC winding losses, P_c , can be derived as

$$P_c = s 3 I_{ph}^2 R_{ph} \quad (3.47)$$

Attention should be paid to analytical modeling of the eddy current losses on the windings due to external PM field. In the proposed machine, flat wired stator made of conductor sheet is used. Since the flat wire has a large cross-sectional area, it has

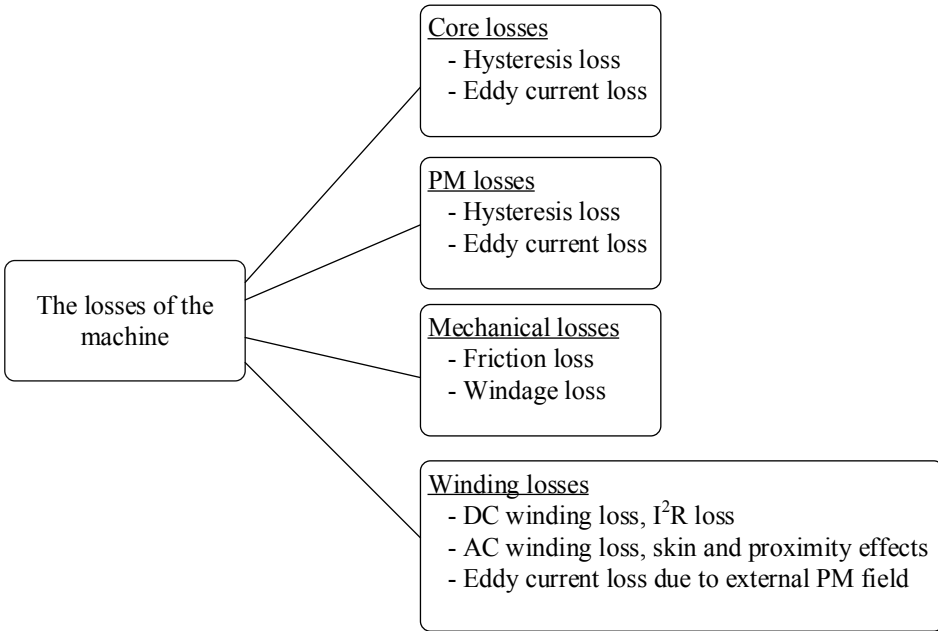


Figure 3.9: Losses of the proposed machine

a risk of high eddy current losses on the windings due to external PM field compared to conventional stranded wires.

For the calculation of eddy current loss on the windings due to external PM field, the method proposed in [49] is used. In the analysis, it is assumed that there is a changing magnetic field on the conductor material with dimensions, t and l as shown in Fig. 3.10, where $t \ll l$. Then, the volumetric specific loss due to eddy currents on the windings due to external PM field, P_{sp} , in W/m^3 is calculated as

$$P_{sp} = \frac{t^2 (2\pi f_e)^2 \hat{B}_{1y}^2}{24 \rho} k_1 \quad (3.48)$$

where f_e is the electrical frequency, \hat{B}_{1y} is the peak flux density of the fundamental component in y -direction, ρ is the resistivity of the flat wire material and k_1 is the factor that includes the effect of harmonics as

$$k_1 = \frac{\hat{B}_{1y}^2 + 3^2 \hat{B}_{3y}^2 + 5^2 \hat{B}_{5y}^2 + \dots}{\hat{B}_y^2} \quad (3.49)$$

where \hat{B}_{ny} is the peak flux density of the n^{th} harmonic component in the y -direction, and \hat{B}_y is the peak flux density in the y -direction including all harmonics. In order

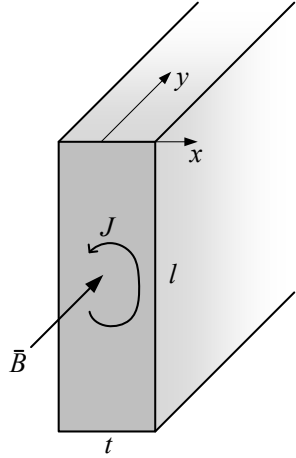


Figure 3.10: Eddy current loss on a conductor due to external PM field

to find the specific eddy current loss on the flat wires due to external PM field, the magnetic field on the conductors should be obtained in x , y , and z directions using the magnetic field derived in the previous section. While deriving the relation, the angular placement of the flat wire conductors should be taken into consideration because flat wire conductors are not aligned in the radial direction, as shown in Fig. 3.8. The specific eddy current loss on the windings due to external PM field will be the sum of specific eddy current losses obtained by the magnetic fields in x , y , and z directions using (3.48). Then, eddy current losses on the windings due to external PM field can be calculated using the total volume of the flat wires.

In order to measure the accuracy of the proposed analytical loss model, a machine is selected for loss calculation. The selected machine is the optimized 1 MW permanent magnet generator for direct-drive wind turbines, which will be studied in Chapter 5. The same machine was also used for analytical field model validation studied in Section 3.1. The summary of the specifications of the selected machine is given in Table 3.2.

The DC winding losses and eddy current losses on the windings due to external PM field of the selected machine are calculated using both the analytical model and finite element analysis. ANSYS Maxwell 3D solver is used for the analysis, and the results are tabulated in Table 3.3. There is a 5.7% difference in the eddy current losses on the windings due to external PM field, mainly caused by a slight difference in analytical

Table 3.2: Specifications of the selected machine for loss modeling validation

| Parameter | Value |
|---------------------------|-----------------------|
| Rated power | 1 MW |
| Rotational speed | 20 rpm |
| Diameter | 4.8 m |
| Electrical frequency | 7.7 Hz |
| Number of poles | 46 |
| Number of stages | 2 |
| Phase current | 850 A |
| Current density | 3.8 A/mm ² |
| Flat wire thickness, t | 3 mm |
| Air gap peak flux density | 0.85 T |

Table 3.3: Comparison of the losses obtained by analytical model and finite element analysis, for the selected machine

| Eddy current losses on windings | | |
|---------------------------------|--------------------------|-------------------|
| | due to external PM field | DC winding losses |
| Analytical model | 33.17 kW | 75.54 kW |
| Finite element analysis | 31.39 kW | 75.56 kW |

calculation of the flux density given in Fig. 3.7b. Remember that this dissimilarity is originated from the sector shaped magnet approximation of diagonally placed permanent magnets, as given in Fig. 3.1.

The DC winding losses losses are in good agreement with less than 0.1 % difference. It is seen that DC winding losses dominate the eddy current losses on the windings due to external PM field because of two main characteristics of the selected machine. Firstly, in direct-drive wind turbine applications, the rotational speed is low; therefore, the induced voltage frequency is low. Since the eddy current losses on the windings due to external PM field are proportional to the square of the electrical frequency, as stated in (3.48), low electrical frequency results in decreased eddy current losses

on the conductors. As presented in Table 3.2, the selected machine has the number of poles of 46, the rotational speed of 20 rpm, and induced voltage frequency of 7.7 Hz. Secondly, the eddy current losses on the windings due to external PM field are proportional to the square of the copper sheet material thickness, t , from which flat wire is manufactured. Due to high efficiency purposes, the selected machine employs thin flat wires with only 3 mm thickness, which effectively limits the eddy current losses on the windings due to external PM field.

3.4 Deflection Analysis

Deflection analysis is an essential step in the mechanical design stage. The deflection can be defined as the displacement of the materials under mechanical load conditions. In this case, the deflection occurs due to Maxwell stress on rotor discs caused by the permanent magnets. Since the stator is air-cored, there is no mechanical stress that causes deflection on the stator. The displacement of the rotor discs due to Maxwell stress should be measured to ensure that the maximum allowed displacement into the air gap is not exceeded. In general, the maximum allowed displacement due to deflection should be maximum 10 % of the air gap clearance as a rule of thumb [23, 50].

In the study, the deflection analysis of the rotor cores is carried out both analytically and using finite element methods. For the analytical analysis, circular plate theory by Young and Budynas [51] is used. The model representing the proposed axial flux topology can be seen in Fig. 3.11. In the figure, the shaft and one of the rotor discs are displayed. Maxwell stress caused by the permanent magnets creates a mechanical load on the rotor disc. This stress causes deflection of the rotor discs, resulting in a displacement into the air gap. In Fig. 3.11, q is Maxwell stress by permanent magnets, a_r is the outer radius of the rotor disc, b_r is shaft radius, and r_o is the inner radius of the area occupied by the permanent magnets. Note that the inner edge of the rotor disc is fixed to the shaft, and it is assumed that there is no displacement here. The outer edge is free, and the maximum displacement occurs at the outer edge, a_r , for the proposed topology.

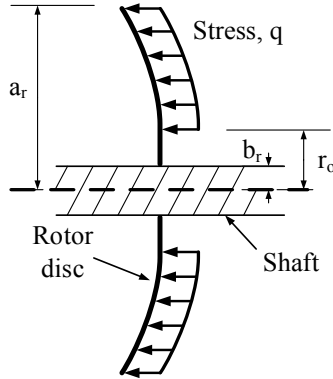


Figure 3.11: Circular plate model of rotor disc for analytical deflection analysis [50]

For the model in Fig. 3.11, the maximum displacement into the air gap, which is at outer edge of the rotor disc, can be calculated as follows [50, 51]

$$y = M_{rb} \frac{a_r^2}{D} C_2 + Q_b \frac{a_r^3}{D} C_3 - q \frac{a_r^4}{D} L_{11} \quad (3.50)$$

where y is the displacement at the outer radius, M_{rb} is the unit radial bending moment at the shaft, D is the plate constant, and Q_b is the unit shear force at the shaft [50]. They can be calculated as follows

$$M_{rb} = -q \frac{a_r^2}{C_8} \left[\frac{C_9}{2a_r b_r} (a_r^2 - r_o^2) - L_{17} \right] \quad (3.51)$$

$$D = \frac{E t_c^3}{12(1-\nu^2)} \quad (3.52)$$

$$Q_b = \frac{q}{2b_r} (a_r^2 - r_o^2) \quad (3.53)$$

where E and ν are the Young's Modulus and Poisson ratio of the core material, respectively, and t_c is the rotor core thickness in the axial direction. The constants C_2 , C_3 , C_8 , C_9 , L_{11} , and L_{17} depend on the model geometry and material properties. These constants are shared in Appendix B.

At this point, Maxwell stress used in the deflection analysis, q , needs special attention. In the circular plate model in Fig. 3.11, it is assumed that a constant and uniformly distributed stress is applied to the rotor discs between the inner radius, r_o , and the outer radius, a_r . However, in the proposed machine, the permanent magnets are placed

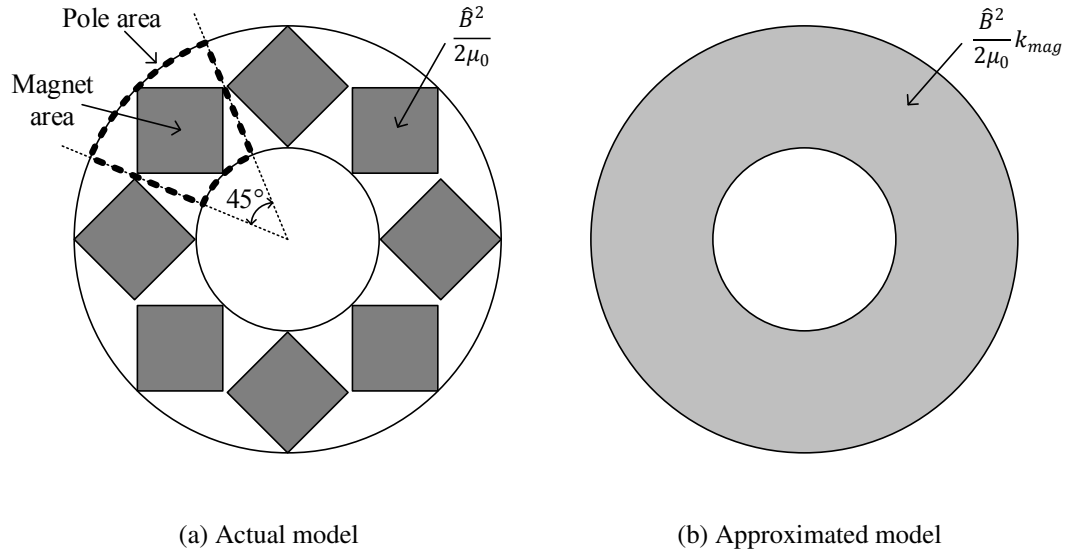


Figure 3.12: Approximation of Maxwell stress on rotor discs for deflection analysis

in diagonal shape, and actual stress on the rotor discs has a trapezoidal shape with eight poles, which is the same as the number of poles. Therefore, an approximation is needed to be able to use circular plate theory.

As proposed in [50], trapezoidal shaped Maxwell stress distribution on the rotor cores is approximated as constant and uniform stress distribution as shown in Fig. 3.12. In order to achieve this, the Maxwell stress is modified by scaling with a magnet constant defined as follows

$$k_{mag} = \frac{\text{magnet area}}{\text{pole area}} \quad (3.54)$$

where the magnet and pole areas are shown in Fig. 3.12a.

Then, constant and uniformly distributed Maxwell stress value used in deflection analysis can be calculated as follows

$$q = \frac{\hat{B}_1^2}{2\mu_0} k_{mag} \quad (3.55)$$

where μ_0 is the permeability of free space, and \hat{B}_1 is the peak value of the flux density of the fundamental component.

In order to measure the accuracy of the analytical deflection model, a dummy machine is selected for the analysis. It is the prototype machine that will be presented in

Table 3.4: Parameters of the selected machine for the deflection analysis

| Parameter | Value |
|-------------------------------|-----------------------|
| Peak fundamental flux density | 0.87 T |
| Rotor outer radius | 150 mm |
| Shaft outer radius | 11 mm |
| Magnet inner radius | 63 mm |
| Air gap clearance | 2.3 mm |
| Rotor yoke thickness | 20 mm |
| Magnet dimensions | 60 mm × 60 mm × 12 mm |
| Pole number | 8 |

Chapter 4, and the deflection for this dummy machine is obtained analytically and using finite element analysis. The parameters of the selected machine are given in Table 3.4.

According to (3.54), the magnet constant of the selected machine is calculated as 0.52. Then, the Maxwell stress for the approximated model is

$$q = \frac{0.87^2}{2\mu_0} 0.52 = 156 \text{ kPa} \quad (3.56)$$

As given in Table 3.4 for the selected machine, the outer radius, a_r , is 150 mm, the shaft radius, b_r , is 11 mm, the inner radius of the area occupied by the permanent magnets, r_o , is 63 mm, and the rotor disc thickness in the axial direction, t_c , is 20 mm. Then, using (3.50) to (3.53), the maximum displacement into air gap is calculated as

$$y = 40.4 \mu\text{m} \quad (3.57)$$

The selected machine has 2.3 mm of air gap clearance. The maximum displacement into the air gap equals to the 1.8 % of the air gap clearance. This much of deflection is within the safe limits of 10 % of the air gap clearance, defined by [23, 50].

In order to measure the accuracy of the analytical deflection analysis, the same model is solved using the finite element method. In the analysis, the simulation toolbox of the SolidWorks software is used. The simulation files as well as the analytical

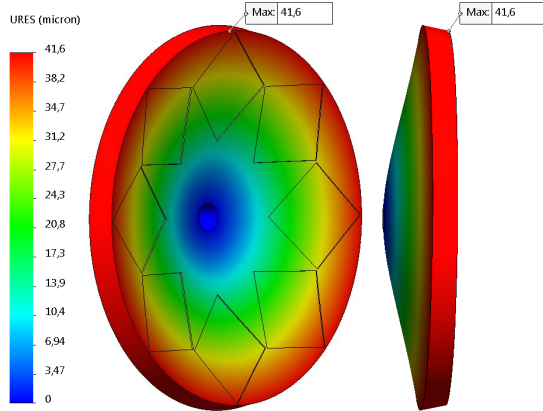


Figure 3.13: Deflection analysis of rotor disc by finite element method

model can be found in Appendix C. The process starts with the mechanical drawing of the part. Then, the fixed surfaces are defined, and the loads applied on the part are introduced. In the analysis, the actual model with diagonal stress distribution shown in Fig. 3.12a is used, rather than the approximated model in Fig. 3.12b.

The result of the finite element analysis by SolidWorks is shared in Fig. 3.13. As expected, since the inner radius of the rotor disc is fixed to the shaft, minimum deflection is observed in this region. The maximum displacement is observed at the outer radius of the rotor disc, and it equals to $41.6 \mu\text{m}$. This value is quite close to the analytical calculation of $40.4 \mu\text{m}$, with 3 % difference. This result proves the accuracy of the analytical deflection analysis and validity of the constant and uniform Maxwell stress distribution approximation, shown in Fig. 3.12.

There is a final point to be considered in the deflection analysis of the rotor disc. At the inner side of the rotor disc, there are four 6 mm screw holes, four 8 mm screw holes, and four 25 mm holes. The screw holes are used to mechanically connect rotor discs to the shaft and the rotor disc located across the air gap. The 25 mm holes are used for the better cooling performance of the machine. These holes will indeed affect the maximum displacement of rotor discs, and the finite element solution is needed for the rotor discs with holes.

Again, the finite element solution is obtained for the rotor disc with holes on it, as seen in Fig. 3.14. The results show that there is $53.6 \mu\text{m}$ displacement into the air

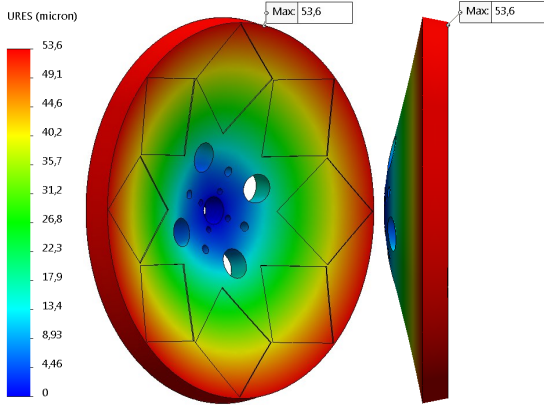


Figure 3.14: Deflection analysis of the detailed rotor disc

gap at the outer radius, and this corresponds to 2.3 % of the air gap clearance. In conclusion, the deflection analysis by analytical and finite element methods shows that the maximum displacement into the air gap due to Maxwell stress does not cause any mechanical problems, and the accuracy of the deflection model is ensured.

3.5 Summary

This chapter presented the analytical modeling of the proposed axial flux permanent magnet machine. The analytical modeling started with magnetic field modeling. Armature reaction is ignored due to the air-cored structure, and the only no-load magnetic field is considered. For the analysis, diagonally placed permanent magnets are approximated as sector shaped permanent magnets. Magnetic scalar potential is used for field derivation with the help of Fourier analysis and Laplace equations. The analysis started with Fourier representation of the magnetization of the permanent magnets. Then, using magnetic scalar potential and constitutive relations, magnetic flux density, and field intensity in the air gap with some unknown coefficients are derived. In order to obtain the field solution, boundary conditions are also considered. In the end, fully analytical representation of the magnetic field is obtained. The accuracy of the analytical model is measured with finite element analysis results for the selected machine. Less than 3 % difference is observed, and the analytical model accuracy is ensured. As a next step, the induced voltage and torque of the proposed machine are

derived using the field model. Also, analytical modeling of the DC winding losses and eddy current losses on the flat windings due to external PM field are presented. Again, finite element analysis is used for verification of loss models, and less than 6 % difference for eddy current loss model is obtained, which is mainly caused by a small difference in the field model. Also, less than 0.5 % difference is observed for the DC winding loss model. Lastly, in the chapter, an analytical model for the deflection of the rotor cores is presented. This analysis is particularly important in the mechanical design of the proposed machine. It is essential to ensure that the deflection into the air gap is within the safe limits. The presented analytical model and finite element results showed good agreement with less than 3 % difference. The presented analytical model is used for the optimization of the machine in the following chapters.

CHAPTER 4

EXPERIMENTAL VERIFICATION OF THE TOPOLOGY WITH 1.4 KW PROTOTYPE

In the previous chapters, an axial flux permanent magnet machine with novel flat winding is presented. To verify the accuracy of the analytical model and prove that the topology can provide the promised advantages, experimental verification is needed.

In line with this need, this chapter presents a manufactured prototype of the proposed machine and experimental results. First, the prototype machine's specifications are determined, and an optimization study is conducted using genetic algorithm to optimize the machine. Then, the mechanical design is presented. Next, the designed machine is manufactured starting from the manufacturing of flat winding stator and rotor discs. The followed experimental results show that the analytical model is quite accurate, and the results are in good agreement. The advantages of aluminum flat winding compared to copper flat winding are presented in the following subsection with experimental results. Lastly, the demagnetization analysis is conducted for the prototype machine, which is a critical issue for permanent magnet machines.

4.1 Optimization Using Genetic Algorithm

This section presents the optimization of the prototype machine. Optimization is an essential step in the machine design process. The machines with high torque and power density can be achieved with the help of optimization. The study is carried out with the developed fully analytical model without finite element analysis (FEA) dependency. Therefore, the optimum design can be achieved quickly. The genetic algorithm optimization files can be found in Appendix C as MATLAB files.

Table 4.1: Optimization constraints

| Parameter | Value |
|------------------------|---------------------|
| Line voltage | 48 V |
| Current density | 4 A/mm ² |
| Pole number | 8 |
| Remanence flux density | 1.39 T |
| Air gap clearance | 2.3 mm |
| Flat wire thickness | 1 mm |
| Efficiency | $\geq 80\%$ |
| Electrical frequency | ≤ 100 Hz |

The optimization process starts by determining the equality and inequality constraints of the optimization, which is given in Table 4.1. These constraints define the specifications and limits of the target design. The study aims to design an eight-pole machine with a line voltage of 48 V. Also, the current density on the conductors is set to 4 A/mm². The prototype is naturally cooled, and it has been confirmed experimentally that the flat winding stator is thermally safe with this current density, which will be presented in Section 4.4 in this chapter.

In the design, N42M grade NdFeB magnets, which have remanence flux density of 1.39 T, are used due to their high energy product. The manufacturing tolerances of the manufactured prototype are kept high to make the manufacturing easier. In that context, the air gap clearance is set to 2.3 mm. Additionally, in order to limit the eddy current losses on the windings due to external PM field because of the large cross-sectional area, the thickness of the flat wire is set to 1 mm. The flat wire can be manufactured from a conductor sheet of various materials such as copper or aluminum. An aluminum and a copper stator are manufactured and compared.

There are two optimization parameters: outer diameter and average air gap flux density. Their minimum and maximum limits are given in Table 4.2. Other dimensions and design parameters such as current rating, rated power, or losses are calculated using optimization constraints in Table 4.1 and optimization parameters in Table 4.2.

Table 4.2: Optimization parameters

| Parameter | Minimum value | Maximum value |
|----------------------|----------------------|----------------------|
| Outer diameter | 100 mm | 600 mm |
| Air gap flux density | 0.1 T | 1 T |

The objective function of the optimization can be defined in various ways depending on the application and design goals. For example, in [52], the authors used an FEA-based differential evaluation optimization algorithm for the optimization of interior permanent magnet (IPM) motors with the objective function of volumetric torque density. In another study, the objective function is total harmonic distortion (THD) of back electromotive force (back EMF) in an FEA-based IPM motor optimization using particle swarm optimization algorithm [53]. Multi-objective optimizations are also possible, where the optimization aims to optimize multiple objective functions simultaneously. A nice summary of the optimization methods and their objectives for the optimization of electrical machines studied in the literature can be seen in [54, 55].

In this study, the objective of the optimization algorithm is set to minimize the active mass of the machine. That is, the algorithm seeks the most lightweight design that satisfies the design constraints in Table 4.1. The population size and the maximum number of generations are set to 50 for both. Additionally, the elite count and the crossover fraction are set to 3 and 0.8, respectively. As stopping criteria, the maximum number of generations and the average change in the fitness functions are considered.

There are many ready to use genetic algorithm tools. In this study, the genetic algorithm tool of MATLAB is used. It is easy to use and can be integrated with any optimization problem easily.

With analytical model in Chapter 3, the optimization algorithm is run on MATLAB in order to minimize the active mass. At the end of the optimization process, genetic algorithm converged to the optimum design with an active mass of 29 kg. Optimization parameters, outer diameter and air gap flux density are determined as 300 mm and 0.6 T, respectively. The overall parameters of optimal design are shown in Table 4.3.

Table 4.3: The optimum design parameters of the 1.4 kW prototype

| Parameter | Value |
|---|-----------------------|
| Rated power | 1.4 kW |
| Line rms voltage | 48 V |
| Line rms current | 20 A |
| Rotational speed | 525 rpm |
| Rated torque | 26 Nm |
| Pole number | 8 |
| Frequency | 35 Hz |
| Axial length | 77 mm |
| Outer diameter | 300 mm |
| Efficiency | 89 % |
| Active mass | 29 kg |
| Structural material mass | 16 kg |
| Torque density | 0.90 Nm/kg |
| Air gap flux density | 0.6 T |
| DC winding losses | 110 W |
| Eddy current losses on windings due to external PM field | 53 W |
| Phase resistance | 93 mΩ |
| Phase inductance | 90 μH |
| Stator winding factor | 0.9891 |
| Rotor core thickness | 20 mm |
| Number of turns per phase | 20 |
| Flat wire dimensions | 1 mm × 5 mm |
| PM dimensions | 60 mm × 60 mm × 12 mm |

At the end of optimization, 1.4 kW, 525 rpm, 20 A and 48 V axial flux machine with flat windings is obtained. According to both experimental and 3D FEA results, by keeping the frequency low and using thin flat wires, eddy current losses on the windings due to external PM field are kept small. In fact, eddy current losses are less than

the DC winding losses resulted from phase currents. The optimum design has active mass of 29 kg, mainly dominated by the mass of the double sided rotor discs with the thickness of 20 mm.

The optimum design employs 240 flat wires. Since it is a three phase machine, there are 80 flat wires per phase. It is investigated in Fig. 2.11 that four flat wires form a turn in flat winding topology for the eight-pole machine. Therefore, there are 20 turns per phase in the optimum design. This low number of turns results in a low line voltage of 48 V. However, due to the large cross-sectional area of the flat wires, a high current rating of 20 A is achieved per phase. In the end, 89 % efficient, low voltage, the high current machine is achieved.

The torque density of the optimum design is 0.90 Nm/kg. This value is slightly lower than other studies in the literature such as 4 kW axial flux machine with torque density of 1.67 Nm/kg in [56] or 2.1 kW axial flux machine with torque density of 1.87 Nm/kg in [57]. The reason for this is that in this study, the aim is to emphasize the advantages of flat winding structure and verify the proposed analytical model; the aim is not to have a compatible machine with high torque or power density. In that context, manufacturing tolerances are kept high to make manufacturing easier. For example, the air gap clearance is 2.3 mm in the design, which is quite large for this diameter and power ratings, resulting in low torque density.

Then, the optimum design is simulated on ANSYS Maxwell for finite element analysis (FEA). First, magnetic flux density distribution is plotted on the midplane at the air gap, as in Fig. 4.1. Additionally, in Fig. 4.2, the axial component of flux density at mean radius is plotted using analytical method and 3D FEA for the optimum design.

Lastly, under the rated operation of 20 A and 525 rpm, the output torque of the machine is plotted using FEA in Fig. 4.3, while the machine is running as motor and driven by sinusoidal three phase currents. For the FEA analysis, 3D mesh structure shown in Fig. 4.4 is used. It is seen that the average value of the torque is calculated as 25.8 Nm, which is very close to the rated torque value of the optimum design, 26 Nm, obtained from the developed analytical model. The torque ripple is measured as 0.9 Nm, which is 3 % of the mean value. This torque ripple is caused by the harmonics in the back EMF, which is resulted from the harmonics in the air gap flux

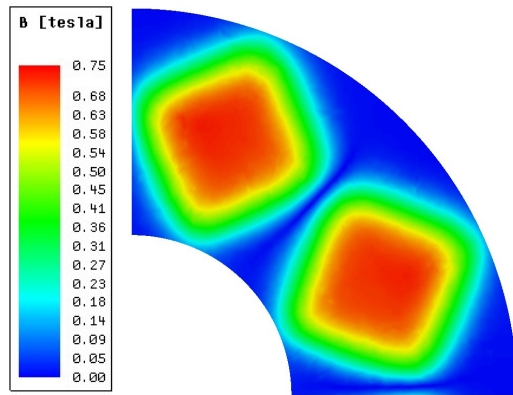
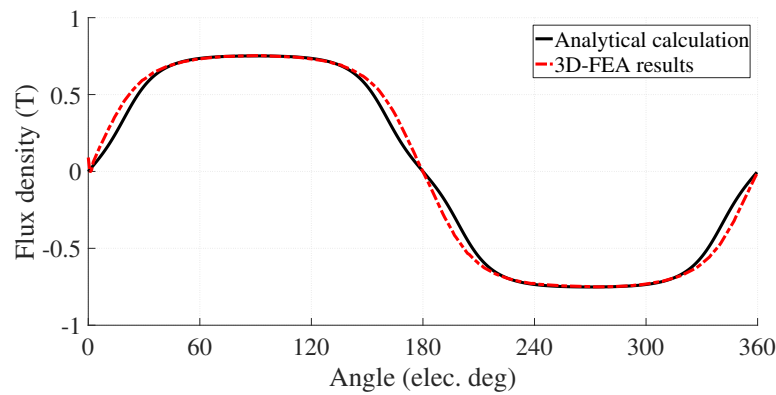
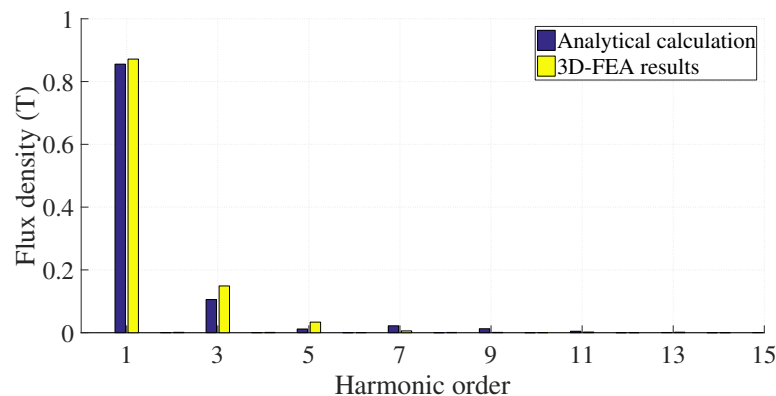


Figure 4.1: Air gap flux density distribution of the optimum design obtained using 3D FEA



(a) Spatial distribution



(b) Harmonic distribution

Figure 4.2: Air gap flux density of the optimum design

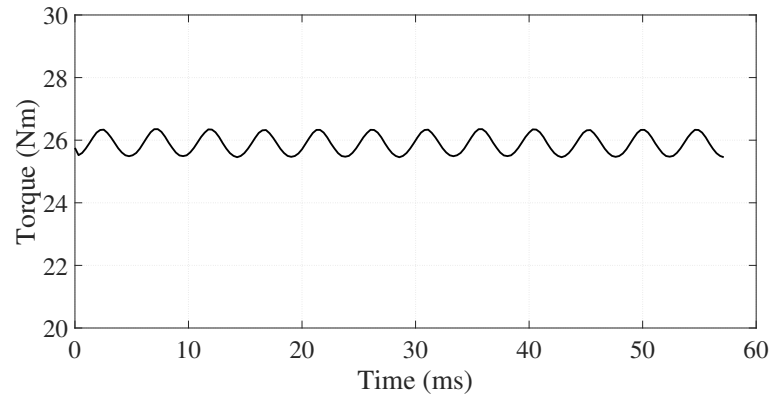


Figure 4.3: Output torque of the optimum design with sinusoidal excitation obtained by 3D FEA

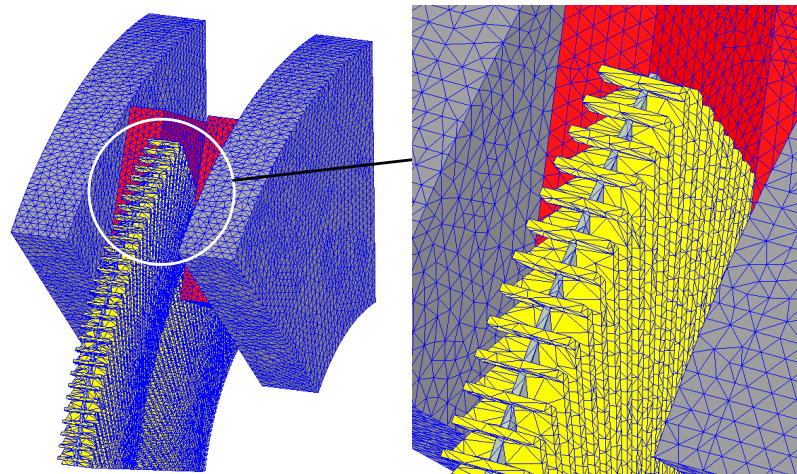


Figure 4.4: 3D mesh structure used in finite element analysis

density seen in Fig. 4.2. Since the input current is pure sinusoidal, and the back EMF of the machine has harmonics, the torque ripple is observed. At experimental results, this value is expected to be smaller due to the inertia of the rotor.

The electromagnetic model of the prototype machine for the finite element analysis can be found in Appendix C as ANSYS Maxwell file.

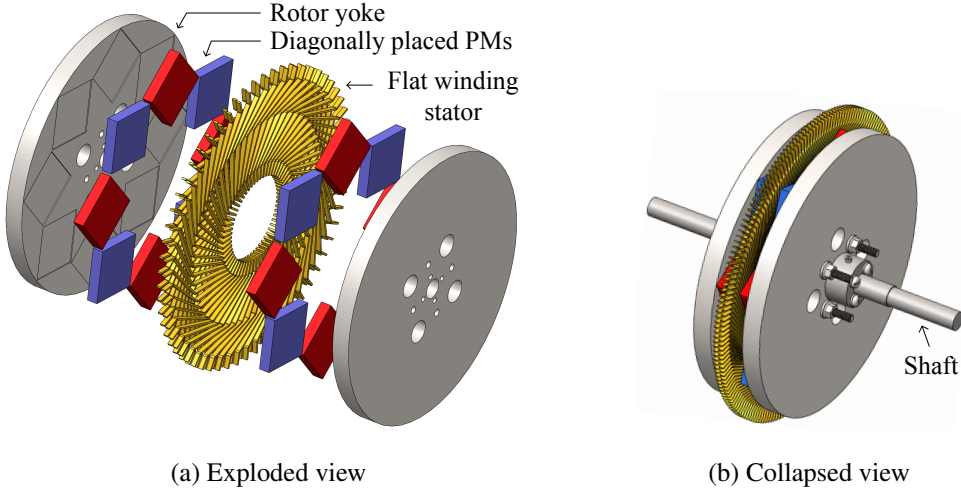
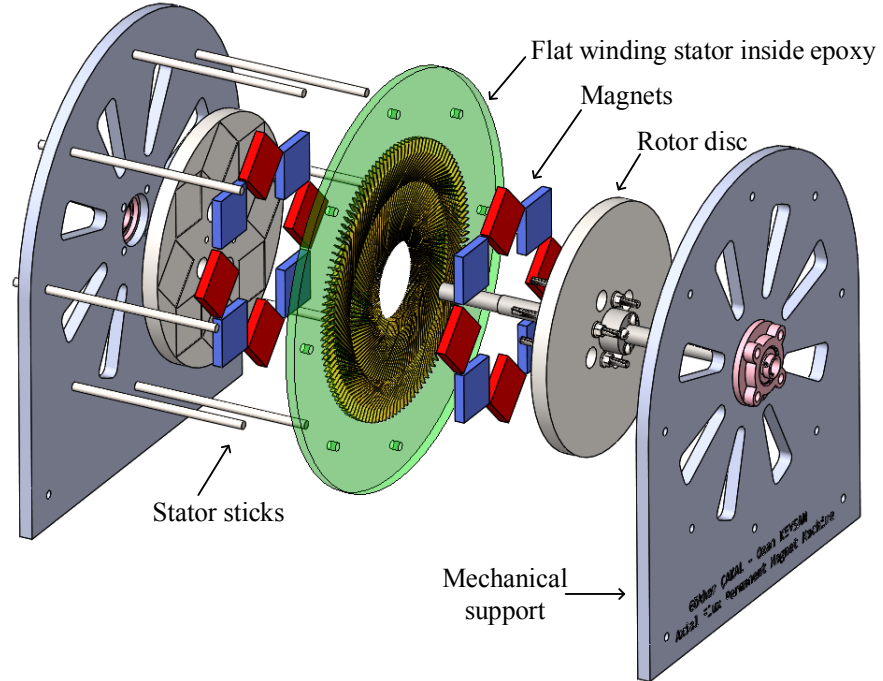


Figure 4.5: Mechanical drawing of the optimum design on SolidWorks

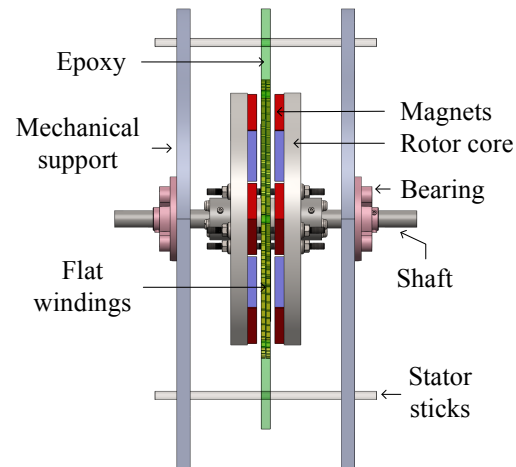
4.2 Mechanical Design

The mechanical model of the optimum design is created on SolidWorks environment before moving into the manufacturing stage. In Fig. 4.5, the optimum design is shown with its exploded and collapsed views. In the model, two rotor discs, having eight poles each, are connected via the shaft. The synchronous rotation of two rotor discs is ensured with rigid connection to the shaft. Also, there are four sticks connecting two rotor discs together with rigid connection. The outer diameter of the rotor is 300 mm, whereas the air-cored stator has a slightly larger diameter due to end winding connectors. The air-cored stator, having 240 flat wires, is sandwiched between two rotor discs. The mechanical model of the prototype machine can be found in Appendix C as SolidWorks files.

In Fig. 4.6, the mechanical assembly of the optimum design with structural elements is shown with exploded and collapsed views. The outer frame of the machine consists of two mechanical supports fixed to the ground. The mechanical support is made of compact laminate material. There are some holes on the mechanical support, which aim to decrease the structural mass of the proposed topology. In order to fix the stator with respect to the stationary outer frame, first, the stator windings are put inside the epoxy. Then, stator sticks are used to connect the stator to the outer frame of the



(a) Exploded view



(b) Collapsed side view

Figure 4.6: Mechanical assembly of the optimum design

machine. The rotor structure having two rotor discs are connected to the outer frame via shaft and bearings. Two bearings are used to make the shaft and outer frame connection.



Figure 4.7: Manufacturing of flat wires with laser cutter

4.3 Manufacturing of the Prototype Machine

The optimum design, whose overall parameters are given in Table 4.3, is manufactured for the experimental verification. The manufacturing stages start with the manufacturing of flat wires. For the optimum design, the flat wires are manufactured from 1 mm thick copper sheet using a fiber laser cutter. In Fig. 4.7, a photo taken during the manufacturing of flat wire is shown. As an alternative, a water jet can be used for cutting copper sheet; however, the manufacturing cost increases with this method compared to laser cutting. Stamping press or punch machines can be preferred for economical manufacturing solutions.

In Fig. 4.8, a manufactured flat wire is shown with its final and preformed shape before the bending stage. In order to give its final form, U-shaped flat wire should be bent at several points. The bending angles and flat wire length depend on the pole number and machine geometry.

In the optimum design, there are 240 flat wires. After the manufacturing of this much flat wires, the air-cored stator can be formed. In order to achieve this, all flat wires are lined up next to each other around an axis, as shown in Fig. 4.9a. Electrical isolation between neighboring flat wires has to be ensured. For this purpose, isolation papers are placed between neighboring flat wires. Additionally, the top and bottom sides of flat wires also should be isolated electrically. To achieve this, a disc-shaped isolation

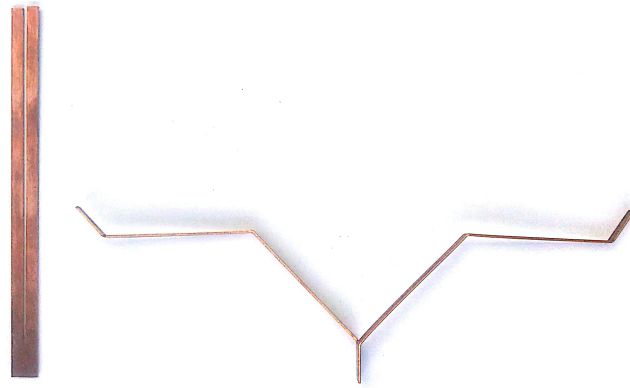


Figure 4.8: Manufactured copper flat wire

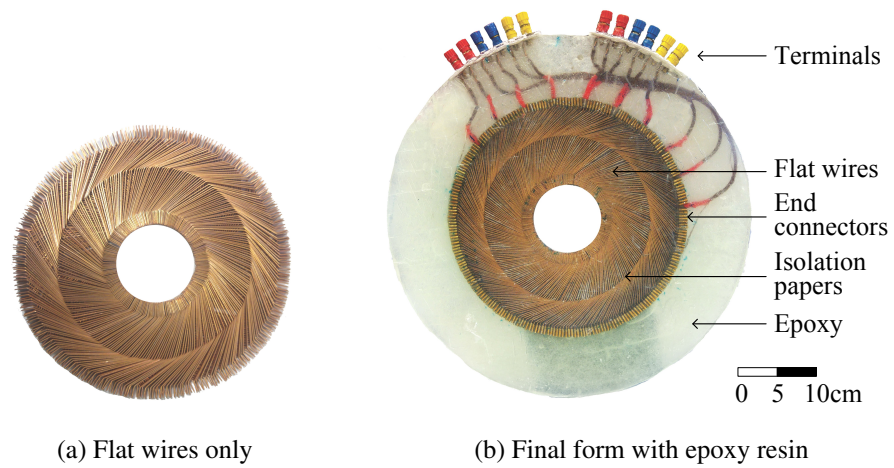


Figure 4.9: Manufacturing of flat winding stator

paper is located in the middle of flat wires. At this point, it is important to note that the isolation paper should be able to withstand high temperatures. The temperature of the windings may go up to 100 °C.

As a next step, end winding connections are made. In order to achieve this, first, the end points of two flat wires are connected mechanically with a connector. Then, soldering is done for a strong mechanical and electrical connection. This is a critical step in the manufacturing of flat winding stator because weak soldering may lead to weak electrical connection and high resistance. In the end, hot points may be observed in the stator. As an example of this fault, in Fig. 4.10, an end winding connection with weak soldering is shown. In the picture of this manufactured stator,

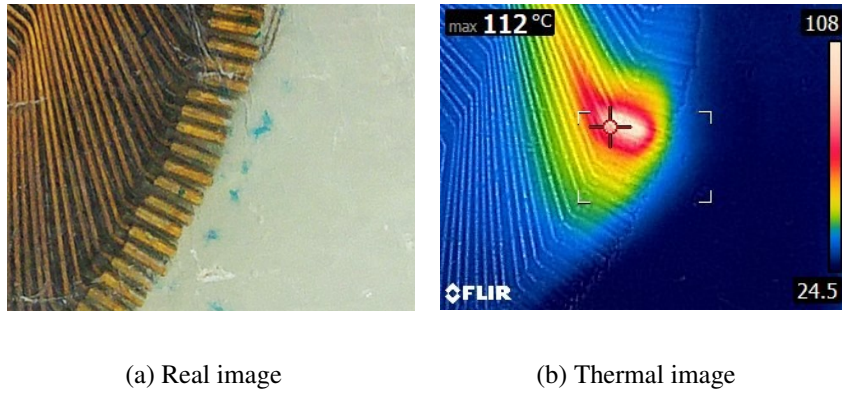


Figure 4.10: A hot spot at the improper end winding connection due to weak soldering

weak soldering resulted in high electrical resistance, which ends up with a hot spot under load condition. Therefore, it is essential to have a robust electrical connection with proper soldering at the end windings.

In order to measure the temperature of windings, two PT100 thermocouples are placed among flat wires. Next, in order to have mechanical rigidity, the flat wires are mold inside the epoxy. In Fig. 4.11, a photo taken during the molding process is shown. The selection of epoxy resin should be carefully made. It should have high thermal conductivity to evacuate the heat out of stator windings. Additionally, the viscosity of the epoxy resin should be low enough so that it can penetrate small areas between flat wires easily during the molding stage. As the last step in the manufacturing of three phase air-cored flat winding stator, the terminal connections should be provided with terminal connectors. The final form of the manufactured stator is shown in Fig. 4.9b.

In this prototype, three phase machine configuration is studied, in which the phases are separated by 120° electrical phase difference. In order to increase the winding factor of the three phase stator, instead of three phase configuration with a phase difference of 120° , six phase configuration with a phase difference of 60° is preferred as shown in the phasor diagram in Fig. 4.12. Then, phases shown with the dashed line in the phasor diagram are connected in reverse polarity to the opposite phase in series, and three phase stator configuration with phase difference of 120° is achieved. This adjustment provided a 3.5% increase in the winding factor and rated voltage.



Figure 4.11: Epoxy molding of flat winding

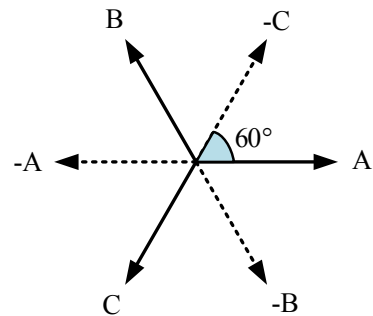


Figure 4.12: Phasor diagram of the three phase stator

The manufacturing of the optimum design continued with the manufacturing of rotor discs, having eight poles each. N42M grade NdFeB magnets are used in manufacturing. They have dimensions of $60\text{ mm} \times 60\text{ mm} \times 12\text{ mm}$. The rotor core is manufactured from ST52 steel material. The holes on the rotor core are drilled with the CNC machine. Then, to give the final form of the rotor, square-shaped magnets are glued on the rotor disc in a diagonal structure. The final form of the rotor disc with permanent magnets on it is shown in Fig. 4.13

After the manufacturing of flat winding stator and rotor discs, they are assembled to give the final form of the manufactured machine, as shown in Fig. 4.14. Two rotor discs are connected to each other via the shaft. The air-cored stator is fixed to the outer frame via stator sticks. The stator sticks are also used to adjust and maintain the mechanical clearance between the stator and rotor discs. Two bearings are used



Figure 4.13: Manufactured rotor disc employing diagonally placed permanent magnets

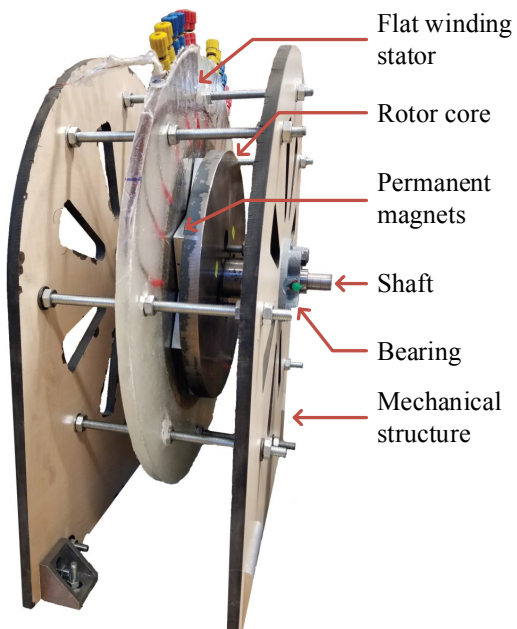


Figure 4.14: Manufactured prototype machine

to connect the rotating shaft and the fixed outer frame. At this point, it is important to note that there is no forced cooling on the system, and the stator windings are naturally cooled. With forced cooling, more electrical loading and higher torque density can be achieved. However, since the scope of this study is to prove the concept and highlight the advantages of flat winding rather than manufacturing a compatible machine, natural cooling is preferred. As a next step in the study, experimental verification is followed.

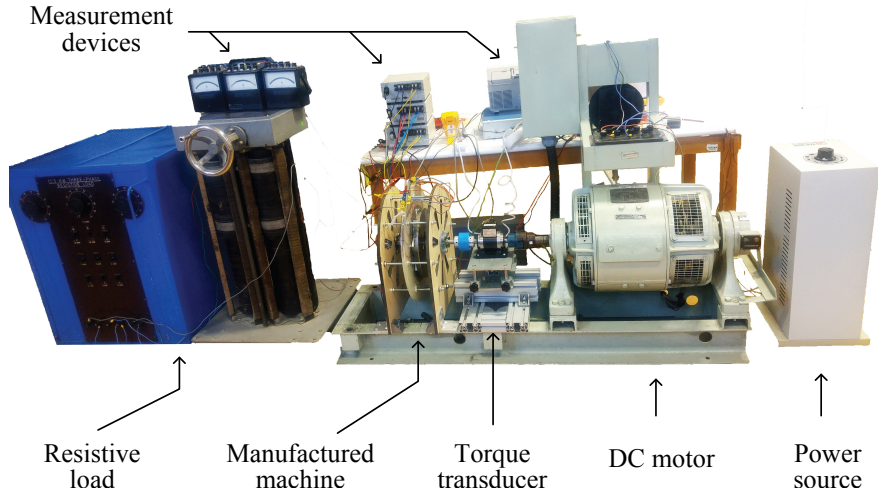
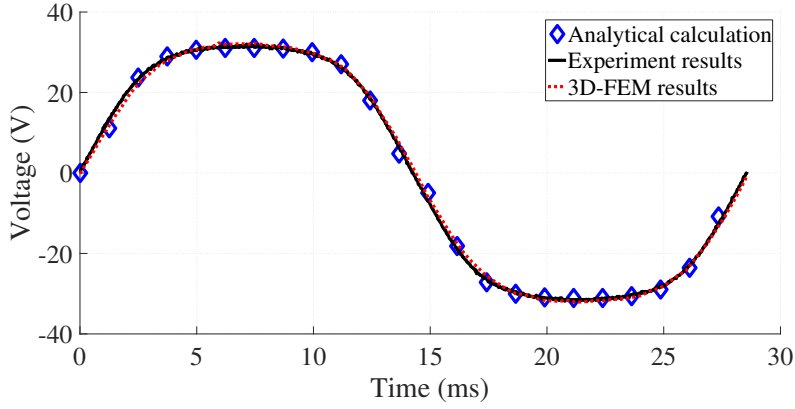


Figure 4.15: Experimental setup

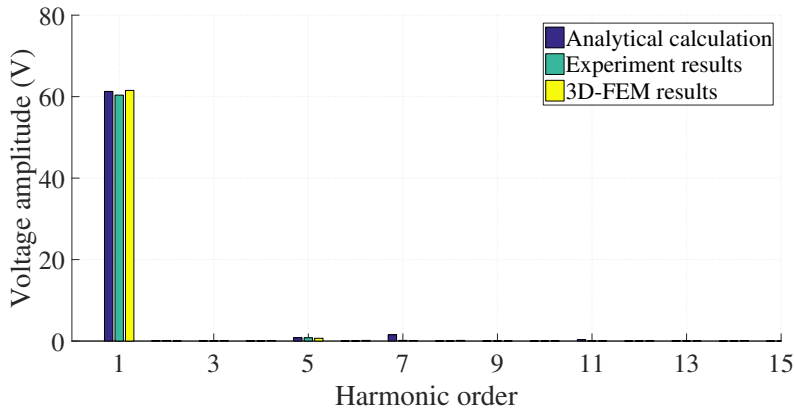
4.4 Experimental Results

Experiments are conducted with the setup shown in Fig. 4.15. During the tests, the manufactured machine is run as a generator. It is driven by a DC motor mechanically coupled to it. Between these two machines, a torque transducer is placed for torque and speed measurements. Since the manufactured machine is run as a generator, the input power is mechanical, and this torque transducer measures it. In order to load the prototype machine, three phase resistor bank is used. The output power is electrical, and it is measured by three phase wattmeter. Lastly, the temperature of the flat windings is measured with PT100 thermocouples.

The first test conducted on the manufactured machine is the open circuit induced voltage test. In order to obtain open circuit characteristics, at no-load, the prototype machine is rotated at the rated speed of 525 rpm by DC motor. The induced voltage in terminals of the machine is recorded via oscilloscope, and the results are compared with analytical and finite element solutions. In Fig. 4.16a, phase voltages are compared in the time domain, and in Fig. 4.16b, the harmonic content of line-to-line voltage is compared. Due to wye-connection, third-order harmonics are eliminated for the line-to-line voltage. Less than 2 % difference is observed between analytical, experimental, and finite element results. These results validate the proposed analytical model and material properties.



(a) Phase voltage in time domain



(b) Harmonic order distribution of line voltage

Figure 4.16: Open circuit characteristics of the prototype machine

Secondly, at rated speed operation, voltage and current measurements of the prototype machine under full-load and half-load conditions are given in Fig. 4.17. At full-load operation, the phase voltage is decreased by 4.6 % compared to the half-load condition due to voltage drop on the armature resistance. Also, there are harmonics in the current waveform, thought to be caused by the unbalance at the load.

Then, the thermal characteristic of the manufactured prototype is investigated. For this purpose, the prototype machine, working as a generator, is loaded with three phase resistive load at full-load and half-load at the rated speed of 525 rpm. Then, the temperature of the stator windings is recorded every three minutes. The temperature of other machine parts, such as rotors or bearings, is also observed via thermal camera. However, the temperature change of these parts was relatively low compared to

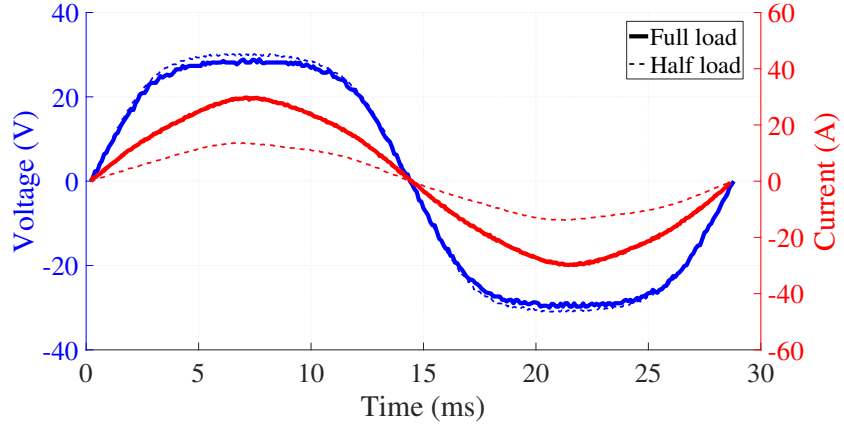


Figure 4.17: Phase voltage and line current measurements of the prototype machine at full-load and half-load conditions

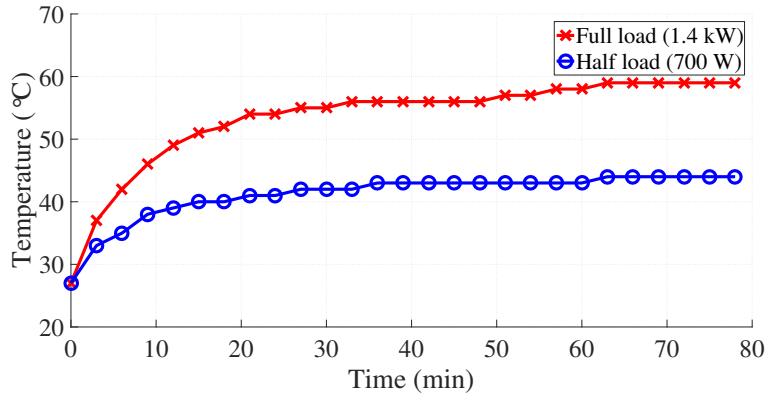


Figure 4.18: Thermal characteristics of the stator windings

the temperature change of stator windings, as expected. The test is conducted under the ambient temperature of 27 °C, and at the end of the test, the thermal characteristic shown in Fig. 4.18 is obtained.

The thermal characteristics in Fig. 4.18 show that the maximum temperature increase of the stator windings is 32 °C under full-load operation of 20 A and 1.4 kW. This value of temperature increase is quite normal for an electrical machine. Under these conditions, the current density is 4 A/mm². According to experimental findings, assuming that the temperature increase of 75 °C on stator windings is allowed, the current density on flat wires can be increased up to 7 A/mm². It should be noted that these results are obtained under natural cooling, and the machine is capable of operating at higher current densities if a forced cooling is used.

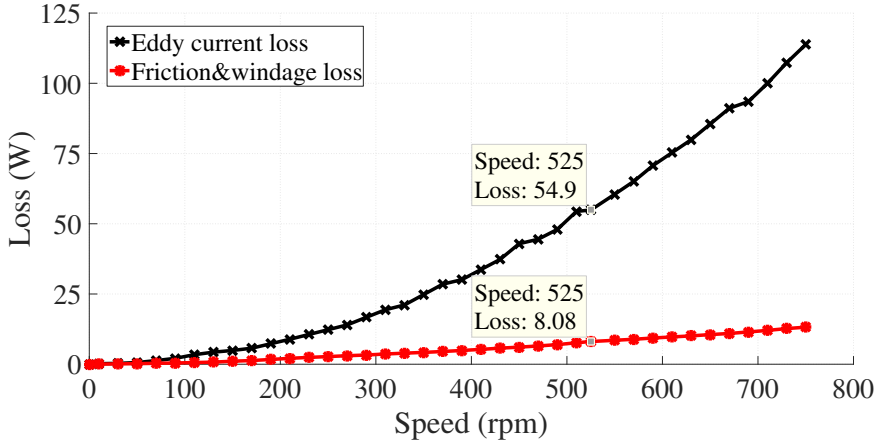


Figure 4.19: The eddy current loss on the windings due to external PM field and friction&windage losses measurement at various rotational speeds at no-load

In order to verify the loss and efficiency calculations, various measurements are taken from the manufactured prototype. First, eddy current losses on the windings due to external PM field are verified. In order to achieve this, first, friction and windage losses characteristics against speed are obtained, as in Fig. 4.19. In order to achieve this, the stator is removed from the machine, and the rotor is rotated at a different speed with the help of the prime mover. The measured power is consumed as friction and windage losses only. Then, the stator is assembled with the rotor, and the machine is rotated at various speeds under no-load condition (i.e., open circuit) in order to eliminate DC winding losses. In that case, there is no output power, and input power is consumed as eddy current loss on the windings due to external PM field, friction, and windage losses. Then, the eddy current characteristic against speed is obtained by taking the difference, shown in Fig. 4.19. It is observed that no-load losses increase exponentially with speed. This result is expected since eddy current losses on the windings due to external PM field and windage losses are proportional to the square of the induced voltage frequency or speed. At the rated speed of 525 rpm, 8 W of friction and windage loss is measured. The eddy current loss on the windings due to external PM field is measured as 55 W as in Fig. 4.19. This value is in good agreement with analytical eddy current calculation of 53 W, with less than 4 % difference. This small difference is mainly caused by less than 2 % difference in analytical field modeling and manufacturing tolerances. The FEA also results in 53 W of eddy current losses on the windings. These three results are close to each other, and in good agreement.

Table 4.4: Loss and efficiency comparison of analytical and experimental results

| | Analytical model | Experimental results |
|---|-------------------------|-----------------------------|
| Eddy current loss on windings due to external PM field | 53 W | 55 W |
| DC winding loss | 110 W | 117 W |
| Phase resistance | 93 mΩ | 100 mΩ |
| Efficiency at full load | 89 % | 88 % |

Additionally, DC winding losses due to phase currents are obtained experimentally using the total loss measurement at the rated operation of 1.4 kW and 20 A at steady-state temperature and rated speed. Total loss is measured as 180 W, which includes DC winding losses, eddy current losses on the windings due to external PM field, friction, and windage losses. Thus, it is concluded that DC winding losses are 117 W, which is in close agreement with the analytical DC winding loss calculation of 110 W. The small difference is mainly caused by the cable resistance of the measurement devices in the experiment setup. Since the current rating of the machine is high (20 A), the losses on the cables of the measurement devices start to make a difference. With loss measurements, the efficiency of the prototype is calculated as 88 %, which is very close to the 89 % efficiency calculation obtained by analytical results. The overall comparison of losses and efficiency is given in Table 4.4. In conclusion, the obtained results are in close agreement with analytical calculations, and the proposed model is verified with experimental data.

4.5 Copper vs. Aluminum Flat Winding

It is uncommon for conventional stranded-wired electric machines to see aluminum windings due to higher electrical resistivity than copper ones. Due to the small cross-sectional area of the wire, DC winding losses dominate the eddy current losses on the windings due to external PM field for these stranded-wired machines. Therefore, aluminum stranded wire usage is not preferred as it increases the machine's losses due to increased DC resistance.

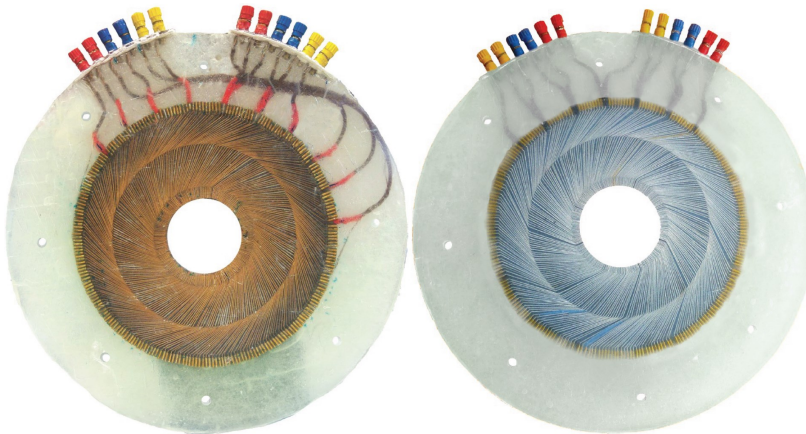


Figure 4.20: Manufactured copper (left) and aluminum flat winding stators for the prototype machine

However, for the wires with a large cross-sectional area, the AC losses start to take place. As analytically modeled in (3.48), it is seen that eddy current losses on the windings due to external PM field decrease when the resistivity of the material increases due to the increased skin depth of the material. Therefore, due to its higher resistivity, aluminum results in lower AC losses than copper, and it may be favorable in terms of total losses and efficiency for some applications. With that motivation, the feasibility of copper and aluminum will be evaluated.

Aluminum and copper material has the following major differences:

- Electrically, copper is 63 % more conductive than aluminum [58].
- For the same volume, aluminum is 70 % lighter compared to copper, which makes aluminum favorable in terms of weight [59].
- From the cost perspective, aluminum is 70 % cheaper per mass compared to copper, providing cost-effective solutions [60].

The feasibility of two alternatives is evaluated both analytically and experimentally. For that purpose, an aluminum flat winding stator for the prototype machine is manufactured, as shown in Fig. 4.20. The aluminum stator has the same dimensions as the copper counterpart.

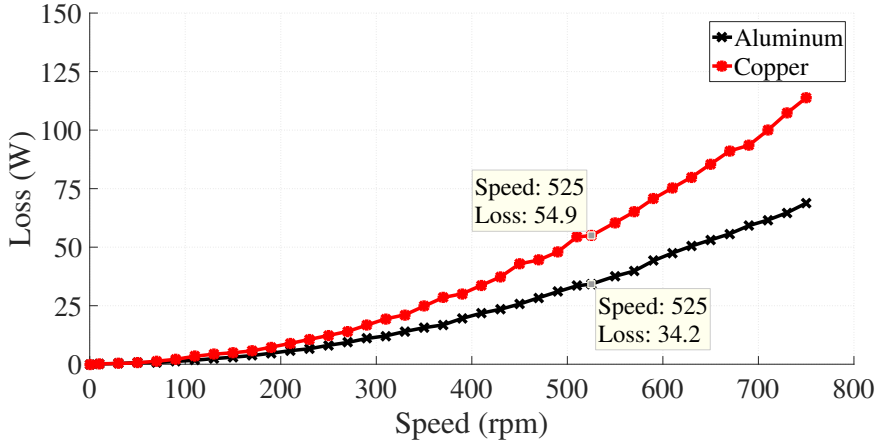


Figure 4.21: Experimental data of eddy current losses on the windings due to external PM field of copper and aluminum stators

The first difference between the two alternatives appears in manufacturing. The aluminum is softer compared to copper and, this makes it easier to process with the required tools. For the end winding connections of copper flat winding, simple soldering is enough to connect two flat wires electrically. However, for the aluminum flat winding, more advanced welding solutions such as tungsten inert gas (TIG), ultrasonic, punch, resistance or laser welding methods need to be employed to connect two flat wires at the end windings. From this perspective, the manufacturing cost of the aluminum stator may be higher depending on the solution applied, even if the material cost is less.

The variation of the eddy current losses on the windings due to external PM field for two stators against speed is obtained experimentally on the prototype machine and plotted in Fig. 4.21. As analytically modeled in (3.48), it is seen that the eddy current losses on the windings due to external PM field are proportional to the square of the electrical frequency or speed. Also, it is observed that copper has higher eddy current losses compared to aluminum at any speed due to its lower resistivity and smaller skin depth. This is expected since in (3.48), it is analytically shown that the eddy current losses increase with decreasing resistivity. However, the higher resistivity of aluminum limits the eddy current flow, resulting in lower losses. Note that at rated speed, eddy current losses of the copper stator due to external PM field is 60 % more than that of aluminum.

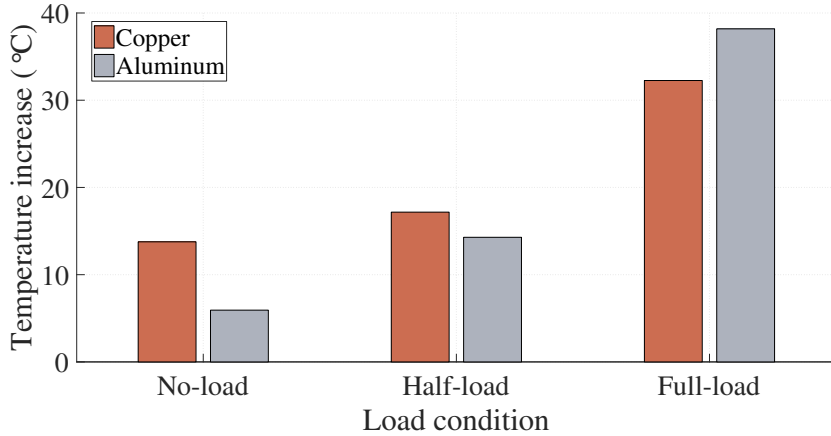
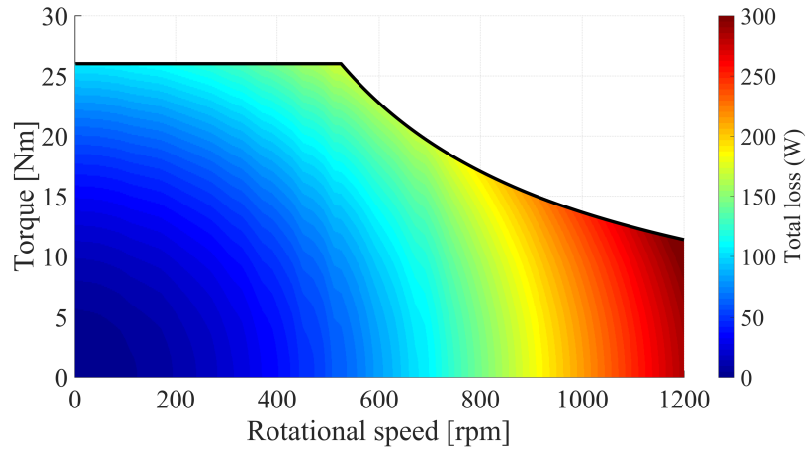


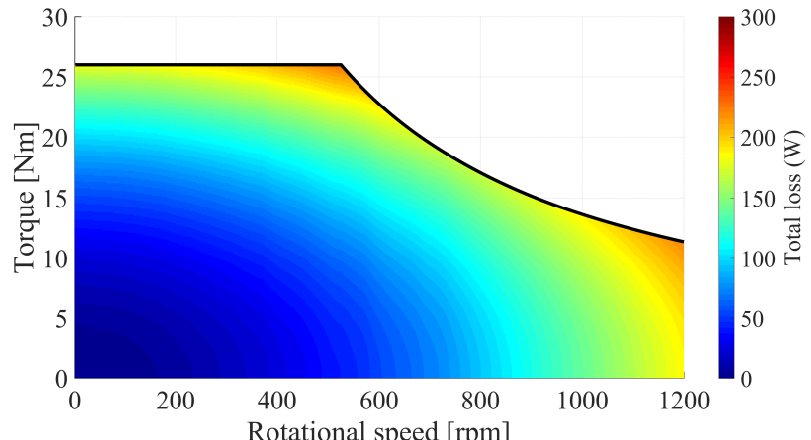
Figure 4.22: Temperature increase of copper and aluminum stators at various loading conditions at rated speed

In order to observe the thermal performance of copper and aluminum stators, the prototype machine is tested under no-load, half-load, and full-load conditions at rated speed, for two stators, separately. After a thermal steady state is reached for each case, the temperature increase of the stator windings is recorded, and the results are shared in Fig. 4.22. It is observed that for no-load and half-load conditions, copper stator reached higher operating temperatures. This is because, at these two operating conditions, eddy current losses on the windings due to external PM field dominate the DC winding losses. Due to its higher electrical resistivity, aluminum suppresses eddy current losses better, and it becomes more favorable in terms of losses and thermal performance. However, for full-load operation, the DC winding losses dominate the eddy current losses due to increased current. Then, due to its lower resistivity, copper limits DC winding losses better, and it becomes more favorable for this operation.

In order to evaluate the performance of both design in details, total loss of the machine at each operating point on the torque-speed plane is plotted in Fig. 4.23, separately the machines with copper and aluminum stators. The losses include both DC winding losses and eddy current losses on the windings due to external PM field. High losses are observed for the copper stator at high speed regions, resulting from high eddy current losses due to low resistivity. For the aluminum stator, high losses are observed equally at both high speed and high torque regions. However, it is seen that the total loss of the copper is higher than total loss of the aluminum at high speed region.



(a) Copper design

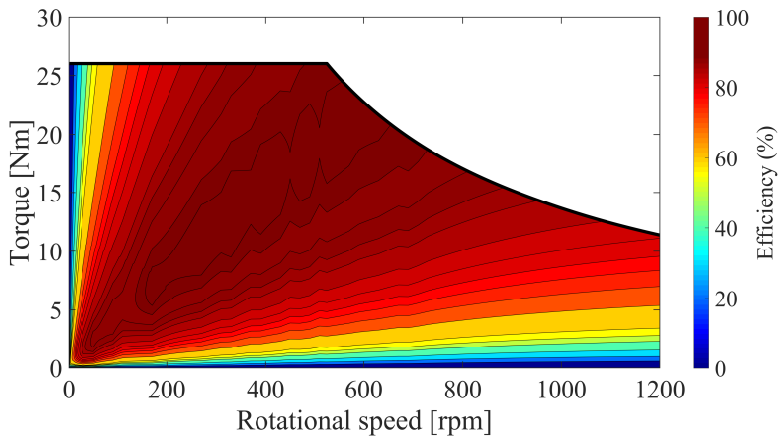


(b) Aluminum design

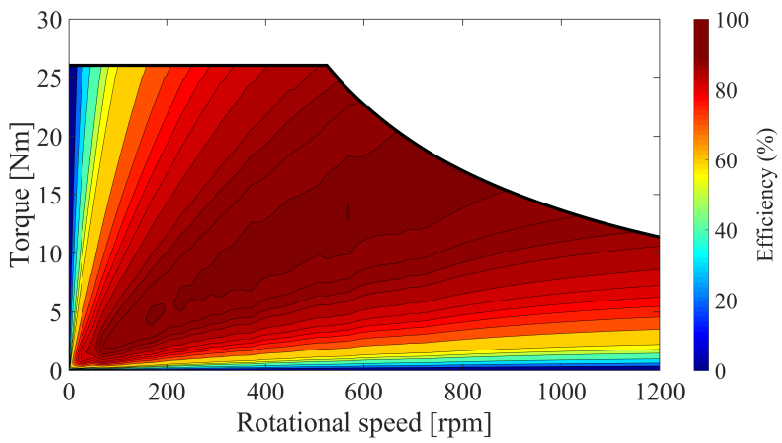
Figure 4.23: Total losses of the machines with different flat winding materials

The efficiency maps of two machines with different stator winding materials are given in Fig. 4.24. From the efficiency maps, it is seen that the most efficient operating points of the copper stator are close to high torque regions, whereas, for the aluminum stator, the most efficient operating points are close to high speed region.

Lastly, derived from these results, the favorable material in terms of losses and efficiency is shown on the torque-speed plane in Fig. 4.25. This analytical finding is also experimentally verified at the crossed operating points by loss comparison of two designs. Note that for the rated operating point of 26 Nm and 525 rpm, the design with a copper stator is more favorable.



(a) Copper design



(b) Aluminum design

Figure 4.24: Efficiency map of the machines with different stator materials

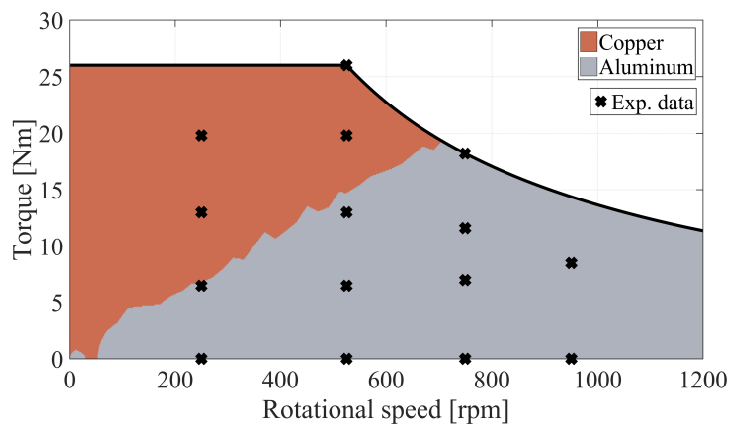


Figure 4.25: Favorable material in terms of losses and efficiency

Table 4.5: Evaluation of the designs with copper and aluminum stators at rated speed (26 Nm, 525 rpm) and high speed (14 Nm, 1000 rpm) operations

| | Copper | | Aluminum | |
|----------------------|-------------|------------|-------------|------------|
| | Rated speed | High speed | Rated speed | High speed |
| DC winding losses | 110 W | 31 W | 185 W | 49 W |
| Eddy current losses* | 53 W | 199 W | 34 W | 124 W |
| Total losses | 171 W | 246 W | 227 W | 189 W |
| Efficiency | 89.3 % | 85.3 % | 86.3 % | 88.3 % |
| Winding mass | 3.56 kg | | 1.08 kg | |
| Material cost | \$170 | | \$12 | |

* Eddy current losses on the windings due to external PM field

As a case study, two designs employing copper and aluminum flat winding stators are compared at two operating points in Table 4.5. For the first operating point, the rated operation of 26 Nm and 525 rpm is selected. At the second operating point, the machine delivers rated power at higher speed operation of 14 Nm and 1000 rpm. The designs are compared in terms of losses, efficiency, flat winding weight, and cost at these two operating conditions. For the total loss and efficiency calculations, DC winding losses, eddy current losses on the windings due to external PM field, friction and windage losses are considered. Note that the two designs have exactly the same geometry for all machine parts. Therefore, these copper and aluminum alternatives can have different machine ratings due to different efficiencies. The aim of this study is to compare the losses for the same geometry for copper and aluminum alternatives.

At 525 rpm, the aluminum design has 33 % more losses than the copper design, mainly due to elevated DC winding losses at high torque. From the weight and cost perspective, the aluminum winding has 30 % weight, and 7 % cost of the copper winding, which could be the reason for the preference for some applications. At 1000 rpm, the aluminum design has 23 % less total losses, as well as weight and cost advantages stated above. Thus, aluminum design is favorable at this operating point in terms of all parameters evaluated.

One can conclude from these results that at high speed region, eddy current losses on the windings due to external PM field dominate, and aluminum is more favorable due to its high resistivity. However, at high torque or current region, copper material is more favorable due to its high conductivity. As a result, during the initial design phase, higher efficiencies can be achieved with copper or aluminum flat windings considering this loss analysis.

4.6 Demagnetization Analysis

Permanent magnets are composed of magnetic dipoles aligned at magnetization direction. A permanent magnet can be partially or fully demagnetized when the alignment of the dipoles are distorted permanently. Demagnetization mainly occurs due to high temperatures, large stator currents resulting in strong armature reaction, or aging of the permanent magnet itself [61].

A typical demagnetization, or B-H, characteristics of a permanent magnet is shown in Fig. 4.26. In the figure, B_r is the remanence flux density, and H_c is coercivity. These parameters depend on the temperature, and the permanent magnet has different B-H characteristics at different temperatures. During normal operation, the permanent magnet works in the reversible region. However, if a large reverse magnetic field is applied, the operation point may go beyond the knee point, and the permanent magnet may be demagnetized permanently. In that case, B-H characteristic is reshaped with recoil line, as in Fig. 4.26. As a result, a demagnetized permanent magnet loses its energy capacity, resulting in decreased output power of the permanent magnet machine.

For the proposed machine, the stator is air-cored, and magnetic reluctance is high. This results in low inductance of the stator windings. Therefore, in a short circuit fault, large short circuit current may flow through phases due to low inductance and impedance. This creates a strong magnetic field in the air gap and may demagnetize the permanent magnets.

On the other hand, the proposed topology has low voltage and high current characteristics due to flat winding topology. Fortunately, this factor limits the short circuit

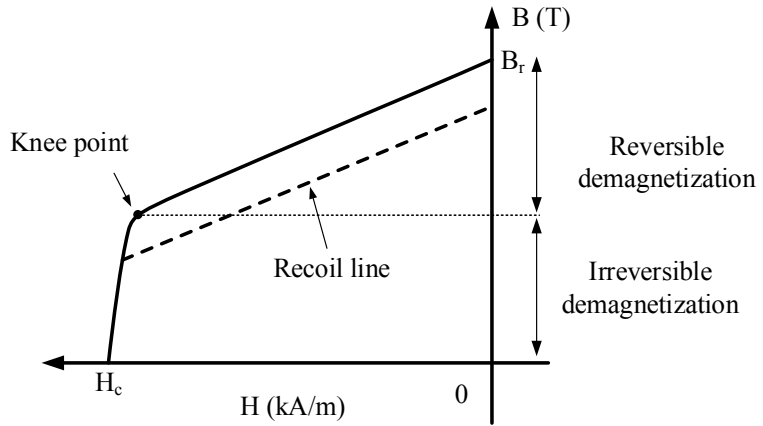


Figure 4.26: Typical BH characteristics of a permanent magnet

current in a fault situation due to low line voltage. Nevertheless, a demagnetization analysis is needed for permanent magnet machines for reliability issues.

The prototype machine is a surface-mounted permanent magnet machine. The direct axis, or d-axis, of the machine, is aligned with the magnetization direction of permanent magnets, as shown in Fig. 4.27a. The quadrature axis, or q-axis, is placed 90° electrically ahead of the d-axis.

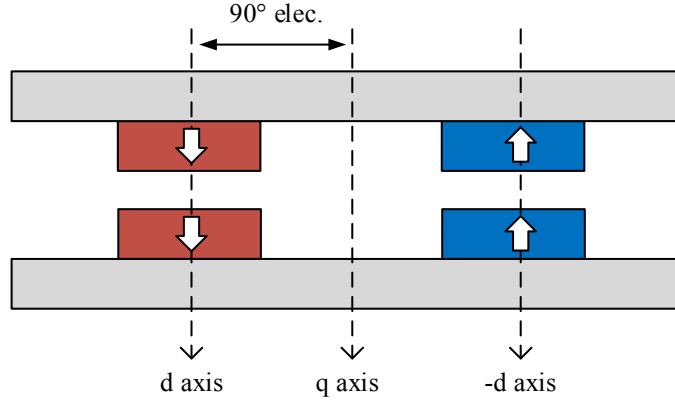
In Fig. 4.27b, the phasor diagram of the direct and quadratures axes are shown. In the figure, \hat{I} is the peak stator current, and θ is the load angle of the machine. In that case, the d-axis current, q-axis current and torque output, T , can be written as

$$I_q = \hat{I} \cos(\theta) \quad (4.1)$$

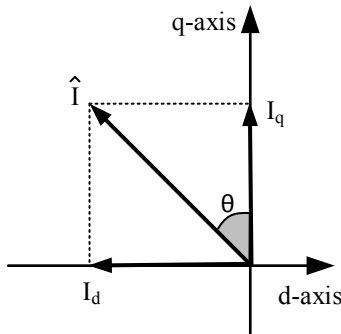
$$I_d = -\hat{I} \sin(\theta) \quad (4.2)$$

$$T = \frac{3}{2} pp \lambda_{PM} I_q \quad (4.3)$$

where pp is the number of pole pairs and λ_{PM} is permanent magnet flux linkage. Note that the torque produced by the machine only depends on q-axis current, and d-axis current does not contribute to the torque production for the surface-mounted permanent magnet machine.



(a) Spatial distribution



(b) Phasor diagram

Figure 4.27: Direct and quadrature axes of the proposed machine

In the field weakening region, beyond the base speed of the machine, $-I_d$ current is applied intentionally so that flux linked by the stator is limited. Referring to Fig. 4.27a, applying $-I_d$ current creates an external magnetic field opposite to the magnetization direction of the permanent magnets. As the magnitude of this reverse magnetic field increases, the permanent magnets face a higher risk of demagnetization.

4.6.1 Demagnetization Current by Finite Element Analysis

The worst-case scenario in demagnetization analysis happens when a large $-I_d$ current is applied with load angle, θ , of 90° , whether in field weakening region or by a control fault. The demagnetization analysis in this study is conducted considering

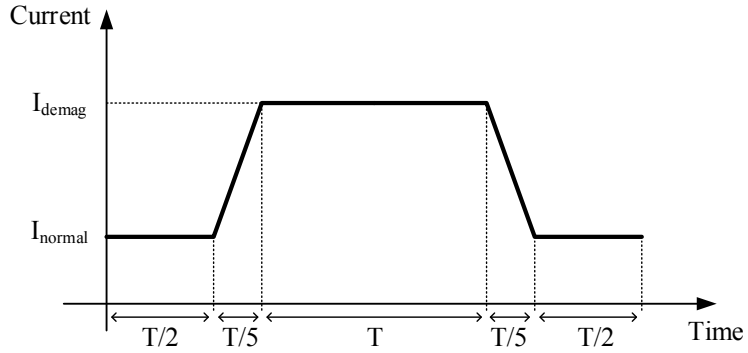


Figure 4.28: Peak current profile applied in demagnetization analysis

this worst-case scenario on ANSYS Maxwell 3D solver. The simulation file for demagnetization analysis can be found in Appendix C. For the analysis, the machine is rotated at rated speed, and the current profile in Fig. 4.28 is applied to the stator windings. Note that since the worst-case scenario is considered, θ is set to 90° , and only $-I_d$ current is applied to the machine. Therefore, the current profile in Fig. 4.28 also represents the $-I_d$ current.

In the current profile in Fig. 4.28, T is the electrical period, I_{normal} is the peak current flowing through stator phases during normal operation in the reversible region, and I_{demag} is peak demagnetization current causing large reverse magnetic field through -direct axis. In order to observe the recoil line on the demagnetization curve, normal current is applied before and after the demagnetization current is applied. For one electrical period, demagnetization current is applied. In the worst case, the demagnetization current, I_{demag} , is observed when two phases of the machine are short circuited at terminals, and large short circuit current flows through short-circuited phases.

In order to check the demagnetization, several observation points are placed inside the permanent magnets in the simulation. On those points, magnetic flux density and field intensity is measured to observe the operation point of the magnet on its demagnetization curve. This study is repeated with different demagnetization currents, I_{demag} , and the results are shown in Fig. 4.29. In the figure, the original demagnetization curve of the magnet at the operation temperature of 80°C is shown with a

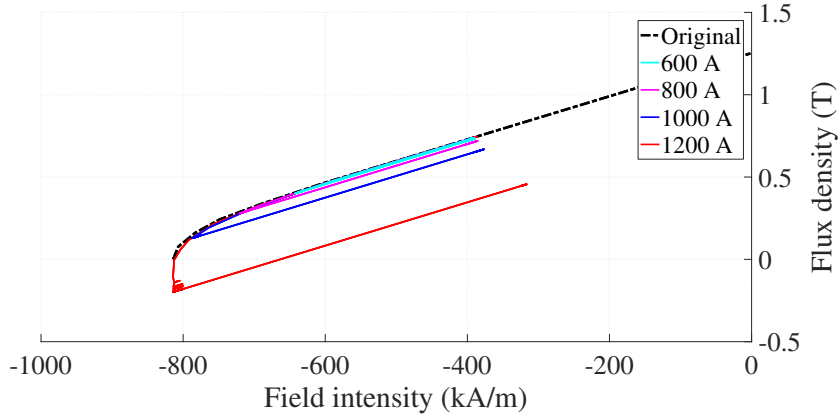


Figure 4.29: Demagnetization characteristic of the permanent magnet at different peak short circuit phase currents at 80 °C

dashed line. For different demagnetization currents, the variation of the demagnetization characteristics is plotted. From the results, it is observed that the knee point is reached around 800 A, and demagnetization starts to take place after this current value. If a higher $-I_d$ current is applied, the magnets start to demagnetize permanently, and the demagnetization curve is redefined with recoil lines.

4.6.2 Maximum Current Calculation

As a next step, the maximum possible $-I_d$ current is calculated considering the worst case scenario, where there is a short circuit at the terminals of the machine at rated speed operation. In this case, the terminal voltage is set to zero, and the following equations can be written

$$V_d = R_{ph}I_d - \omega_e L_{ph}I_q = 0 \quad (4.4)$$

$$V_q = R_{ph}I_q + \omega_e L_{ph}I_d + \omega_e \lambda_{PM} = 0 \quad (4.5)$$

where V_d and V_q are d-axis and q-axis voltages, respectively, R_{ph} and L_{ph} are phase resistance and inductance, respectively, ω_e is electrical speed, and λ_{PM} is permanent magnet flux linkage. These parameters are measured experimentally as follows

$$\lambda_{PM} = 0.153 \text{ V s} \quad (4.6)$$

$$R_{ph} = 0.1 \Omega \quad (4.7)$$

$$L_{ph} = 103 \mu\text{H} \quad (4.8)$$

Then, solving (4.4) and (4.5) together, I_q and I_d currents can be found for the considered short circuit case as follows

$$I_q = -\frac{\omega_e \lambda_{PM} R_{ph}}{R_{ph}^2 + (\omega_e L_{ph})^2} = -\frac{220 \cdot 0.153 \cdot 0.1}{0.1^2 + (220 \cdot 103\mu)^2} = -336 \text{ A} \quad (4.9)$$

$$I_d = \frac{\omega_e L_{ph} I_q}{R_{ph}} = \frac{220 \cdot 103\mu \cdot (-336)}{0.1} = -76 \text{ A} \quad (4.10)$$

Thus, it is seen that the worst case $-I_d$ current, which is -76 A , is less than the critical $-I_d$ current causing demagnetization, which is -800 A , in amplitude. This result means that whatever happens in the machine, there is no risk of demagnetization of the prototype optimum machine. This result is expected since the proposed machine topology has low voltage and high current characteristics. Therefore, the short circuit current is limited, and demagnetization risk is eliminated.

4.7 Summary

This chapter presented the experimental verification of the proposed axial flux machine employing a flat winding stator on 1.4 kW and 525 rpm prototype. As a first step, an optimization study is conducted with the objective function of minimizing active mass. The manufacturing stages of the prototype follow this. First, the manufacturing of the flat wires from 1 mm thick copper sheet using a laser cutter is presented. Electrical isolation, end winding connections, and epoxy coating are the followed steps of the manufacturing of the stator.

The open circuit test, which investigates the induced voltages at no-load, showed that less than 2 % difference between analytical, finite element analysis, and experimental results proves the accuracy of the analytical model and correctness of the material properties. The temperature characteristics and loading test of the prototype also

showed that the flat winding stator is capable of operating with current density up to 7 A/mm^2 . Also, experimental loss measurements prove that the analytical eddy current loss on the windings due to external PM field and DC winding loss models are accurate with less than 4 % and 2 % differences, respectively.

The feasibility of aluminum flat winding is investigated with experimental and analytical analysis. It is known that aluminum has weight and cost advantage over copper; however, it has higher resistivity. The analytical analysis and experimental loss measurements showed that aluminum has lower losses at high speed due to lower eddy current losses on the windings due to external PM field. However, at high torque region, copper has lower losses due to lower DC winding losses. Lastly, in the chapter, a demagnetization analysis for the prototype machine is presented. It is seen that at worst case, permanent magnets start to demagnetize at peak phase current of 800 A. However, the actual worst case peak phase current is 290 A. Thus, the chapter is concluded by stating that there is no risk of demagnetization for the prototype.

After ensuring the accuracy of the proposed analytical models with experimental verifications, the presented models can be scaled to evaluate the flat winding performance in large power machines. For that purpose, in the next chapter, 1 MW direct-drive wind turbine generator with flat winding stator is investigated.

CHAPTER 5

1 MW DIRECT-DRIVE WIND TURBINE GENERATOR

In this chapter, the feasibility of the proposed flat winding topology will be investigated in MW-class machines. The machines with this power level are typically used in power generation or propulsion applications. This study aims to design a direct-drive wind turbine generator to evaluate the performance of the flat winding.

In the last few decades, wind energy applications gained popularity due to increased demand for renewable energy resources [62, 63, 64]. According to WindEurope statistics, annual wind energy production in Europe in 2019 reached 15 % of the EU's electricity demand with a capacity increase of 15.2 GW in the previous year [65]. With the increasing demand for wind turbine generators, high efficient and reliable drivetrain solutions with high torque density become the primary focus of the researchers. In this context, direct-drive wind turbine generators are becoming more popular due to their reliability and low maintenance costs [66, 67]. Drivetrain solutions employing gearbox suffer from high failure rates due to high mechanical stresses [68, 69]. In particular, for offshore wind turbines, any failure in the gearbox may result in considerable downtimes, expensive maintenance costs, and economic losses. Therefore, many manufacturers of offshore wind turbine generators prefer to use direct-drive solutions [70, 71].

Direct-drive wind turbine generators have low rotational speed, high torque, and large diameter, which pose design and manufacturing challenges [72]. In order to overcome these challenges, several different topologies are presented in the literature. Radial flux iron-cored generators, which are commonly used in direct-drive wind turbines, are studied in [73, 74]. They suffer from limited torque density and elevated core losses. There are also non-conventional generators such as claw-pole or

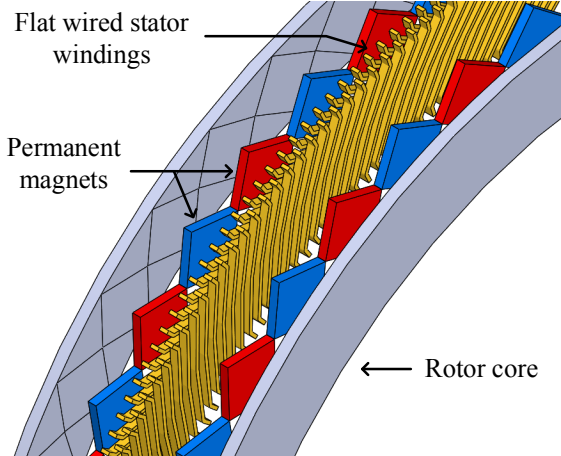


Figure 5.1: Exploded view of AFPM generator with novel flat winding for wind turbine applications

transverse-flux machines [75, 28], but they operate at low power factors [20, 76]. Superconducting direct-drive generators are also studied, and they promise high torque densities [77, 78, 79]. However, they are not mature enough for commercialization yet.

Wind turbines can be categorized as a horizontal axis and vertical axis wind turbines based on the rotor orientation. Vertical axis wind turbines are well suited for the axial flux generators, and there are examples of axial flux vertical axis wind turbines in the literature [80]. However, they are not common in the MW-range wind turbine market due to low capacity factors and poor performance [81, 82]. Therefore, in this thesis, the horizontal axis wind turbines are selected as a possible application for the proposed generator.

Similar to the prototype, axial flux permanent magnet machine topology is selected for wind turbine generator applications, as shown in Fig. 5.1. The magnetic design of the generator is the same as the prototype machine in a topology basis: an air-cored stator employing flat windings is sandwiched between two rotor discs with diagonally placed permanent magnets. However, the mechanical design is improved, as will be presented in the following section.

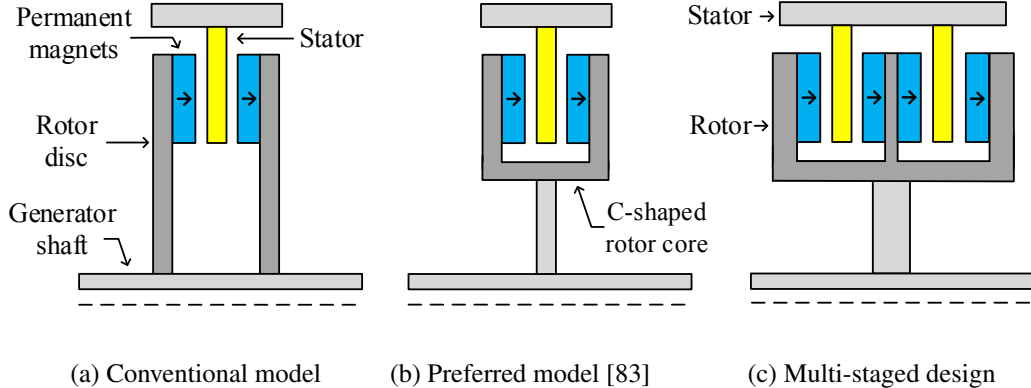


Figure 5.2: Structural models

5.1 Mechanical Structure

C-shaped rotor core and multi-staged design concepts are utilized in the mechanical design of the generator, and structural mass is evaluated. Structural mass estimation is an important step in the design of large-sized electric machines. Especially for the optimization of direct-drive wind turbine generators, both the cost and mass of the active materials decrease as the outer diameter increases for the same power rating. However, as the diameter increases, structural mass increases significantly. Therefore, the optimization problems ignoring structural mass may end up with incomplete or unrealistic results. Therefore, the structural model should be included in the optimization problem to get more realistic solutions.

5.1.1 C-shaped Core Design

In this study, instead of the conventional structural model shown in Fig 5.2a, the model shown in Fig. 5.2b is used. Mueller and McDonald propose this model for an air-cored axial flux machine [83]. In this model, instead of connecting two rotor discs directly to the shaft, they are connected to each other with a C-shaped rotor core, and they share the same rotor yoke. Then, this C-shaped core is connected to the shaft, as in Fig. 5.2b.

Compared to the conventional structural model, the preferred model has two main advantages. Firstly, since the rotor cores are connected to the shaft with one structural element, total structural mass is reduced. Secondly, since the lever arm is shorter, the deflection of the rotor cores resulting from the attraction force between magnets is smaller, which reduces the structural mass.

5.1.2 Multi-staged Design

Multi-stage or stacked generators can provide higher power density [28]. The axial flux wind energy generator presented in this thesis also has the advantage of stackability in the axial direction, as shown in Fig. 5.2c. As the power rating of the generator increases, the diameter of the generator tends to increase as well. The generator's diameter can be reduced by utilizing the multi-staged design, resulting in decreased structural mass. Therefore, compared to the single-stage configuration, the multi-stage configuration reduces the total mass of the generator, including the structural mass [84].

Also, the multi-stage designs benefit from modularity. This is particularly important for MW-class wind turbines with large diameters. Modular structure has a significant advantage in the manufacturing and transportation of the generator. Additionally, multi-stage configuration provides flexibility in series or parallel connection of stages.

5.2 Genetic Algorithm Optimization

In this section, the optimization of the generator model will be presented. Optimization is carried out with the analytical model proposed in Chapter 3. It is aimed to design a generator with a rated power of 1 MW at 20 rpm rotational speed for wind turbine applications. The genetic algorithm optimization files for the generator can be found in Appendix C.

In Table 5.1, the fixed design parameters used in the optimization process are tabulated. As in the prototype machine, NdFeB magnets of N42M grade with remanence flux density of 1.29 T are preferred. Also, a rotor core material with saturation flux

Table 5.1: Fixed design parameters

| Parameter | Value |
|---------------------------------------|--------|
| Rated power | 1 MW |
| Rated speed | 20 rpm |
| Remanence flux density of the magnets | 1.29 T |
| Phase number | 3 |
| Saturation flux density of the cores | 1.7 T |

Table 5.2: Optimization parameters

| Parameter | Minimum value | Maximum value |
|------------------------------------|---------------------|---------------------|
| Diameter | 2 m | 13 m |
| Number of poles | 10 | 160 |
| Current density | 1 A/mm ² | 9 A/mm ² |
| Number of stages | 1 | 14 |
| Number of parallel turns per stage | 1 | 8 |
| Flat wire width | 5 mm | 50 mm |
| Flat wire thickness | 1 mm | 10 mm |

density of 1.7 T is preferred. Focusing on the stator side, it is possible to utilize different flat winding materials, but copper is selected as flat wire material in this study.

There are seven optimization parameters, which are presented in Table 5.2, with their limits. The generator is assumed to be naturally cooled, and the current density is optimized accordingly. The limits of the current density are determined by considering the thermal performance of the manufactured prototype presented in Section 4.4. The multiple numbers of stages, as shown in Section 5.1.2, are also evaluated in the optimization process. Two optimization parameters are defining flat wire geometry: flat wire thickness, t , and width, w , which are shown in Fig. 2.5c. Note that the flat wire thickness is also the conductor sheet's thickness, from which flat wire is manufactured. Also, note that the flat wire width determines the axial length of the stator and also magnetic air gap defined by the distance between the rotor discs.

The objective of the optimization is to minimize the total mass, including structural mass. Since the output torque is determined by the fixed design parameters shown in Table 5.1, the objective of the optimization can also be stated as maximizing torque density defined in Nm/kg. Both the active and structural masses are taken into account in the total mass calculation. Additionally, minimum efficiency of 90 % and maximum line-to-line voltage of 690 V constraints are defined.

Therefore, the fitness function can be defined as

$$\begin{aligned}
 & \text{minimize } \{\text{total mass}\} \\
 & \text{subject to} \\
 & \text{efficiency} \geq 90\% \\
 & \text{line voltage} \leq 690 \text{ V}
 \end{aligned} \tag{5.1}$$

Similar to the optimization of the prototype machine, the genetic algorithm is selected as an optimizer and utilized on MATLAB with a fully analytical model presented before. The number of populations and generations are selected as 400 and 200, respectively.

5.2.1 Diameter Variation

In order to interpret the trade-offs between generator parameters, the outer diameter is set as a fixed variable, and seven different optimization problems are solved using the proposed optimization method. The results are presented in Fig. 5.3, from which the following can be concluded:

- As the diameter is increased, it is possible to reduce the PM mass, as shown in Fig. 5.3a. This results in decreased active mass, but structural mass increases with increasing diameter. There exists an optimum design, where total mass is minimum as depicted in Fig. 5.3b around the diameter of 5 m. This clearly shows why structural mass should also be included in the mass optimization problem of direct-drive wind turbine generators.
- The cost of the generator is dominated by the permanent magnet cost. Therefore, the increasing diameter decreases the total material cost.

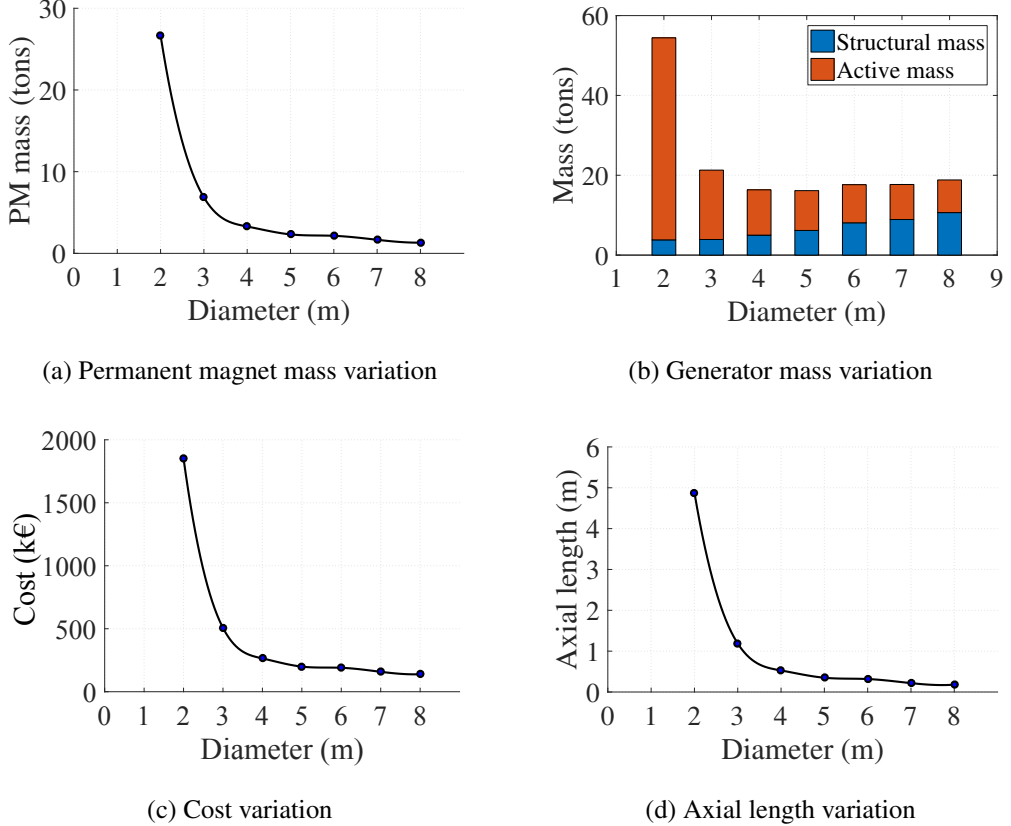


Figure 5.3: The variation of generator parameters against diameter

- At small diameters, the generator lacks the induced voltage due to decreased linear speed of the conductors and decreased number of flat wires. Therefore, the algorithm converges to designs with multiple numbers of stages.

5.2.2 Flat Wire Thickness Variation

One of the most critical parameters for both efficiency and manufacturability is the thickness of the conductor sheet, from which the flat wire is manufactured. Manufacturing of the stator includes cutting and bending stages, as depicted in Fig. 2.5. Therefore, the selection of flat wire thickness may affect the manufacturing cost and difficulty. For better visualization, a section of two generators having the same rotors and different flat wire thicknesses are shown in Fig. 5.4. Three loops of flat winding in Fig. 5.4a occupy the same area as seven loops of flat winding in Fig. 5.4b.

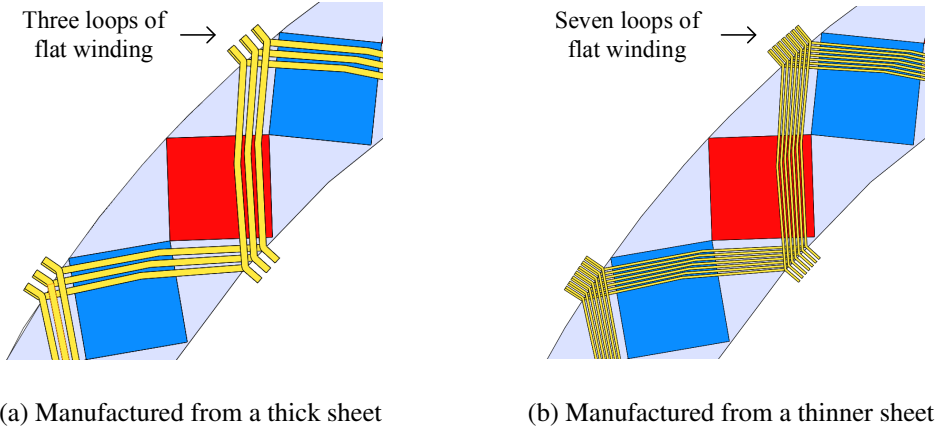


Figure 5.4: Two designs with different flat wire thicknesses

Similar to the previous study, the parameter of flat wire thickness is fixed, and several optimization problems are solved with different flat wire thicknesses. Other optimization parameters in Table 5.2, such as diameter or current density, are set free within their limits. Variation of the some critical generator parameters with flat wire thickness is shown in Fig. 5.5, from which the following conclusions can be drawn:

- As the flat wire thickness is increased, the eddy current losses on the stator due to external PM field increase due to the larger cross-sectional area. Increased eddy current losses lead to designs with lower DC winding losses because of the minimum efficiency constraint, as shown in Fig. 5.5a. For the optimum design with 1 mm flat wire thickness, eddy current losses on the windings due to external PM field are 2 % of the total losses, which increase to 34 % with a flat wire thickness of 6 mm.
- The eddy current loss on the windings is proportional to the square of the electrical frequency as presented in (3.48). In order to limit eddy current losses, the algorithm converges to designs with less electrical frequency and pole number.
- The DC winding losses are proportional to the square of the current density and total volume of the flat wires. In order to limit the DC winding losses, the current density is decreased, as shown Fig. 5.5c. However, note that the generator's rated current increases even if the current density is decreased due to increased flat wire thickness and cross-sectional area.

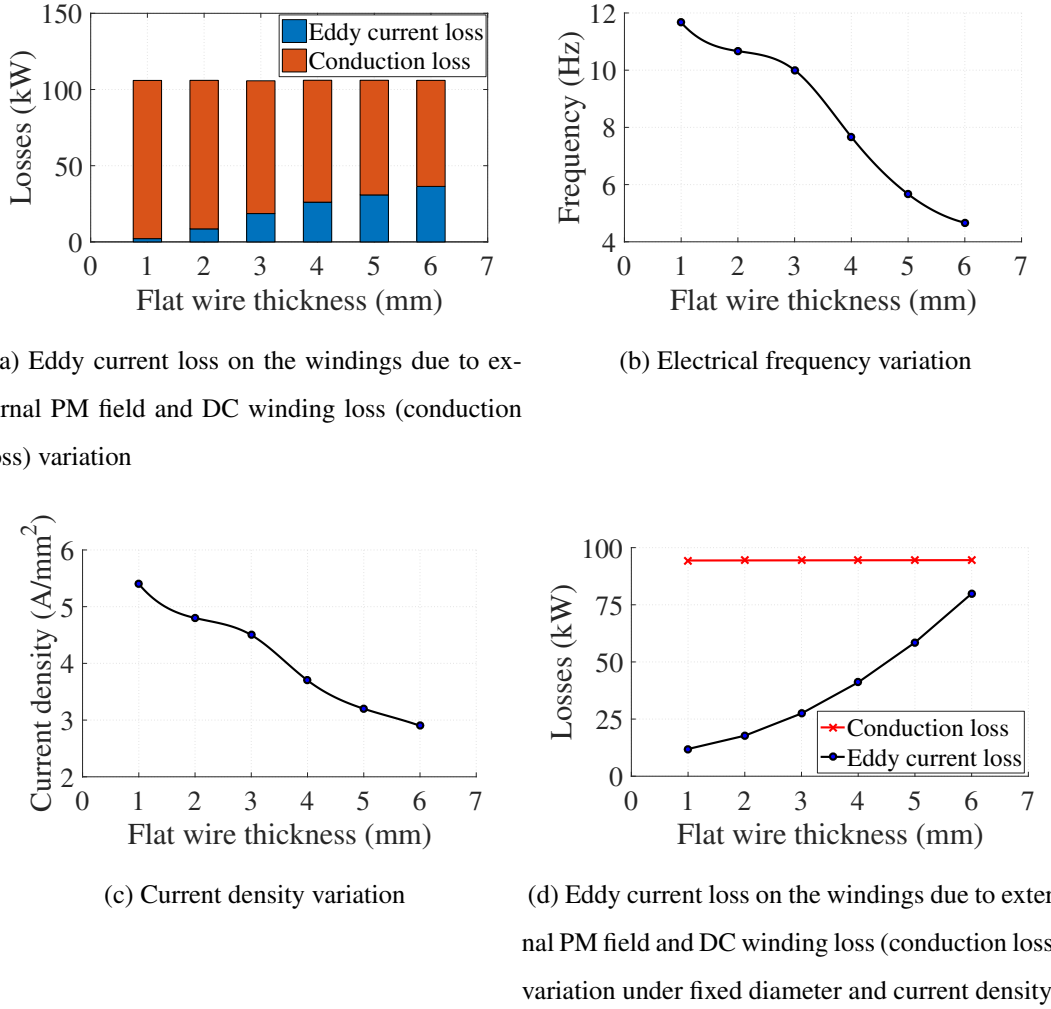


Figure 5.5: The variation of generator parameters against flat wire thickness

In Fig. 5.5d, the variation of the DC winding losses and eddy current losses on the windings due to external PM field against flat wire thickness is given. Unlike the previous study, in this analysis, machine parameters such as diameter, current density, electrical frequency, or rotor geometry are fixed, and only flat wire thickness is changed without the optimization process. As the flat wire thickness is varied, the total number of flat wires also changes linearly. This variation effectively changes the current and voltage ratings of the generator. Note that the total volume of the conductors used does not change in this analysis. Under the same current density, this leads to the conclusion that DC winding losses do not change. However, the eddy current losses on the windings due to external PM field increase with increasing material thickness, as presented by (3.48).

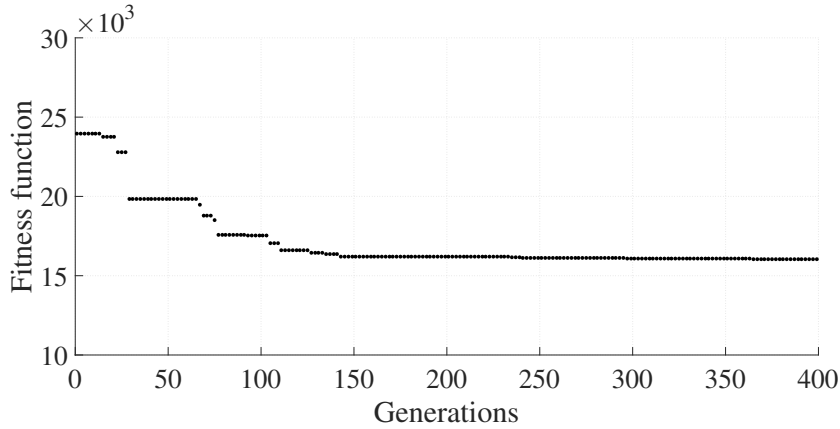


Figure 5.6: Convergence plot of the genetic algorithm

5.2.3 The Optimum Design

After figuring out the trade-offs between generator parameters, the optimization problem is solved once again with the optimization parameters in Table 5.2. The convergence plot given in Fig. 5.6 shows that the genetic algorithm converged to the optimum design with a total mass of 16 t. The parameters of the optimum design are tabulated in Table 5.3. It is a two-stage, 1 MW, 480 kNm design with 4.8 m diameter. It is seen that both the efficiency and line voltage parameters converged to a value close to their limits. The total mass of the generator is dominated by 10.4 t of active mass, and the structural mass is calculated as 5.6 t. The current density parameter is converged to 3.8 A/mm^2 in the optimum design. This much current density is proven to be safe thermally by the experimental verification of the prototype machine shared in Section 4.4. Also, the aspect ratio of the optimum design, defined as the ratio of axial length to the outer diameter of the generator, is calculated as 0.075. This value is close to the optimum aspect ratio for the axial flux machines with high pole numbers (≥ 10) [85]. Additionally, the total cost of the optimum design is € 203 k, according to specific costs given in Table 5.4. Since the single objective of the algorithm is minimizing the mass, more cost-effective solutions can be achieved when the cost is also added to the fitness function.

The mechanical drawing of the optimum design is given in Fig. 5.7 with the full model and its section view. In Appendix C, the electromagnetic model in ANSYS Maxwell and the mechanical model in SolidWorks are given for the optimized generator.

Table 5.3: Optimized 1 MW, 20 rpm generator design parameters

| Parameter | Value |
|------------------------------------|-----------------------|
| Rated power | 1 MW |
| Rotational speed | 20 rpm |
| Diameter | 4.8 m |
| Line rms voltage | 680 V |
| Line rms current | 850 A |
| Number of poles | 46 |
| Torque | 480 kNm |
| Axial length | 0.36 m |
| Aspect ratio | 0.075 |
| Efficiency | 90 % |
| DC winding losses | 75 kW |
| Eddy losses on windings by PM | 31 kW |
| Active mass | 10.4 t |
| Structural mass | 5.6 t |
| Total mass | 16.0 t |
| Torque density | 29.8 Nm/kg |
| Electrical frequency | 7.7 Hz |
| Number of stages | 2 |
| Number of parallel turns per stage | 2 |
| Current density | 3.8 A/mm ² |
| Flat wire width | 18.6 mm |
| Flat wire thickness | 3 mm |
| Total cost | € 203 k |
| Air gap peak flux density | 0.85 T |

Focusing on the feasibility and manufacturing of 1 MW optimum design, the proposed flat winding stator can be manufactured by simple modifications on the production line used for the existing solutions. Even though laser or water jet may increase the manufacturing cost compared to conventional stranded wire technology,

Table 5.4: Specific costs of the materials [86]

| Parameter | Value |
|-----------------------|--------|
| Copper cost | €15/kg |
| Permanent magnet cost | €60/kg |
| Rotor iron cost | €2/kg |
| Structural steel cost | €2/kg |

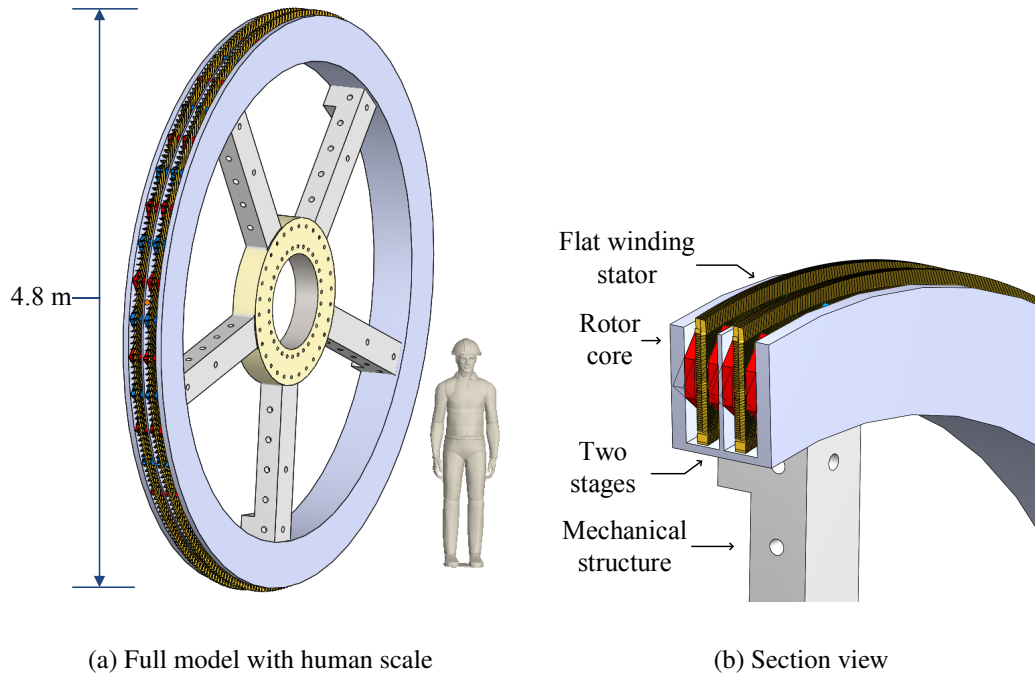


Figure 5.7: The optimum 1 MW and 20 rpm design

stamping press machines can provide an economical solution for high volume production. These machines are already being used in the manufacturing of the rotor and stator laminations. With simple modifications on the production line, flat wires for the optimum design can be manufactured from 3 mm thick copper sheet using stamping press machines. Rotor and structural parts of the optimum design are similar to the existing technology for the axial flux machines on topology. Therefore, they can be manufactured using existing tools dedicated to the mass production of the current technology.

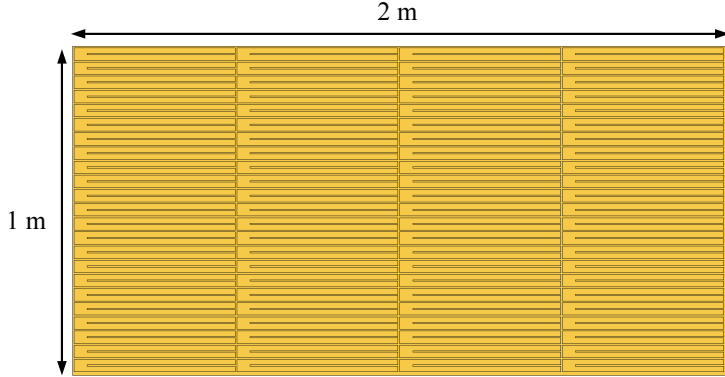


Figure 5.8: Sample manufacturing cut-out of 92 flat wires from copper sheet with dimensions of 1 m and 2 m using a planar cutting tool such as laser

For the flat winding stator of the optimum design, 2898 flat wires shown in Fig. 2.5 are required for each stage. They can be manufactured from a 3 mm thick copper sheet using a stamping press machine. Each flat wire cut covers an area with 38 mm of width and 490 mm of height. In order to give an idea about the manufacturing of flat wires from a copper sheet, a sample cut-out of flat wires from a copper sheet with dimensions of 1 m and 2 m is given in Fig. 5.8. From the copper sheet with these standardized dimensions, 92 flat wires can be manufactured. This means that 32 copper sheets are required for each stage, and 63 copper sheets are enough for the optimum design with double stages.

For the optimum design, a rough estimate of the manufacturing cost can be obtained for the flat winding stator among the proposed manufacturing methods: laser, water jet cutting, and stamping press machines. The flat winding stator's manufacturing cost will be dominated by the cutting cost of the metal sheet. Roughly, the operation costs of laser and water jet cutting are €0.11 and €0.77 per meter, respectively [87]. For the flat winding stator of the optimum design, this results in cutting the cost of €1200 for laser and €8500 for water jet. However, in mass production, stamping press machines decrease both the manufacturing cost and time compared to laser and water jet cutter even though it has high tooling cost [88]. Moreover, stamping press machines can do stamping and bending operations simultaneously, which reduces the manufacturing cost further. Therefore, it is favorable to use the stamping press method to manufacture flat winding stators for higher volumes.

5.3 Thermal analysis of the optimum design

In order to evaluate the thermal behavior of the optimum design, a finite element analysis is run on SolidWorks, whose simulation file can be found in Appendix C. The flat windings and the epoxy around the windings are modeled, and the DC winding losses and eddy current losses of the stator due to external PM field are included in the analysis. First, considering a rated operation, 106 kW of total heat power, which represents DC winding losses and eddy current losses on the windings due to external PM field, is generated on the windings. Then, assuming forced air cooling is used in the system, $50 \text{ W}/(\text{m}^2 \text{ K})$ convection coefficient is defined on the faces of the stator.

In Fig. 5.9a and Fig. 5.9b, the modeled stator part is shown with two different views. The windings are fully covered with epoxy in the model, and the ambient temperature is set to 28°C . At the end of the thermal analysis, it is observed that at rated operation, the windings are exposed to 90°C temperature increase and the maximum temperature is 118°C as can be seen in Fig. 5.9c. This thermal behavior proves that the optimum design having current density of $3.8 \text{ A}/\text{mm}^2$ is thermally safe, and the temperature limits are not exceeded.

The thermal performance of the optimum design can be further improved by partially coating the stator windings with epoxy, as shown in Fig. 5.10a, instead of fully coating the stator windings as in Fig. 5.9a. The thermal conductivity of copper is around $400 \text{ W}/(\text{m K})$ [89]. However, the thermal conductivity of epoxy resin is around 1 to $10 \text{ W}/(\text{m K})$ depending on the material properties [90]. Therefore, the copper is at least 40 times thermally conductive than epoxy resin.

In order to take advantage of this, the windings can be coated partially with epoxy. This provides two advantages. First, due to direct contact of the flat windings with air, the heat can be evacuated easily due to the high thermal conductivity of copper. Second, flat windings have a finned structure similar to the heat sinks. Therefore, the total surface area contacting with air increases with partial coating, as in Fig. 5.10a.

It is observed that the maximum temperature increase is around 40°C , which is 56 % less than the fully coated case in Fig. 5.9. With that result, it can be concluded that the electrical loading of the generator can be increased more. In fact, the electrical load-

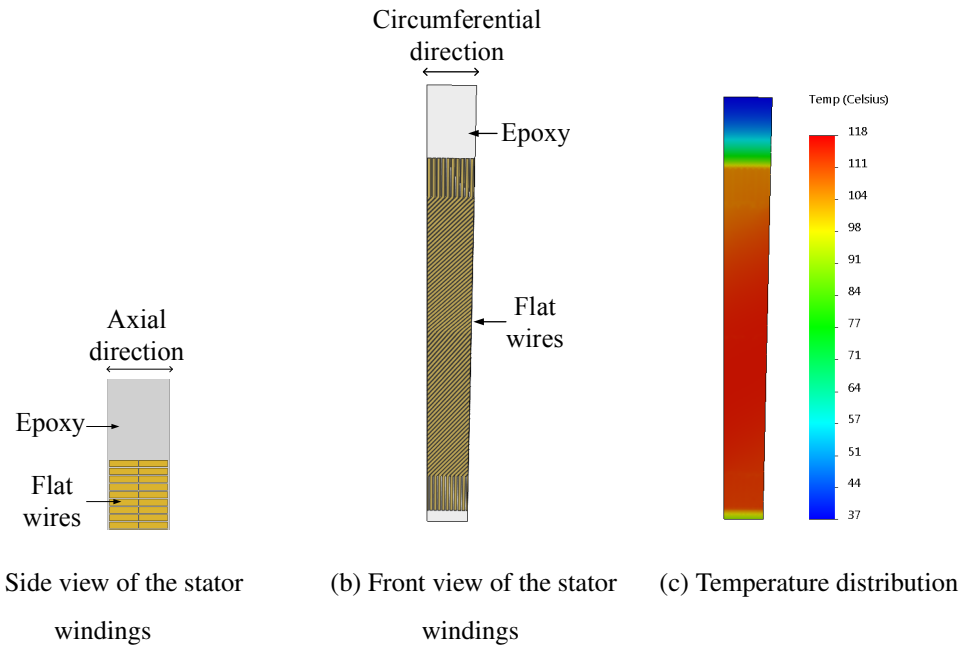


Figure 5.9: Thermal analysis of the optimum design at rated operation

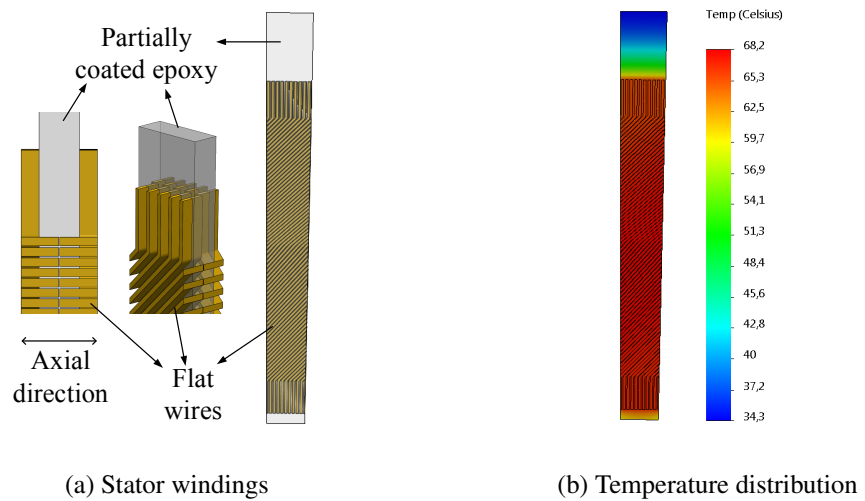


Figure 5.10: Thermal analysis of the partially coated stator design

ing of the generator can be increased 66 % to achieve the same temperature increase of 90 °C as in the fully coated case. This means that the power and torque density of the generator can be increased significantly with this method. Overall, the proposed optimum design is able to operate in a thermally safe region at the rated operation.

Table 5.5: Comparison of the optimum design with other direct-drive permanent magnet generators studied in the literature

| | Li <i>et al.</i> [91] | This study | McDonald <i>et al.</i> [92] | Maples <i>et al.</i> [93] | Versteegh [94] | Bang [95] |
|---|--------------------------|-------------------|--------------------------------|------------------------------|-------------------|--------------|
| Generator type | RFPM ¹ | AFPM ² | AFPM | RFPM | RFPM | RFPM |
| Power, MW | 0.75 | 1 | 1 | 1 | 1.5 | 2 |
| Speed, rpm | 29 | 20 | 12 | 26 | 18 | 20 |
| Torque, kNm | 250 | 477 | 798 | 367 | 796 | 979 |
| Number of stages | 1 | 2 | 4 | 1 | 1 | 1 |
| Active mass, t | 3.1 | 10.4 | 18.6 | - | 16.7 | 14.6 |
| Structural mass, t | - | 5.6 | 6.9 | - | 20.8 | 10.4 |
| Total mass, t | - | 16.0 | 25.5 | 17.4 | 37.5 | 25.0 |
| Torque density by active mass, Nm/kg | 79.7 | 46.0 | 42.9 | - | 47.7 | 67.0 |
| Torque density by total mass, Nm/kg | - | 29.8 | 31.3 | 21.0 | 21.2 | 39.2 |

¹ Radial flux permanent magnet machine

² Axial flux permanent magnet machine

5.4 Comparison of the Optimum Design with Existing Technologies

In this section, the optimum design is compared with wind power generators presented in the literature. In comparison study, direct-drive permanent magnet generators with power ratings between 0.75 MW and 2 MW are considered [91, 92, 93, 94, 95]. The results are tabulated in Table 5.5. Torque density (Nm/kg) is selected as the performance parameter. Some of the publications do not include active, structural, or total mass data. Therefore, two definitions of torque density considering either active or total mass are made. The results show that the optimum design presented in this paper has comparable torque density, especially with 29.8 Nm/kg torque density including structural mass. Also, it is seen that the presented structural model and multi-staged design creates a significant advantage in terms of torque density by total mass in the comparative study.

The main advantage of the proposed generator stands out in manufacturing. Instead of conventional stranded wires, the flat wire proposed in this paper provides ease of manufacturing. The whole stator structure can be manufactured by cutting, bending, and welding processes. Additionally, air-cored stator design eliminates the problems related to high attraction force between rotor and stator parts of the generator, as well as decreases the structural mass.

5.5 Demagnetization Analysis

For reliable operation, a demagnetization analysis is required for the permanent magnet machines. In that context, a demagnetization analysis is carried out considering the worst-case scenario for the 1 MW generator in this section.

In Section 4.6, for 1.4 kW prototype machine, a similar analysis is presented. In the section, the causes for demagnetization, typical B-H or demagnetization characteristics, the recoil line, and spatial distribution of the direct and quadrature axes for the proposed axial flux machine topology are presented. Additionally, the demagnetization analysis procedure is shared, in which only $-I_d$ current is applied, and the operation point of the permanent magnets is observed via observation points inside the magnets using finite element analysis (FEA). Therefore, since the concept and the detailed procedure for the analysis are presented in Section 4.6, they will not be repeated in this section for the 1 MW generator.

First, using FEA, demagnetization characteristics of the permanent magnets for different peak demagnetization currents are obtained as in Fig. 5.11, where the original demagnetization characteristic for N42M magnet at 80 °C is also presented. The figure shows that the knee point is reached, and the recoil line starts to appear at the peak current of 3.2 kA. Beyond this current, irreversible demagnetization occurs, and permanent performance loss of the machine is observed. The electromagnetic model used for this analysis is given in Appendix C.

Next, an analytical analysis is conducted for the demagnetization current calculation considering the worst case scenario. For this fault case, it is assumed that there is a short circuit at the terminals of the machine, and the terminal voltage becomes zero

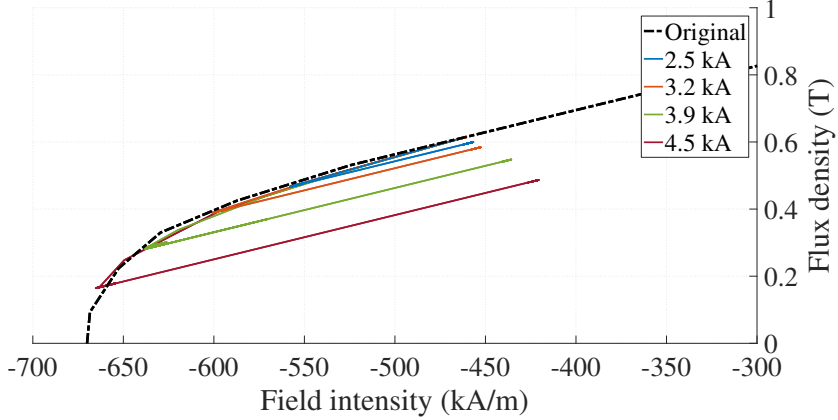


Figure 5.11: Demagnetization characteristic of the permanent magnet at different peak short circuit phase currents

instantly. A similar analysis is carried out in Section 4.6 for the prototype machine. In this situation, the analytical derivation of $-I_d$ current can be carried out as follows

$$I_q = -\frac{\omega_e \lambda_{PM} R_{ph}}{R_{ph}^2 + (\omega_e L_{ph})^2} = -\frac{48 \cdot 11.5 \cdot 0.041}{0.041^2 + (48 \cdot 0.00174)^2} = -2.6 \text{ kA} \quad (5.2)$$

$$I_d = \frac{\omega_e L_{ph} I_q}{R_{ph}} = \frac{48 \cdot 0.00174 \cdot I_q}{0.041} = -5.3 \text{ kA} \quad (5.3)$$

It is seen that the $-I_d$ current in the considered fault case, which is -5.3 kA , higher than the critical $-I_d$ current that cause demagnetization, which is -3.2 kA , in magnitude. These result shows that permanent magnets demagnetize irreversibly when there is a short circuit fault at the terminals of the phases and when the magnetic field is created through $(-d)$ -axis direction. This also implies that there is demagnetization risk for the different fault cases.

Remember that this was not the case for the prototype machine, as analyzed in Section 4.6. It was found that peak demagnetization current for the considered fault case does not cause irreversible demagnetization, and there was no risk of demagnetization in any case. However, for 1 MW generator, there is a risk of demagnetization in a fault situation, and it should be considered for reliable operation.

In order to eliminate the demagnetization risk, several precautions can be taken. For instance, permanent magnets that are tolerant to high temperatures can be preferred.

In the design, N42M grade magnets are used, and it is known that N42H or N42UH magnets are able to operate at higher temperatures. Therefore, these magnets can be used instead of N42M grade magnets at the expense of increased cost. Moreover, the conducted analysis assumed that the magnets' temperature is 80 °C, which may not be the case because the losses on the magnets are expected to be low due to the synchronous rotation of the double-sided rotor discs. Nevertheless, it is important to observe the temperature of the magnets for reliable operation.

5.6 Summary

This chapter investigated the performance of the flat winding topology on a 1 MW axial flux permanent magnet direct-drive wind turbine generator. Firstly, the optimization study using genetic algorithm is presented with a fully analytical model. The constraints and optimization variables are defined considering the aimed with turbine application specifications, and the objective function is set to minimize the total mass of the generator, including the structural mass. In order to gain a deeper understanding of the trade-offs among machine parameters, the generator is optimized with different diameters and flat wire thicknesses, separately. Lastly, the optimized 1 MW, 20 rpm, and double-staged generator is presented. It is observed that the optimum design converged to a diameter of 4.8 m, flat wire thickness of 3 mm, and total mass of 16 t. Also, the thermal analysis of the optimized generator is conducted on SolidWorks. It is observed that the generator is thermally safe; moreover, the electrical loading of the generator can be increased 66 % by partially coating the flat winding stator.

Additionally, the optimum design is compared with direct-drive wind turbine generators studied in the literature. The results show that the optimized design has reached the torque density of 29.8 Nm/kg, including total mass, which is a promising value when compared to other generators. Moreover, the manufacturing advantages of the proposed flat winding topology makes the proposed generator more attractive. Lastly, in the chapter, the demagnetization analysis using finite element analysis is presented. It is shown that there is a risk of demagnetization in the worst-case, unlike the prototype. Several precautions are recommended to decrease the demagnetization risk.

CHAPTER 6

CONCLUSIONS AND FUTURE WORKS

In a typical electric machine, conventional windings with stranded round wires are employed. These windings may not meet the increasing performance demand in an electric machine at some points, such as current density or end winding losses. Therefore, this thesis aims to find a novel winding solution as an alternative to conventional windings.

The proposed winding is made of a thin conductor sheet, and it is called ‘flat winding.’ It can be manufactured using a laser cutter, water jet, or even stamping press machines. Flat winding is able to outperform the conventional windings at many points. In Table 6.1, the comparison is presented, including other winding topologies. It is shown that the flat winding promises ease of manufacturing advantage because it can be manufactured with the tools that are used in the manufacturing of electric machines, such as stamping press, and not much modification is needed on the production line. Also, it is experimentally shown that the flat winding is able to operate with current density up to 7 A/mm^2 . Other advantages, such as short end winding length, lower end winding losses or superior current ratings, make the flat finding an attractive solution.

In order to evaluate the performance of flat winding, it is implemented on an axial flux permanent magnet machine. The topology has a double-sided rotor and one air-cored stator employing flat windings, which is sandwiched between two rotor discs. In the thesis, first, the analytical modeling of the machine, including field, torque, voltage, and losses modelings, is presented. These models are then verified on 1.4 kW prototype, and the promised advantages of the flat winding are shown on a real machine. Additionally, the aluminum and copper flat windings are compared

Table 6.1: Comparison of the winding topologies

| | Flat winding | Conventional round winding | Hairpin winding | PCB winding |
|-----------------------|-----------------|-------------------------------|--------------------|----------------|
| Ease of manufacturing | ++ | + | + | ++ |
| Current density | ++ | - | + | ++ |
| Current rating | ++ | + | ++ | - |
| Manufacturing cost | + | + | - | -- |
| End winding length | ++ | + | - | + |
| Eddy current loss | + | ++ | - | + |

'+' sign means advantage

analytically and experimentally. Lastly, the flat winding performance is evaluated on 1 MW direct-drive axial flux wind turbine generator. From these analyses, the following key conclusions can be drawn:

- The proposed axial flux topology has critical advantages such as high torque density, absence of cogging torque, and eliminated core losses on the stator. Thus, when combined with the superiorities of the flat winding, the machine's overall performance can be boosted.
- Having the analytical model of the topology is critical in the design of electric machines. The presented analytical magnetic field, torque, induced voltage, DC winding loss, and eddy current loss models agree well with the finite element analysis and experimental results. Thus, they can be used in the design of axial flux permanent magnet air-cored machines.
- Due to its large cross-sectional area, flat winding has a risk of high eddy current losses on the windings due to external PM field, like hairpin winding. However, the eddy current losses can be suppressed by manufacturing from a thin conductor sheet and staking them through thickness in the circumferential direction. By this method, it is shown on the prototype that eddy current losses on the windings are less than the DC winding losses. This proves the superior performance of flat winding over hairpin windings in terms of eddy current losses.

- According to experimentally obtained thermal characteristics, the flat wires are capable of achieving current density up to 7 A/mm^2 . Thus, it outperforms the conventional windings with stranded round wires in terms of current density.
- It is shown both analytically and experimentally that the aluminum flat winding is a feasible alternative to the copper flat winding at some operating regions in terms of losses, efficiency, cost, and weight. At high-speed region, eddy current losses on the windings due to external PM field dominate the DC winding losses. Due to its higher skin depth, aluminum has lower eddy current losses in this region, which is favorable at high-speed operation. However, at the high torque region, copper is favorable due to its lower resistivity and lower DC winding losses.
- The superior performance of flat winding topology is also proven on MW-class machines. 1 MW and 20 rpm direct-drive axial flux wind turbine generator employing flat winding stator is designed. It is shown that the optimized generator has a torque density of 29.8 Nm/kg , considering total mass, which is quite comparable with existing generators with conventional stranded round wires.
- In overall, the conducted analyses show that the proposed flat winding topology made of a thin conductor sheet is a promising alternative to the conventional windings with round wires. Thus, it is expected to see the flat winding topology on some applications in the future.

6.1 Future Work

Through the thesis, electromagnetic and mechanical analyses are evaluated in detail. However, thermal analysis needs more investigation. In Section 5.3, it is shown that by partially coating the flat windings with epoxy, the electrical loading can be increased by 66 %. Experimental verification on the manufactured prototype would be promising work for this study. Also, for the proposed topology, the magnets on the double-sided rotor discs create a fan effect on the flat winding stator. This can be further improved by customized magnet shape or by additional elements. By these arrangements, the electrical loading of the flat windings can be further increased.

In the thesis, the machines with rotational speed up to 1000 rpm are evaluated. However, the performance of the flat winding on high-speed machines needs further investigation. At high-speed operation, it is expected that the aluminum flat windings can outperform the conventional round windings.

The performance of the flat winding is evaluated only on axial flux machines. Additionally, the authors also investigated the flat winding on a double-sided linear machine in [48]. However, further research is needed to see flat winding performance on other machine topologies, such as radial flux machines. It would be an interesting research to conduct an electromagnetic, thermal, and structural analysis of a radial flux machine with flat winding and compare its performance with the axial flux counterpart in the thesis. Additionally, linear machines can also be stacked in the axial direction similar to the multi-stage design presented in Section 5.1.2 in order to increase modularity [96]. A linear multi-staged machine with flat winding is a possible future work of this study.

During the aluminum flat winding stator manufacturing, end winding welding was challenging because the aluminum can not be welded with simple soldering as copper can. Therefore, novel manufacturing methods for the proposed flat winding can be possible future work of this study. It is estimated that the flat winding stator can be manufactured using CNC from a cylinder block by milling and drilling operations. Although this can increase the manufacturing cost, manufacturing can be more automated. Additionally, different manufacturing methods, such as stamping press, laser, or water jet, can be compared in terms of cost, accuracy, and ease of manufacturing. Also, different end winding welding techniques can be investigated, such as soldering, TIG welding, MIG welding, laser welding, tin plating, or ultrasonic welding.

REFERENCES

- [1] D. Staton, A. Boglietti, and A. Cavagnino, “Solving the more difficult aspects of electric motor thermal analysis in small and medium size industrial induction motors,” *IEEE Transactions on Energy Conversion*, vol. 20, no. 3, pp. 620–628, 2005.
- [2] Taizhou Chuangpu Machinery and Electricity, “Basic knowledge of stator winding.” www.ixymotor.com. Accessed: 2020-08-19.
- [3] D. G. Dorrell, M. Hsieh, M. Popescu, L. Evans, D. A. Staton, and V. Grout, “A review of the design issues and techniques for radial-flux brushless surface and internal rare-earth permanent-magnet motors,” *IEEE Transactions on Industrial Electronics*, vol. 58, no. 9, pp. 3741–3757, 2011.
- [4] M. Aoyama and J. Deng, “Visualization and quantitative evaluation of eddy current loss in bar-wound type permanent magnet synchronous motor for mild-hybrid vehicles,” *CES Transactions on Electrical Machines and Systems*, vol. 3, pp. 269–278, Sep. 2019.
- [5] M. Popescu, J. Goss, D. A. Staton, D. Hawkins, Y. C. Chong, and A. Boglietti, “Electrical vehicles-practical solutions for power traction motor systems,” *IEEE Transactions on Industry Applications*, vol. 54, pp. 2751–2762, May 2018.
- [6] H. Park and M. Lim, “Design of high power density and high efficiency wound-field synchronous motor for electric vehicle traction,” *IEEE Access*, vol. 7, pp. 46677–46685, 2019.
- [7] C. Liu, Z. Xu, D. Gerada, J. Li, C. Gerada, Y. C. Chong, M. Popescu, J. Goss, D. Staton, and H. Zhang, “Experimental investigation on oil spray cooling with hairpin windings,” *IEEE Transactions on Industrial Electronics*, vol. 67, no. 9, pp. 7343–7353, 2020.

- [8] S. Jurkovic, K. Rahman, B. Bae, N. Patel, and P. Savagian, “Next generation Chevy Volt electric machines; design, optimization and control for performance and rare-earth mitigation,” *2015 IEEE Energy Conversion Congress and Exposition (ECCE)*, pp. 5219–5226, 2015.
- [9] T. Burress, “Electrical performance, reliability analysis, and characterization,” *2017 US DOE Vehicle Technologies Office Annual Merit Review, US Department of Energy*, pp. 1–25, 2017.
- [10] Special Machine Tool, “Hairpin winding technology.” www.specialmachinetool.it. Accessed: 2020-08-19.
- [11] Fraunhofer-Institute for Manufacturing Technology and Advanced Materials, “Coils produced by casting.” www.generativ.fraunhofer.de. Accessed: 2020-08-19.
- [12] S. Lomheim, *Analysis of a Novel Coil Design for Axial Flux Machines*. Msc dissertation, Norwegian University of Science and Technology, Trondheim, Norway, June 2013.
- [13] M. Groninger, F. Horch, A. Kock, M. Jakob, and B. Ponick, “Cast coils for electrical machines and their application in automotive and industrial drive systems,” *2014 4th International Electric Drives Production Conference (EDPC)*, pp. 1–7, 2014.
- [14] M. Groninger, F. Horch, A. Kock, H. Pleteit, B. Ponick, D. Schmidt, and F. Wostmann, “Casting production of coils for electrical machines,” *2011 1st International Electric Drives Production Conference*, pp. 159–161, 2011.
- [15] N. Salim, S. P. Nikam, S. Pal, A. K. Wankhede, and B. G. Fernandes, “Multi-physics analysis of printed circuit board winding for high-speed axial flux permanent magnet motor,” *IET Electric Power Applications*, vol. 13, no. 6, pp. 812–818, 2019.
- [16] X. Wang, W. Pang, P. Gao, and X. Zhao, “Electromagnetic design and analysis of axial flux permanent magnet generator with unequal-width PCB winding,” *IEEE Access*, vol. 7, pp. 164696–164707, 2019.

- [17] F. Marignetti, G. Volpe, S. M. Mirimani, and C. Cecati, “Electromagnetic design and modeling of a two-phase axial-flux printed circuit board motor,” *IEEE Transactions on Industrial Electronics*, vol. 65, no. 1, pp. 67–76, 2018.
- [18] G. H. Jang and J. H. Chang, “Development of an axial-gap spindle motor for computer hard disk drives using PCB winding and dual air gaps,” *IEEE Transactions on Magnetics*, vol. 38, no. 5, pp. 3297–3299, 2002.
- [19] M. Mirzaei, M. Mirsalim, and S. E. Abdollahi, “Analytical modeling of axial air gap solid rotor induction machines using a quasi-three-dimensional method,” *IEEE Transactions on Magnetics*, vol. 43, no. 7, pp. 3237–3242, 2007.
- [20] H. Polinder, J. A. Ferreira, B. B. Jensen, A. B. Abrahamsen, K. Atallah, and R. A. McMahon, “Trends in wind turbine generator systems,” *IEEE Journal of Emerging and Selected Topics in Power Electronics*, vol. 1, no. 3, pp. 174–185, 2013.
- [21] Xu Tongle, Zhang Xinyi, and Jia Qingxuan, “Rolling bearing fault analysis and wavelet thresholding research,” in *International Conference on Advanced Technology of Design and Manufacture (ATDM 2010)*, pp. 185–189, 2010.
- [22] A. Parviainen, M. Niemela, J. Pyrhonen, and J. Mantere, “Performance comparison between low-speed axial-flux and radial-flux permanent-magnet machines including mechanical constraints,” in *IEEE International Conference on Electric Machines and Drives, 2005.*, pp. 1695–1702, 2005.
- [23] A. Parviainen, *Design of axial-flux permanent-magnet low-speed machines and performance comparison between radial-flux and axial-flux machines*. Phd dissertation, Lappeenranta University of Technology, Lappeenranta, Finland, Apr. 2005.
- [24] W. Geng and Z. Zhang, “Analysis and implementation of new ironless stator axial-flux permanent magnet machine with concentrated nonoverlapping windings,” *IEEE Transactions on Energy Conversion*, vol. 33, no. 3, pp. 1274–1284, 2018.

- [25] M. Aydin, Surong Huang, and T. A. Lipo, “Torque quality and comparison of internal and external rotor axial flux surface-magnet disc machines,” *IEEE Transactions on Industrial Electronics*, vol. 53, no. 3, pp. 822–830, 2006.
- [26] K. Sitapati and R. Krishnan, “Performance comparisons of radial and axial field, permanent-magnet, brushless machines,” *IEEE Transactions on Industry Applications*, vol. 37, no. 5, pp. 1219–1226, 2001.
- [27] Surong Huang, Jian Luo, F. Leonardi, and T. A. Lipo, “A comparison of power density for axial flux machines based on general purpose sizing equations,” *IEEE Transactions on Energy Conversion*, vol. 14, no. 2, pp. 185–192, 1999.
- [28] K. Kails, Q. Li, and M. Mueller, “Modular and stackable power generators for efficient renewable power generation,” *IET Renewable Power Generation*, vol. 13, no. 15, pp. 2774–2782, 2019.
- [29] K. M. Rahman, N. R. Patel, T. G. Ward, J. M. Nagashima, F. Caricchi, and F. Crescimbini, “Application of direct-drive wheel motor for fuel cell electric and hybrid electric vehicle propulsion system,” *IEEE Transactions on Industry Applications*, vol. 42, no. 5, pp. 1185–1192, 2006.
- [30] C. H. T. Lee, K. T. Chau, C. Liu, T. W. Ching, and F. Li, “A high-torque magnetless axial-flux doubly salient machine for in-wheel direct drive applications,” *IEEE Transactions on Magnetics*, vol. 50, no. 11, pp. 1–5, 2014.
- [31] P. Duck, P. Lesniewski, and B. Ponick, “Design and analysis of axial-flux permanent magnet synchronous machines as traction drives for electric vehicles,” in *2016 International Symposium on Power Electronics, Electrical Drives, Automation and Motion (SPEEDAM)*, pp. 376–381, 2016.
- [32] T. D. Nguyen, K. Tseng, S. Zhang, and H. T. Nguyen, “A novel axial flux permanent-magnet machine for flywheel energy storage system: Design and analysis,” *IEEE Transactions on Industrial Electronics*, vol. 58, no. 9, pp. 3784–3794, 2011.
- [33] C. Zhang, K. J. Tseng, T. D. Nguyen, and S. Zhang, “Design and loss analysis of a high speed flywheel energy storage system based on axial-flux flywheel-rotor electric machines,” in *2010 Conference Proceedings IPEC*, pp. 886–891, 2010.

- [34] S. Kumar, T. A. Lipo, and B. Kwon, “A 32 000 r/min axial flux permanent magnet machine for energy storage with mechanical stress analysis,” *IEEE Transactions on Magnetics*, vol. 52, no. 7, pp. 1–4, 2016.
- [35] T. F. Chan and L. L. Lai, “An axial-flux permanent-magnet synchronous generator for a direct-coupled wind-turbine system,” *IEEE Transactions on Energy Conversion*, vol. 22, no. 1, pp. 86–94, 2007.
- [36] Z. Zhang, A. Matveev, R. Nilssen, and A. Nysveen, “Ironless permanent-magnet generators for offshore wind turbines,” *IEEE Transactions on Industry Applications*, vol. 50, no. 3, pp. 1835–1846, 2014.
- [37] Yicheng Chen, P. Pillay, and A. Khan, “PM wind generator topologies,” *IEEE Transactions on Industry Applications*, vol. 41, no. 6, pp. 1619–1626, 2005.
- [38] S. G. Min and B. Sarlioglu, “Fast and systematic design optimization of surface-mounted PM machines using advanced analytical models and subharmonic elimination methods,” *IEEE Transactions on Magnetics*, vol. 55, pp. 1–16, Jan 2019.
- [39] R. Zhang, J. Li, R. Qu, and D. Li, “Analysis and design of triple-rotor axial-flux spoke-array vernier permanent magnet machines,” *IEEE Transactions on Industry Applications*, vol. 54, pp. 244–253, Jan 2018.
- [40] Z. Q. Zhu, D. Howe, E. Bolte, and B. Ackermann, “Instantaneous magnetic field distribution in brushless permanent magnet DC motors. I. open-circuit field,” *IEEE Transactions on Magnetics*, vol. 29, pp. 124–135, Jan 1993.
- [41] E. P. Furlani, “Computing the field in permanent-magnet axial-field motors,” *IEEE Transactions on Magnetics*, vol. 30, pp. 3660–3663, Sep. 1994.
- [42] T. F. Chan, L. L. Lai, and S. Xie, “Field computation for an axial flux permanent-magnet synchronous generator,” *IEEE Transactions on Energy Conversion*, vol. 24, pp. 1–11, March 2009.
- [43] A. Parviaainen, M. Niemela, and J. Pyrhonen, “Modeling of axial flux permanent-magnet machines,” *IEEE Transactions on Industry Applications*, vol. 40, pp. 1333–1340, Sep. 2004.

- [44] J. Azzouzi, G. Barakat, and B. Dakyo, “Quasi-3-D analytical modeling of the magnetic field of an axial flux permanent-magnet synchronous machine,” *IEEE Transactions on Energy Conversion*, vol. 20, pp. 746–752, Dec 2005.
- [45] W. Fei, P. C. K. Luk, and K. Jinupun, “Design and analysis of high-speed coreless axial flux permanent magnet generator with circular magnets and coils,” *IET Electric Power Applications*, vol. 4, no. 9, pp. 739–747, 2010.
- [46] W. Fei, P. C. K. Luk, and T. S. El-Hasan, “Rotor integrity design for a high-speed modular air-cored axial-flux permanent-magnet generator,” *IEEE Transactions on Industrial Electronics*, vol. 58, no. 9, pp. 3848–3858, 2011.
- [47] N. F. Lombard and M. J. Kamper, “Analysis and performance of an ironless stator axial flux PM machine,” *IEEE Transactions on Energy Conversion*, vol. 14, no. 4, pp. 1051–1056, 1999.
- [48] G. Cakal and O. Keysan, “Design of double sided linear motor with easy to manufacture hairpin plate winding,” in *2019 12th International Symposium on Linear Drives for Industry Applications (LDIA)*, pp. 1–5, 2019.
- [49] G. Muller, K. Vogt, and B. Ponick, *Wicklungen Rotierender Elektrischer Maschinen*. John Wiley & Sons Ltd., 2009.
- [50] A. S. McDonald, *Structural analysis of low speed, high torque electrical generators for direct drive renewable energy converters*. PhD thesis, University of Edinburgh, 2008.
- [51] W. C. Young and R. G. Budynas, *Roark's formulas for stress and strain; 7th ed.* McGraw Hill, 2002.
- [52] D. Zarko, S. Stipetic, M. Martinovic, M. Kovacic, T. Jercic, and Z. Hanic, “Reduction of computational efforts in finite element-based permanent magnet traction motor optimization,” *IEEE Transactions on Industrial Electronics*, vol. 65, no. 2, pp. 1799–1807, 2018.
- [53] J. H. Lee, J. Song, D. Kim, J. Kim, Y. Kim, and S. Jung, “Particle swarm optimization algorithm with intelligent particle number control for optimal design of electric machines,” *IEEE Transactions on Industrial Electronics*, vol. 65, no. 2, pp. 1791–1798, 2018.

- [54] A. Cavagnino, G. Bramerdorfer, and J. A. Tapia, “Optimization of electric machine designs - Part I,” *IEEE Transactions on Industrial Electronics*, vol. 64, no. 12, pp. 9716–9720, 2017.
- [55] A. Cavagnino, G. Bramerdorfer, and J. A. Tapia, “Optimization of electric machine designs - Part II,” *IEEE Transactions on Industrial Electronics*, vol. 65, no. 2, pp. 1700–1703, 2018.
- [56] H. Vansompel, P. Leijnen, and P. Sergeant, “Multiphysics analysis of a stator construction method in yokeless and segmented armature axial flux PM machines,” *IEEE Transactions on Energy Conversion*, vol. 34, no. 1, pp. 139–146, 2019.
- [57] P. Schwarz and A. Mockel, “Air gap influence in axial flux machines with different excitation,” *2019 9th International Electric Drives Production Conference (EDPC)*, pp. 1–6, 2019.
- [58] W. R. Finley and M. M. Hodowanec, “Selection of copper versus aluminum rotors for induction motors,” *IEEE Transactions on Industry Applications*, vol. 37, no. 6, pp. 1563–1573, 2001.
- [59] J. D. Widmer, R. Martin, and B. C. Mecrow, “Precompressed and stranded aluminum motor windings for traction motors,” *IEEE Transactions on Industry Applications*, vol. 52, no. 3, pp. 2215–2223, 2016.
- [60] J. D. Widmer, C. M. Spargo, G. J. Atkinson, and B. C. Mecrow, “Solar plane propulsion motors with precompressed aluminum stator windings,” *IEEE Transactions on Energy Conversion*, vol. 29, no. 3, pp. 681–688, 2014.
- [61] T. Ishikawa, Y. Seki, and N. Kurita, “Analysis for fault detection of vector-controlled permanent magnet synchronous motor with permanent magnet defect,” *IEEE Transactions on Magnetics*, vol. 49, no. 5, pp. 2331–2334, 2013.
- [62] V. Yaramasu, B. Wu, P. C. Sen, S. Kouro, and M. Narimani, “High-power wind energy conversion systems: State-of-the-art and emerging technologies,” *Proceedings of the IEEE*, vol. 103, no. 5, pp. 740–788, 2015.

- [63] J. A. Barrado-Rodrigo, J. I. Talpone, and L. Martinez-Salamero, “Variable-speed wind energy conversion system based on a dual stator-winding induction generator,” *IET Renewable Power Generation*, vol. 11, no. 1, pp. 73–80, 2017.
- [64] S. Chatterjee and S. Chatterjee, “Review on the techno-commercial aspects of wind energy conversion system,” *IET Renewable Power Generation*, vol. 12, no. 14, pp. 1581–1608, 2018.
- [65] WindEurope, *Wind energy in Europe in 2019 - Trends and statistics*, Feb. 2020. Available at <https://windeurope.org>, accessed 11 Mar. 2020.
- [66] S. Sanz, T. Arlaban, R. Manzanas, M. Tropeano, R. Funke, P. Kováč, Y. Yang, H. Neumann, and B. Mondesert, “Superconducting light generator for large offshore wind turbines,” *Journal of Physics: Conference Series*, vol. 507, p. 032040, may 2014.
- [67] R. S. Semken, M. Polikarpova, P. Roytta, J. Alexandrova, J. Pyrhonen, J. Nerg, A. Mikkola, and J. Backman, “Direct-drive permanent magnet generators for high-power wind turbines: benefits and limiting factors,” *IET Renewable Power Generation*, vol. 6, no. 1, pp. 1–8, 2012.
- [68] L. Wang, Z. Zhang, H. Long, J. Xu, and R. Liu, “Wind turbine gearbox failure identification with deep neural networks,” *IEEE Transactions on Industrial Informatics*, vol. 13, no. 3, pp. 1360–1368, 2017.
- [69] A. Hayes, L. Sethuraman, K. Dykes, and L. J. Fingersh, “Structural optimization of a direct-drive wind turbine generator inspired by additive manufacturing,” *Procedia Manufacturing*, vol. 26, pp. 740 – 752, 2018. 46th SME North American Manufacturing Research Conference, NAMRC 46, Texas, USA.
- [70] A. McDonald and N. A. Bhuiyan, “On the optimization of generators for off-shore direct drive wind turbines,” *IEEE Transactions on Energy Conversion*, vol. 32, no. 1, pp. 348–358, 2017.
- [71] M. Liserre, R. Cardenas, M. Molinas, and J. Rodriguez, “Overview of multi-MW wind turbines and wind parks,” *IEEE Transactions on Industrial Electronics*, vol. 58, no. 4, pp. 1081–1095, 2011.

- [72] A. Tessarolo, F. Luise, S. Pieri, A. Benedetti, M. Bortolozzi, and M. De Martin, “Design for manufacturability of an off-shore direct-drive wind generator: An insight into additional loss prediction and mitigation,” *IEEE Transactions on Industry Applications*, vol. 53, no. 5, pp. 4831–4842, 2017.
- [73] T. de Paula Machado Bazzo, J. F. Kolzer, R. Carlson, F. Wurtz, and L. Gerbaud, “Multiphysics design optimization of a permanent magnet synchronous generator,” *IEEE Transactions on Industrial Electronics*, vol. 64, no. 12, pp. 9815–9823, 2017.
- [74] S. Jia, R. Qu, J. Li, X. Fan, and M. Zhang, “Study of direct-drive permanent-magnet synchronous generators with solid rotor back iron and different windings,” *IEEE Transactions on Industry Applications*, vol. 52, no. 2, pp. 1369–1379, 2016.
- [75] T. Husain, I. Hasan, Y. Sozer, I. Husain, and E. Muljadi, “Design considerations of a transverse flux machine for direct-drive wind turbine applications,” *IEEE Transactions on Industry Applications*, vol. 54, no. 4, pp. 3604–3615, 2018.
- [76] A. Tovar-Barranco, D. J. Gomez, A. Lopez-de-Heredia, and I. Villar, “High torque density transverse flux permanent magnet machine design for wind power generation,” *2016 XXII International Conference on Electrical Machines (ICEM)*, pp. 782–788, 2016.
- [77] Y. Xu, N. Maki, and M. Izumi, “Overview study on electrical design of large-scale wind turbine HTS generators,” *IEEE Transactions on Applied Superconductivity*, vol. 28, pp. 1–5, Aug 2018.
- [78] X. Song, C. Buhrer, P. Brutsaert, J. Krause, A. Ammar, J. Wiezoreck, J. Hansen, A. V. Rebsdorf, M. Dhalle, A. Bergen, T. Winkler, S. Wessel, M. t. Brake, J. Kellers, H. Putz, M. Bauer, H. Kyling, H. Boy, and E. Seitz, “Designing and basic experimental validation of the world’s first MW-class direct-drive superconducting wind turbine generator,” *IEEE Transactions on Energy Conversion*, vol. 34, no. 4, pp. 2218–2225, 2019.

- [79] A. B. Abrahamsen, D. Liu, N. Magnusson, A. Thomas, Z. Azar, E. Stehouwer, B. Hendriks, G. Van Zinderen, F. Deng, Z. Chen, D. Karwatzki, A. Mertens, M. Parker, S. Finney, and H. Polinder, “Comparison of levelized cost of energy of superconducting direct drive generators for a 10-MW offshore wind turbine,” *IEEE Transactions on Applied Superconductivity*, vol. 28, no. 4, pp. 1–5, 2018.
- [80] G. Ahmad and U. Amin, “Design, construction and study of small scale vertical axis wind turbine based on a magnetically levitated axial flux permanent magnet generator,” *Renewable Energy*, vol. 101, pp. 286 – 292, 2017.
- [81] R. J. Preen and L. Bull, “Toward the coevolution of novel vertical-axis wind turbines,” *IEEE Transactions on Evolutionary Computation*, vol. 19, no. 2, pp. 284–294, 2015.
- [82] M. Malinowski, A. Milczarek, R. Kot, Z. Goryca, and J. T. Szuster, “Optimized energy-conversion systems for small wind turbines: Renewable energy sources in modern distributed power generation systems,” *IEEE Power Electronics Magazine*, vol. 2, no. 3, pp. 16–30, 2015.
- [83] M. A. Mueller and A. S. McDonald, “A lightweight low-speed permanent magnet electrical generator for direct-drive wind turbines,” *Wind Energy*, vol. 12, no. 8, pp. 768–780, 2009.
- [84] M. A. Mueller, A. S. McDonald, and D. E. Macpherson, “Structural analysis of low-speed axial-flux permanent-magnet machines,” *IEE Proceedings - Electric Power Applications*, vol. 152, no. 6, pp. 1417–1426, 2005.
- [85] A. Cavagnino, M. Lazzari, F. Profumo, and A. Tenconi, “A comparison between the axial flux and the radial flux structures for PM synchronous motors,” *IEEE Transactions on Industry Applications*, vol. 38, no. 6, pp. 1517–1524, 2002.
- [86] N. A. Bhuiyan and A. McDonald, “Optimization of offshore direct drive wind turbine generators with consideration of permanent magnet grade and temperature,” *IEEE Transactions on Energy Conversion*, vol. 34, pp. 1105–1114, June 2019.

- [87] McHone Industries, Inc, *Laser cutting vs. waterjet cost for steel sheet metal*, Aug. 2019. Available at <https://blog.mchoneind.com/blog/cost-laser-vs-waterjet-cutting>, accessed 07 June 2020.
- [88] Dahlstrom Roll Form, *Water jet cutting vs laser cutting & other metal cutting services*, Nov. 2018. Available at <https://blog.dahlstromrollform.com/water-jet-cutting-vs-laser-cutting-metal-cutting-services>, accessed 07 June 2020.
- [89] K. Mendelssohn and H. M. Rosenberg, *The Thermal Conductivity of Metals at Low Temperatures*. Academic Press, 1961.
- [90] S.-L. Chung and J.-S. Lin, “Thermal conductivity of epoxy resin composites filled with combustion synthesized h-BN particles,” *Molecules*, vol. 21, p. 670, 05 2016.
- [91] H. Li, Z. Chen, and H. Polinder, “Optimization of multibrid permanent-magnet wind generator systems,” *IEEE Transactions on Energy Conversion*, vol. 24, pp. 82–92, March 2009.
- [92] A. S. McDonald, N. Al-Khayat, D. Belshaw, M. Ravilious, A. Kumaraperumal, A. M. Benatamane, M. Galbraith, D. Staton, K. Benoit, and M. Mueller, “1MW multi-stage air-cored permanent magnet generator for wind turbines,” *6th IET International Conference on Power Electronics, Machines and Drives (PEMD 2012)*, pp. 1–6, 2012.
- [93] B. Maples, M. Hand, and W. Musial, “Comparative assessment of direct drive high temperature superconducting generators in multi-megawatt class wind turbines,” *Technical Report, National Renewable Energy Laboratory*, pp. 1–40, 10 2010.
- [94] C. Versteegh, “Design of the zephyros Z72 wind turbine with emphasis on the direct drive PM generator,” *Nordic Workshop on Power and Industrial Electronics*, pp. 1–7, 2004.
- [95] D. Bang, *Design of Transverse Flux Permanent Magnet Machines for Large Direct-Drive Wind Turbines*. Phd dissertation, Delft University of Technology, Delft, The Netherlands, October 2010.

- [96] N. Hodgins, O. Keysan, A. McDonald, and M. Mueller, “Linear generator for direct drive wave energy applications,” in *The XIX International Conference on Electrical Machines - ICEM 2010*, pp. 1–6, 2010.
- [97] D. J. Struik, “Joseph Fourier.” <https://www.britannica.com/biography/Joseph-Baron-Fourier>. Accessed: 2020-09-07.

Appendix A

FOURIER SERIES REPRESENTATION OF MAGNETIZATION

The Fourier¹ series representation of any periodic function, $f(x)$, can be expressed as

$$f(x) = a_0 + \sum_{n=1}^{\infty} a_n \cos\left(\frac{2\pi n}{T} x\right) + \sum_{n=1}^{\infty} b_n \sin\left(\frac{2\pi n}{T} x\right) \quad (\text{A.1})$$

where T represents the fundamental period of the function, and n represents n^{th} order space harmonic. In the expression, a_0 , a_n , and b_n represent the DC component, cosine term coefficients and sine term coefficients, respectively. They can be found as follows

$$a_0 = \frac{1}{T} \int_0^T f(x) dx \quad (\text{A.2})$$

$$a_n = \frac{2}{T} \int_0^T f(x) \cos\left(\frac{2\pi n}{T} x\right) dx \quad (\text{A.3})$$

$$b_n = \frac{2}{T} \int_0^T f(x) \sin\left(\frac{2\pi n}{T} x\right) dx \quad (\text{A.4})$$

In this part, y-component of the magnetization vector of the permanent magnets, $M_y(x)$, will be expressed using Fourier series expansion. The characteristics of this periodic function can be seen in Fig. A.1. Then, the Fourier series expansion can be written as

$$M_y(x) = \sum_{n=1}^{\infty} m_{ycs} \cos\left(\frac{\pi n}{\tau_p} x\right) + \sum_{n=1}^{\infty} m_{ysn} \sin\left(\frac{\pi n}{\tau_p} x\right) \quad (\text{A.5})$$

Note that the magnetization component, $M_y(x)$, is periodic with fundamental period of $2\tau_p$, and it does not has DC term. The Fouries series coefficients can be expressed

¹ Jean Baptiste Joseph Fourier, a French mathematician and a physicist, was born in Auxerre, France. He initialized Fourier series, Fourier transforms and their applications to problems of heat transfer and vibrations. The Fourier series, Fourier transforms and Fourier's Law are named in his honor [97].

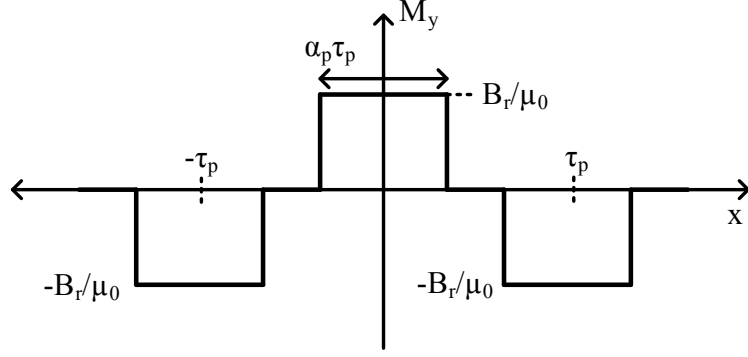


Figure A.1: Magnetization characteristics of permanent magnets

as follows

$$m_{ycs} = \frac{1}{\tau_p} \int_{-\tau_p}^{\tau_p} M_y(x) \cos \left(\frac{\pi n}{\tau_p} x \right) dx \quad (\text{A.6})$$

$$m_{ysn} = \frac{1}{\tau_p} \int_{-\tau_p}^{\tau_p} M_y(x) \sin \left(\frac{\pi n}{\tau_p} x \right) dx \quad (\text{A.7})$$

Note that $M_y(x)$ and sine term are odd functions, and cosine term is even function. Since the integral of a periodic odd function is zero over one period, one can conclude

$$m_{ysn} = 0 \quad (\text{A.8})$$

The cosine term coefficient of Fourier series expansion can be written as

$$m_{ycs} = \frac{2}{\tau_p} \int_0^{\tau_p} M_y(x) \cos \left(\frac{\pi n}{\tau_p} x \right) dx \quad (\text{A.9})$$

When the integral sum is written separately, considering Fig A.1, one can obtain

$$m_{ycs} = \frac{2}{\tau_p} \left[\int_0^{\frac{\alpha_p \tau_p}{2}} \frac{B_r}{\mu_0} \cos \left(\frac{\pi n}{\tau_p} x \right) dx - \int_{\tau_p - \frac{\alpha_p \tau_p}{2}}^{\tau_p} \frac{B_r}{\mu_0} \cos \left(\frac{\pi n}{\tau_p} x \right) dx \right] \quad (\text{A.10})$$

$$m_{ycs} = \frac{2B_r}{\mu_0 \tau_p} \left[\int_0^{\frac{\alpha_p \tau_p}{2}} \cos \left(\frac{\pi n}{\tau_p} x \right) dx - \int_{\tau_p - \frac{\alpha_p \tau_p}{2}}^{\tau_p} \cos \left(\frac{\pi n}{\tau_p} x \right) dx \right] \quad (\text{A.11})$$

Note that the integral in this form can be written as

$$\int_a^b \cos(kx) dx = \frac{1}{k} \left(\sin(kb) - \sin(ka) \right) \quad (\text{A.12})$$

Then, it can be written

$$m_{y_{cs}} = \frac{2B_r}{\pi n \mu_0} \left[\sin \left(\frac{\pi n \tau_p \alpha_p}{2} \right) - \sin \left(\frac{\pi n}{\tau_p} \tau_p \right) + \sin \left(\frac{\pi n}{\tau_p} \tau_p - \frac{\pi n \tau_p \alpha_p}{2} \right) \right] \quad (\text{A.13})$$

Note that $\sin(\pi n)$ term is zero for all harmonics. Then, one can write

$$m_{y_{cs}} = \frac{2B_r}{\pi n \mu_0} \left[\sin \left(\frac{\pi n \alpha_p}{2} \right) + \sin \left(\pi n - \frac{\pi n \alpha_p}{2} \right) \right] \quad (\text{A.14})$$

Note that the sum of two sine terms can be written as

$$\sin(a) + \sin(b) = 2 \sin \left(\frac{a+b}{2} \right) \cos \left(\frac{a-b}{2} \right) \quad (\text{A.15})$$

Then,

$$m_{y_{cs}} = \frac{2B_r}{\pi n \mu_0} \left[2 \sin \left(\frac{\pi n}{2} \right) \cos \left(\frac{\pi n}{2} - \frac{\pi n \alpha_p}{2} \right) \right] \quad (\text{A.16})$$

Also, the cosine term can be decomposed as

$$\cos(a-b) = \cos(a) \cos(b) + \sin(a) \sin(b) \quad (\text{A.17})$$

Then, one can write that

$$m_{y_{cs}} = \frac{2B_r}{\pi n \mu_0} \left[2 \sin \left(\frac{\pi n}{2} \right) \left(\cos \left(\frac{\pi n}{2} \right) \cos \left(\frac{\pi n \alpha_p}{2} \right) + \sin \left(\frac{\pi n}{2} \right) \sin \left(\frac{\pi n \alpha_p}{2} \right) \right) \right] \quad (\text{A.18})$$

$$m_{y_{cs}} = \frac{2B_r}{\pi n \mu_0} \left[2 \sin \left(\frac{\pi n}{2} \right) \cos \left(\frac{\pi n}{2} \right) \cos \left(\frac{\pi n \alpha_p}{2} \right) + 2 \sin^2 \left(\frac{\pi n}{2} \right) \sin \left(\frac{\pi n \alpha_p}{2} \right) \right] \quad (\text{A.19})$$

The sine function can be written as

$$\sin(a) = 2 \sin \left(\frac{a}{2} \right) \cos \left(\frac{a}{2} \right) \quad (\text{A.20})$$

$$m_{y_{cs}} = \frac{2B_r}{\pi n \mu_0} \left[\sin(\pi n) \cos \left(\frac{\pi n \alpha_p}{2} \right) + 2 \sin^2 \left(\frac{\pi n}{2} \right) \sin \left(\frac{\pi n \alpha_p}{2} \right) \right] \quad (\text{A.21})$$

Remember that $\sin(\pi n)$ term is zero for all harmonics. Then, the analysis of Fourier series expansion of the magnetization component can be concluded as follows

$$m_{y_{cs}} = \frac{4B_r}{\pi n \mu_0} \sin \left(\frac{\pi n \alpha_p}{2} \right) \sin^2 \left(\frac{\pi n}{2} \right) \quad (\text{A.22})$$

$$M_y(x) = \sum_{n=1}^{\infty} m_{y_{cs}} \cos \left(\frac{\pi n}{\tau_p} x \right) \quad (\text{A.23})$$

Appendix B

CONSTANTS USED IN CIRCULAR PLATE THEORY FOR DEFLECTION ANALYSIS

The following constants are used for the deflection analysis of a circular rotor discs exposed to Maxwell stress due to permanent magnets [51].

$$C_2 = \frac{1}{4} \left[1 - \left(\frac{b}{a} \right)^2 \left(1 + 2 \ln \frac{a}{b} \right) \right] \quad (\text{B.1})$$

$$C_3 = \frac{b}{4a} \left\{ \left[\left(\frac{b}{a} \right)^2 + 1 \right] \ln \frac{a}{b} + \left(\frac{b}{a} \right)^2 - 1 \right\} \quad (\text{B.2})$$

$$C_8 = \frac{1}{2} \left[1 + \nu + (1 - \nu) \left(\frac{b}{a} \right)^2 \right] \quad (\text{B.3})$$

$$C_9 = \frac{b}{a} \left\{ \frac{1 + \nu}{2} \ln \frac{a}{b} + \frac{1 - \nu}{4} \left[1 - \left(\frac{b}{a} \right)^2 \right] \right\} \quad (\text{B.4})$$

$$L_{11} = \frac{1}{64} \left\{ 1 + 4 \left(\frac{r_o}{a} \right)^2 - 5 \left(\frac{r_o}{a} \right)^4 - 4 \left(\frac{r_o}{a} \right)^2 \left[2 + \left(\frac{r_o}{a} \right)^2 \right] \ln \frac{a}{r_o} \right\} \quad (\text{B.5})$$

$$L_{17} = \frac{1}{4} \left\{ 1 - \frac{1 - \nu}{4} \left[1 - \left(\frac{r_o}{a} \right)^4 \right] - \left(\frac{r_o}{a} \right)^2 \left[1 + (1 + \nu) \ln \frac{a}{r_o} \right] \right\} \quad (\text{B.6})$$

Appendix C

SUPPLEMENTARY DOCUMENTS

The supplementary documents are shared in the GitHub repository. It can be reached with the following link and QR code.

<https://github.com/gkhnckl/msc-thesis-supplementary>



Figure C.1: Scan this QR code to reach the repository

In the repository, the following documents and more can be found:

- Author's CV
- Analytical modeling and optimization files on MATLAB 2016a
- Electromagnetic models for the prototype and 1 MW generator on ANSYS Maxwell 19.1
- Structural and thermal models for both machines on SolidWorks 2018
- The thesis defense presentation
- Some photos of manufacturing